Pasqual Rivera

Interlayer Valley Excitons in Two-Dimensional Semiconductor Heterostructures

Pasqual Rivera

A dissertation submitted in partial fulfillment

of the requirements for the degree of

Doctor of Philosophy

University of Washington

2018

Reading Committee:

Xiaodong Xu

Arka Majumdar

David Cobden

Program Authorized to Offer Degree:

Physics

University of Washington

Abstract

Interlayer Valley Excitons in Two-Dimensional Semiconductor Heterostructures

Pasqual Rivera

Chair of the Supervisory Committee:

Associate Professor Xiaodong Xu

Department of Physics and Materials Science and Engineering

The ability to isolate and manipulate two-dimensional crystals into carefully designed van der Waals heterostructures is an emerging technology that offers an unprecedented level of control over the optical and electronic properties of the resulting synthetic materials. As the library of two-dimensional materials increases in size, adding new types of material properties and geometries, the power of this new technology grows. Many examples of new electronic behavior have already being found by exploring the possible heterostructures. In the following, I present an exploration into the optical properties of the $MoSe_2$-WSe_2 heterobilayer, which is an atomically thin type-II heterointerface between two valley semiconductors. In particular, this thesis presents the discovery and characterization of the properties of the interlayer exciton – the Coulomb bound state from electron and hole localized in different layers. This unique type of exciton is shown to demonstrate extended population and valley polarization lifetimes compared to the excitons localized in the constituent monolayers alone. Furthermore, the electric dipole moment associated with the separated charges provides a simple means to control the interlayer exciton energy, as well as the population and valley lifetimes. By placing the heterobilayer on top of a photonic crystal cavity, the intensity of light emission from the interlayer exciton can also be enhanced by an order of magnitude. Additionally, magnetic field dependent photoluminescence from trapped interlayer excitons in heterobilayers of different twist angles between the layers provides the first evidence for the influence of a moiré pattern on the optical properties of these excitons. Finally, the outlook for future studies in this new system are considered.

ACKNOWLEDGMENTS

I would like to express my gratitude to Xiaodong Xu, who has been an amazing advisor. His passion for scientific discovery is only matched by his unwavering work ethic. I deeply appreciate the warmth, humor, understanding, and compassion he has quietly demonstrated, somehow in the most powerful ways at precisely those few critical moments when it was most needed. His steady character and leadership and genuine excitement for data have kept the Xu Lab an excellent work environment, and are undoubtedly keys to the success we have achieved together. I appreciate the many things I have learned from him, and the privilege of using all the nice new fancy toys he has purchased over the years (such as lasers, cryostats, sem/ebl systems, etc). I consider myself very lucky to have worked with him and will surely miss it.

Many thanks are also deserved by my doctoral supervisory committee and professors, from which I have benefited greatly. The curiosity of Dave Cobden has often made me reconsider my own measurements and processes, always for the better. I will regrettably miss his uniquely dry humor. I thank Arka Majumdar for the illuminating discussions regarding real world applications of 2D materials, which has provided a refreshing contrast to fundamental scientific research and helped shape my path forward. Special thanks also to Anton Andreev, whose provocative questioning after my final examinations was a formative experience which made me feel like I was really a decent scientist, and for this I am deeply grateful. Finally, I thank Kai-Mei Fu for giving me my first opportunity in a laboratory setting, which is where this journey all started. I am also very appreciative of the support given by our caring and outstanding student advisor Catherine Provost.

The enclosed work has benefited greatly from many collaborations over the years. In particular, the theoretical work from Wang Yao and Hongyi Yu has developed in lockstep with our experimental findings, the combination of which underpins the current understanding of the field. Every sample I made is owed in part to the bulk crystals generously provided by the talented scientists at Oak Ridge National Laboratory, including David Mandrus, Jiaqiang Yan, and Nirmal Ghimire, and from Takashi Taniguchi and Kenji Watanambe from NIMS in Japan. Within UW, collaborations with the Fu Lab and Cobden have accelerated the pace of discovery, and are much appreciated.

Over the years, I’ve worked with many people in the Xu Laboratory as well, all of which have shaped my PhD experience. I want to thank John Schaibley, who taught me more about optics and lasers than anyone else. The many lunches we spent talking about science and society and many weekends we spent taking data were some of the best times. I wish him the greatest success at The University of Arizona. Special thanks also to my lab family in the early years, when the Xu Lab was small, including Mitch, Grant, Sanfeng, and Gen. Also, my good friend Jason Ross, who taught me SEM and EBL, beat me at poker, and who I shared many late evenings with. Sanfeng was a constant source of laughter, raw intellect, and creative chaos. The Sanfeng-Kyle ping-pong battles in the loading bay were intense. I thank Gen for her great sense of humor and can-do-anything attitude. I think she may work harder than anyone else in the Xu Lab (maybe the entire Physics department) – she has a bright future. Special thanks also to Kyle Seyler, who always had a smile on his face, even when the problem sets, lasers, or experiments weren’t going amazing. He is a true scientist, and undoubtedly takes the nicest data sets of anyone I know. It’s been a great pleasure working alongside him in the dark over the years and I look forward to seeing the amazing work he will achieve in the future. I also want to thank the second generation of Xu Lab members, and wish you all the best in your future: Nathan Wilson, Bevin Huang, Ding Zhong, Tiancheng Song, Chenfeng Du, Minhao He, Harold Cai, Colin Chow, Fucai Liu, Qi Zhang, Chang-Hua Liu, and Dmitry Ovchinnikov, I’ve enjoyed working with you all. Special thanks to Nathan, who is an extremely talented scientist and system engineer. He designs the best microscopes, hands down. Thanks also to Bevin, who everyone knows can eat more than anyone else, but can’t eat cheese (but we all know he does anyways). I also thank the many undergraduates I’ve worked withover the years, especially Essance Ray for her dedicated and excellent hard work. She is a very talented undergraduate researcher with a bright future and an infectious laugh. I’ve also enjoyed the relationships I have with the people from the Cobden and Fu Labs who I’ve had the pleasure to work with. I’m sorry that I cannot name everyone! It’s mostly been a lot of fun working amongst such brilliant and great minds.

The most important thanks go out to my family and hometown friends. Ultimately, finding and marrying Rachel was the best thing that happened during my time in the Xu Lab. She is my favorite. Without her constant humor, compassion, and support, I don’t want to imagine where I’d be today. I also would never have gotten our little doggy Coda, who I think is really funny and adorable. To THE GROUP (you know who you are) thank for being awesome, forever. Sorry I missed so many events over the years because I was sitting in a pitch-black room shooting lasers at stuff so small you can’t even see it. Many thanks to Cara and Jonas for letting us come to Hawaii every year to unwind, even if it meant also unwinding your home. And thanks to Lucienne for always being the rock – you’re solidarity is legendary. I think of you when I need inspiration. Thanks to Selah too, for always providing high quality artwork that makes me smile, and for loving Rachel more than me ☺. To my parents, I couldn’t have done this without their unwavering love and support, not only now, but every moment of my life. Finally, as a family we endured the most difficult loss during my time at UW, when my nephew passed away after nearly a year of fighting brain cancer. I want to specially thank all the nurses and doctors at Children’s Hospital for their dedicated work to try and save him from this terrible disease. Every moment I spent with him was the most precious treasure to me. We all miss you and love you, Bennett! This was the worst of times in my life, but with the help of all the people above, I was able to make it through the toughest times.

This work is dedicated to my late nephew, who I miss more than anything in the world.

In loving memory of Bennett Elijah.

TABLE OF CONTENTS

Appendices

List of Figures

List of Tables

Abbreviations

2D – Two-dimensional

TMD – Transition metal dichalcogenides

hBN – Hexagonal boron nitride

FET – Field effect transistor

PV – Photovoltaic

LED – Light emitting diode

vdW – van der Waals

BZ – Brillouin Zone

CBM – Conduction band minimum

VBM – Valence band maximum

AFM – Atomic force microscopy

PDMS – Poly-dimethylsiloxane

PC – Polycarbonate

IPA – Isopropyl Alcohol

EBL – Electron beam lithography

SEM – Scanning electron microscope

PMMA – Poly (methyl)-methacrylate

PVA – Poly-vinyl alcohol

CVD – Chemical vapor deposition

μ-ARPES – Micron-scale angle resolved photoemission spectroscopy

HS – Heterostructure

PL – Photoluminescence

SHG – Second harmonic generation

cw – Continuous wave

PLE – Photoluminescence excitation spectroscopy

CCD – Charge coupled device

PhC – Photonic crystal

IX – Interlayer exciton

FWHM – Full width at half maximum

Chapter 1: Introduction to Two-dimensional materials

1.1 Two-dimensional materials

The discovery of two-dimensional (2D) materials has opened up the door to an entire class of new materials for fundamental scientific research and device technologies. The world witnessed the birth of this new area of physics and materials science in 2004 when graphene, a single layer of graphite consisting with carbon atoms arranged in a honeycomb lattice, was the first 2D crystal ever isolated[1]. At that time, nobody knew how deep the treasure trove of new physics was, or that a tidal wave of research efforts in this new field had just begun. The high quality and unique electronic properties of graphene facilitated a number of discoveries in fundamental physics[2], most remarkably the presence of massless Dirac fermions[3]. The discovery marked a new age in condensed matter physics and was awarded the Nobel prize in physics in 2010.

The exciting discoveries in graphene prompted researchers to search for other two-dimensional materials, hoping that more novel physics would be revealed[4-11]. Accordingly, the class of materials has grown rapidly in the past decade, and the search not only continues, but is accelerating. Of particular interest in this dissertation are the layered transition metal dichalcogenides (TMDs)[12,13], which undergo a transition from indirect bandgap semiconductors in the bulk to direct bandgap semiconductors in their monolayer form[14,15]. The direct bandgap is in the visible range and, despite being less than a nanometer thick, these materials boast extraordinarily high peak absorptions exceeding 15%[16], and exceptionally high exciton binding energies of up to 0.5 V[17]. The strong light-matter interactions in these materials make them an attractive platform for next-generation ultrathin optoelectronic devices[18-22]. Additionally, the deep valleys and symmetry properties of the monolayer TMDs leads to an advantageous set of valley optical selection rules[23,24], making it possible to address a particular valley in the electronic band structure using circularly polarized light[25]. Finally, the enormous spin-orbit splitting leads to spin-valley locking, protecting the valley degree of freedom of electrons and excitons in these materials. A further introduction to these materials is the foundation for understanding the bulk of this thesis, so a detailed introduction is provided in Chapter 2.

1.2 Van der Waals heterostructures

Thanks to intense research efforts, researchers have isolated and characterized 2D materials exhibiting nearly all known electronic behaviors found in their conventional 3D counterparts; metals, semi-metals, superconductors, semiconductors, insulators, and ferromagnetic materials have all been found in monolayer form, as shown in Fig. 1-1. The natural trajectory of this field of science leads to questions of how these materials can be combined to form heterostructures, and what are the properties of these synthetic materials. Techniques for isolating and manipulating single layered materials have evolved to now allow the assembling of 2D materials into arbitrarily complex heterostructures (see Fig. 1-2). In these synthetic heterostructures, the layers are bound to one another via the short range vdW interactions, which are much weaker compared to the in-plane covalent bonds that make up the 2D crystals. Depending on the nature and strength of the interlayer interactions, the monolayer materials can either largely retain their electronic properties, or interact with one another to give rise to altogether new properties. For example, samples consisting of graphene encapsulated between hexagonal boron nitride (hBN) can exhibit behavior ranging from that of pristine graphene, where the hBN serves only as an ultra-flat substrate[26,27], to demonstrating the fractal Hofstadter's butterfly spectrum, which comes about from the formation of a superlattice between hBN and graphene when their crystal lattices are closely aligned[28-30].

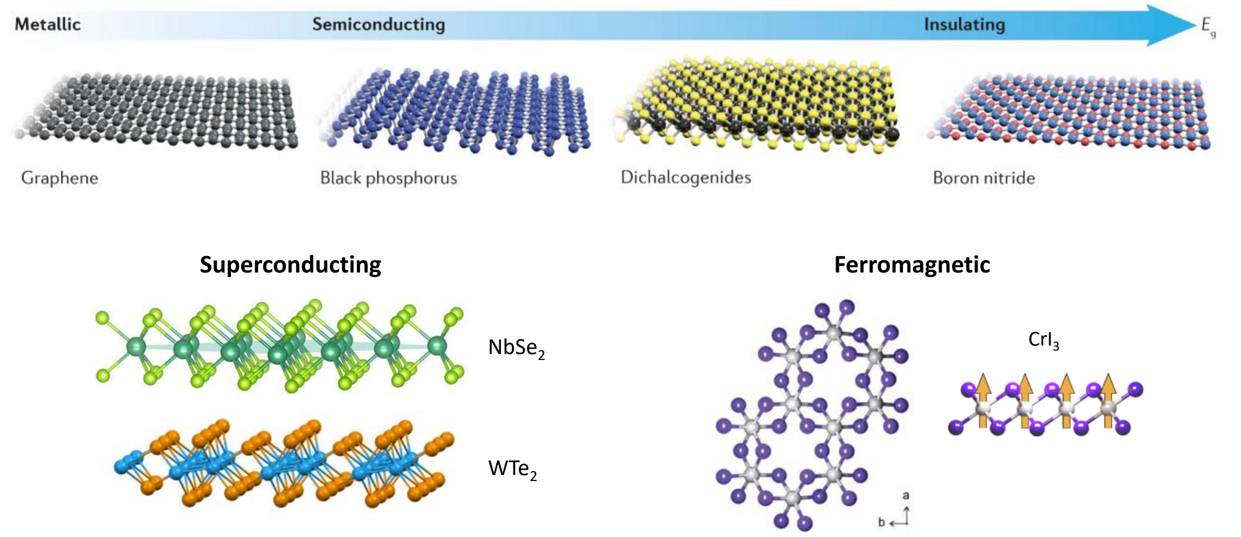

Figure 1-1 | Library of two-dimensional materials. The library of 2D materials includes materials exhibits every electronic property found in three-dimensional materials. Graphics reproduced from Liu, et al. Nat. Rev. Mats 1 (2016); Zhu, et al. Nat Comm 7 (2016); and Huang, et al. Nature 546 (2017).

The technology of van der Waals (vdW) heterostructures[31,32] is now an extremely prominent and fast growing field in condensed matter physics, which has enabled the fabrication of 2D electronic, photonic, and optoelectronic devices[33], such as field effect transistors (FETs)[34], photovoltaics (PVs)[35,36], p-n junctions and light emitting diodes (LEDs)[37-39], to name just a few. This newfound ability also opens the door to engineering novel electronic and optical devices that have no analogue in 3D systems. The exploration of these vdW materials and devices is now the cutting edge of 2D materials research, and the list of possible devices is practically unlimited.

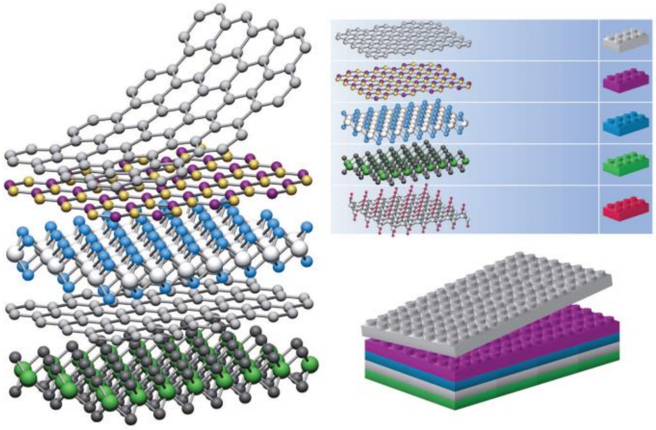

Figure 1-2 | Van der Waals heterostructures. Arbitrarily complex layered structures can now be made from a wide assortment of 2D materials. Graphics reproduced from Geim & Grigorieva, *Van der Waals heterostructures.* Nature **499** (2013).

1.3 Thesis outline

The overarching theme of this thesis will be the characterization of the optical properties of the monolayer $MoSe_2$-WSe_2 vdW bound heterostructure, or heterobilayer. The second chapter will provide an introduction to the optical properties of the monolayer TMDs, with special attention paid to the valley excitons and their optical selection rules. This will provide a foundation for subsequent chapters focusing on the optical properties of the $MoSe_2$-WSe_2 heterobilayer. Chapter 3 will describe the contemporary approach to fabricating vdW heterostructures, from the isolation and characterization of monolayer materials to the methods used to manipulate and stack them on top of one another. This will also include a brief consideration of lithographic techniques for fabricating electrical contacts to 2D devices with micron-scale dimensions. The rest of the thesis will consider the theoretical and experimental properties of the spatially indirect excitons in this system, those made up of electron and hole from different layers, i.e. interlayer excitons (IXs).

The band structure of the transition metal dichalcogenide heterobilayers will be discussed in Chapter 4, showing that the combination of the two different monolayer semiconductors forms a type-II electronic interface. Then a theoretical discussion of the optical coupling of interlayer excitons in $MoSe_2$-WSe_2 heterobilayers with small twist angles is presented in Chapter 5. This will provide a simple derivation of the dispersion for the interlayer exciton and examine how it can couple directly to light, even though the ground state is momentum indirect. Chapter 6 reports the experimental discovery of bright interlayer excitons in the $MoSe_2$-WSe_2 heterostructure and characterizes some of their properties. This includes the ultrafast interlayer charge transfer mechanism for formation of the interlayer exciton, as well as the dramatic enhancement of the population lifetime. The latter results comes from the suppression of the interlayer exciton oscillator strength resulting from the spatial separation of the electron and hole. This chapter will also provide direct evidence of the dipolar nature of IX, through control of the IX energy via externally applied electric fields, and the observation of density dependent self-energy corrections.

Having demonstrated bright IX, Chapter 7 will detail the experimental realization of valley IX. Through time and polarization resolved PL measurements it is shown that the spatial separation of electron and hole reduces valley exchange interactions to preserve IX valley information for many orders of magnitude longer than in the isolated monolayers. This chapter will also show how valley exchange interactions become important at high IX density, through the visualization of these interactions in the spatial profile of the long-range drift-diffusion of the IX valley degree of freedom.

In Chapter 8, I will show how placing the $MoSe_2$-WSe_2 heterobilayer directly on top of a GaP photonic crystal cavity produces a hybrid exciton-cavity device. In this work, weak coupling between the interlayer exciton and the photonic crystal cavity produces an order of magnitude increase in the emission intensity from the interlayer exciton. The polarization of the cavity-enhanced emission is also seen to be controlled by the cavity.

Chapter 9 is devoted to the recent discovery of interlayer excitons confined by the moiré pattern inevitably formed in any real heterobilayer, due to finite lattice mismatch and twisting angle between the constituent hexagonal lattices. Through careful analysis of temperature and power dependent photoluminescence measurements, we establish that presence of trapped interlayer excitons over large areas of several $MoSe_2$-WSe_2 heterobilayers. Remarkably, we identify a twist-angle dependent Landé g-factor for interlayer excitons in different heterobilayers.

The Zeeman shift contributions from spin, orbit, and valley magnetic moments are identified. Through a combination of polarization dependent measurements and careful analysis of g-factors for different twist angles, we attribute the confining potentials to the intrinsic moiré superlattice potential.

A brief summary of the prospects and challenges for future studies and applications for interlayer excitons is found in Chapter 10.

Chapter 2: Transition Metal Dichalcogenides

2.1 Crystallographic Structure and Electronic Properties

The transition metal dichalcogenides (TMDs) have chemical formula MX_2, with the M representing a transition metal atom and the X representing a chalcogen atom. There are over 60 bulk materials of this stoichiometry, spanning a wide range of electronic properties including insulators, semiconductors, semimetals, true metals, as well as superconductors and charge density wave materials at low temperatures[40]. Of particular interest here are the semiconducting TMDs, the most common of which are $MoSe_2$, MoS_2, WSe_2, and WS_2. The MX_2 unit cell is composed of a transition metal atom covalently bonded to six selenium ligands with trigonal prismatic coordination, as shown in Figure 2-1A. Figure 2-1B shows a side view of a single layer of MX_2 crystal, which has a thickness of ~7 Å. The top-down view (Fig. 2-1C) illustrates the hexagonal lattice structure in the plane. The bulk materials are composed of repeated layers with 2H stacking – each successive layer is rotated by 180° with alternating M and X atoms along the vertical direction – and the layers are held together by van der Waals (vdW) forces. Due to the relative weakness of vdW interactions compared to the in-plane covalent bonds, it is possible to peel away single layers of the MX_2 materials from the bulk crystals without damaging them. This technique is referred to as 'micromechanical cleavage', 'exfoliation', or the well-known 'scotch-tape method' which was used to isolate graphene in 2004[1]. The ease at which the layers of the bulk materials sheer away explains why MoS_2 is a common dry lubricant.

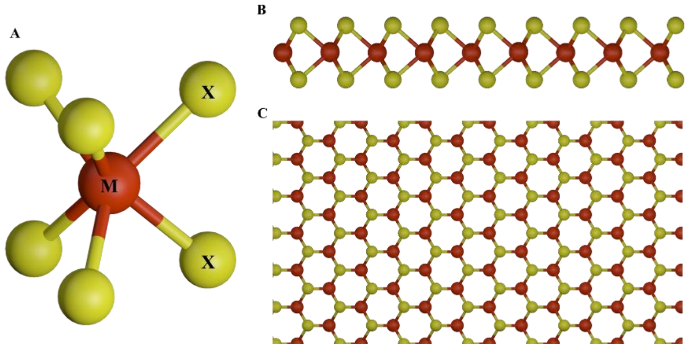

Figure 2-1 | Monolayer transition metal dichalcogenides. (A) The unit cell of MX_2. Single layer of MX_2 as viewed from **(B)** in the plane and **(C)** out of the plane.

While the bulk TMD have long been known as indirect gap semiconductors[13,41], the thinnest flakes behave quite differently. The clearest example is a single monolayer of TMD, which when thinned down to a single layer, becomes a direct bandgap semiconductor[14,15,42]. For brevity, in the following discussion any reference to TMD implies the monolayer form. Since the hexagonal lattice of TMD shares many similarities with that of graphene, much can be learned from comparing the two materials. From solid state physics, a single electron in a periodic lattice can be represented by Bloch waves, with energy eigenvalues forming continuous bands in the momentum space[43]. The energy minima in the momentum space are referred to as the ‘valleys’ in the electronic spectrum. For the 2D hexagonal lattice shown in Fig. 2-2A, the reciprocal lattice vectors in the momentum space form the 2D hexagonal Brillouin zone (BZ) shown in Fig. 2-2B. In the simplest case, where each lattice site on the crystal is the same atom, as is the case with the honeycomb of C atoms forming graphene, the electronic band structure from $\vec{k}\cdot\vec{p}$ theory[44] is shown in Fig. 2-2C. Zooming in on a single valley illustrates how the conduction band minimum (CBM) and valence band maximum (VBM) touch at a single point located at the corner of hexagonal BZ. The electronic valleys at adjacent (or opposite) corners of the BZ are conventionally referred to as the K and K’ (or $\pm K$) valleys. A unique aspect of graphene’s band structure is that the dispersion relation near the K points is linear. Using the tight binding approximation, one can approximate the low energy bands by the Hamiltonian $H = v_F(\tau\sigma_x k_x + \sigma_y k_y)$, where $v_F \sim 10^6$ m/s is known as the Fermi velocity, k_i are the in-plane momentum space wavevectors, σ_i are the Pauli matrices, and $\tau = \pm 1$ is a binary valley index. This Hamiltonian has the form of the famous Dirac equation for massless fermions, and so the edges of the BZ are also known as the Dirac points.

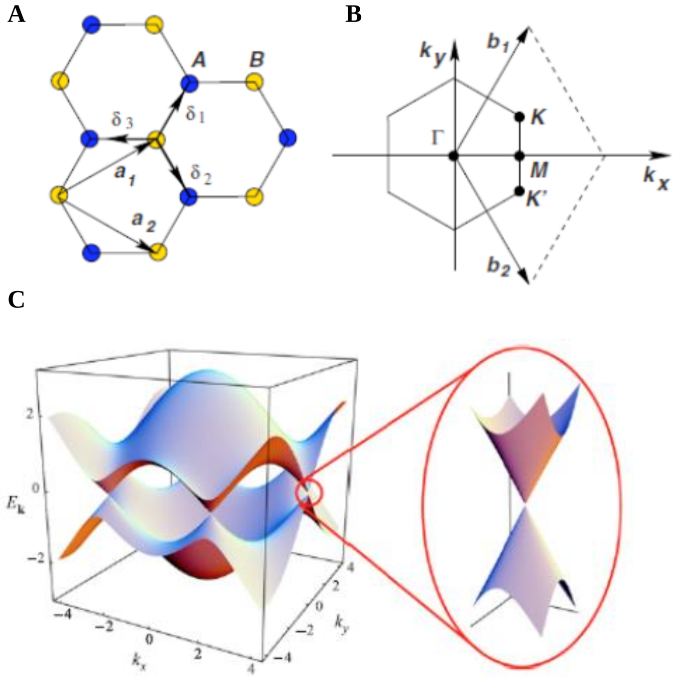

Figure 2-2 | Electronic band structure of graphene. (A) The real space lattice contains A and B sites arranged with hexagonal symmetry. **(B)** The hexagonal Brillouin zone with corners at the K and K’ valleys. **(C)** The 2D band structure of graphene. Inset highlights the linear dispersion near the Dirac points. Graphics reproduced from Castro Neto, et al. *The electronic properties of Graphene*, Reviews of Modern Physics **81** 2009.

By comparing the TMD crystal structure with graphene one can gain insight into the band structure. In particular, the hexagonal symmetry of MX_2 differs from graphene in that adjacent atoms are not the same. In the case of broken sublattice symmetry, the valleys remain at the Dirac points, but the effective Hamiltonian becomes $H \sim at\left(\tau\sigma_x k_x + \sigma_y k_y\right) + \frac{\Delta}{2}\sigma_z$, where a is the lattice constant, and t is the intersite hopping integral[40]. The new term indicates the opening of a bandgap (Δ) at the Dirac points of the hexagonal BZ, and the band edge dispersion is parabolic instead of linear, which implies finite effective mass for the Bloch electrons. The monolayer MX_2 band structure, ignoring the spin-orbit coupling, is well described by the Hamiltonian above, which is equivalent to the equation for massive Dirac fermions. Notably, the MX_2 bandgap resides in the visible (1.6-2.0 eV)[18,40] which is an important factor for technological considerations.

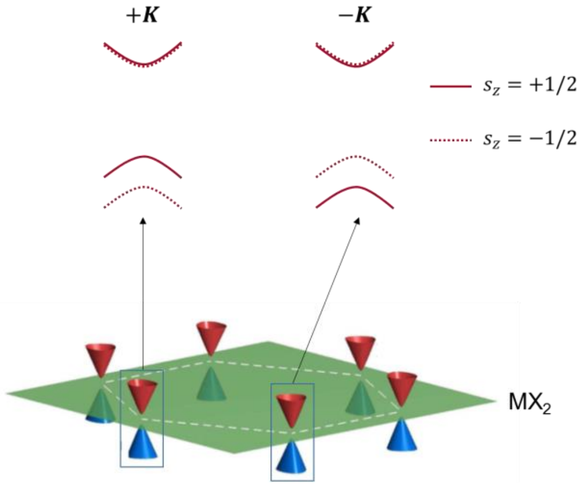

Figure 2-3 | Electronic band structure of MX_2. The valleys at the Dirac points have spin-orbit induced splitting of the valence and conduction bands that are related by time reversal. The spin-splitting of the conduction band an order of magnitude smaller than that of the valence band.

In many materials, the band structure can be strongly affected by coupling of the orbital angular momentum of an electron in an atomic orbital with the spin angular momentum of the electron, i.e. spin-orbit coupling. In the TMDs, band edge electrons are primarily in the outermost d-orbitals of the heavy transition metal atoms (Mo or W). Density functional theory calculations reveal that the CBM is primarily composed of d_{z^2} $(\sim Y_2^0)$ orbitals and electrons at the VBM are mostly in $\frac{1}{\sqrt{2}}\left(d_{x^2-y^2} \pm i d_{xy}\right)$ orbitals[23] $\left(\sim Y_2^{\pm 2}\right)$. The mirror symmetry about the center of the TMD plane implies that only out-of-plane spins may have spin-orbit splitting, and the lack of an inversion center in MX_2 gives rise to spin-orbit fields that break the spin degeneracy at the band edges. Importantly, since opposing valleys and spins are related by time reversal symmetry $(K \rightarrow -K, s_z \rightarrow -s_z)$, the spin-splitting must be opposite for the two bands in opposite valleys. Including the SOC, the band structure of the K and $-K$ valleys are shown in illustrated in Fig 2-3. The spin splitting of the conduction band is only ~15-30 meV[45], (the splitting comes from higher order corrections arising from contributions from p_z, d_{xz}, and d_{yz} orbitals), while the VB spin splitting of 0.2 – 0.5 V is large compared to the other energy scales of the system. Note that the sign of the conduction band splitting depends on the metal atom, such that spin of an electron at the conduction band edge is the same (different) as the electron at the VB edge for Mo (W) species of MX_2[46].

The spin-orbit coupling effects result in unprecedented properties for MX_2. The combination of broken inversion symmetry and spin-orbit coupling gives rise to the interesting situation that an electron moving from one valley to another not only requires a large change in momentum, but also a flip of spin (or large change in energy). Intervalley scattering is thereby suppressed, giving rise to the so-called 'spin-valley locking effect' where the $\pm K$ electrons have their spin degree of freedom locked to the valley index[45] $\left(s_z = \frac{1}{2}\tau\right)$. Including the SOC the effective Hamiltonian for MX_2 is given by $H \sim at\left(\tau\sigma_x k_x + \sigma_y k_y\right) + \frac{\Delta}{2}\sigma_z - \lambda\tau\frac{\sigma_z - 1}{2}s_z$, where 2λ is the magnitude of the spin splitting of the valence band and s_z is the Pauli matrix for the electron spin[23]. This ignores the spin splitting of the conduction band, which can be included by adding in a fourth term of a similar form as the third.

2.2 Valley optical selection rules

The lack of inversion symmetry in MX_2 has important consequences for the light-coupling of interband electronic transitions at the $\pm K$ points. In an atom, the allowed and forbidden optical transitions are derived by considering the angular momentum conserving transitions according to the orbital magnetic moments of the electron energy eigenstates. The optical transitions in a solid are similar, but the intracellular rotation of the Bloch electrons can take on their own orbital magnetic moment due to Berry curvatures of the bands[23]. The broken inversion symmetry in MX_2 allows nontrivial Berry curvatures which must be opposite for opposing valleys, since they are related by time reversal. The Berry curvatures give the band edge Bloch electrons a

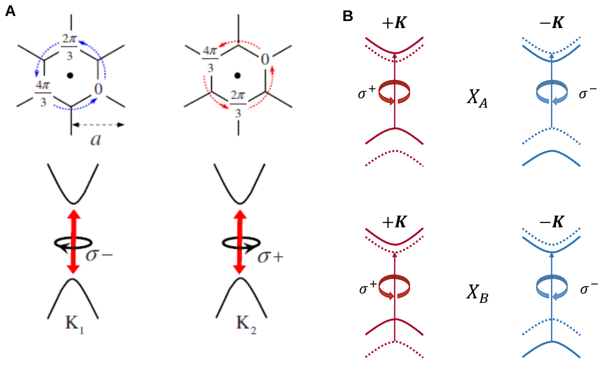

Figure 2-4 | Valley optical selection rules for MX_2. (A) The valley-contrasting Berry curvature leads to circularly polarized light coupling for the K and –K valleys. **(B)** Optical selection rules for the A exciton (top) and B exciton (bottom) in the $\pm K$ valleys of MX_2.

valley orbital magnetic momentum, which causes the optical dipole coupling to light of $+\sigma$ in the +K valley and $-\sigma$ in the –K valley (Fig. 2-4A). Time reversal symmetry dictates that the light emission from different valleys will have opposite helicity. This defines a set of optical selection rules where one can excite electron-hole pairs localized within a single valley, i.e. valley excitons, by controlling the helicity of light. Further, since each valley possesses two excitons, marked as X_A and X_B in Fig 2-4B, it is possible to address either state by tuning the excitation energy. Considering the spin-valley locking effect, the unique band structure and optical coupling of MX_2 made it an exciting new playground for optics researchers in solid state physics.

2.3 Valley exciton properties

The valley excitons in MX_2 have been widely studied in the past decade, with researchers confirming the optical selection rules by demonstrating the valley-specific optical pumping of excitons[45,47]. For example, the monolayer WSe_2 illuminated with circularly polarized light is seen to emit light with the same helicity as the pump laser[48], as shown in Figs. 2-5A & B. The two valleys can also evolve coherently when excited with linearly polarized light, as was shown experimentally in monolayer WSe_2, where the photon emission is linearly polarized along the axis of the excitation laser, as shown in Figs. 2-5C & D. Since linearly polarized light is equivalent to an equal superposition of light with positive helicity σ^+ and negative helicity σ^-, the excitation populates both valleys equally. The emission of light along the same axis as the excitation indicates that the underlying phase relation between the two valley populations is maintained, which demonstrates valley exciton coherence[49,50]. These results confirm the valley-contrasting circular dichroism and show that the valley excitons in monolayer TMDs enjoy robust

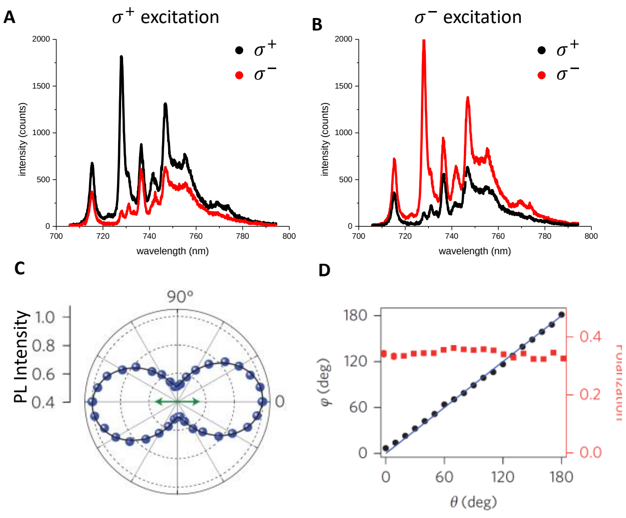

Figure 2-5 | Valley exciton photoluminescence. Polarization resolved PL (circular basis) from monolayer WSe_2 pumped with light of **(A)** positive helicity and **(B)** negative helicity. **(C)** Polar plot of the PL intensity from monolayer WSe_2 under linearly polarized excitation (orientation shown in green). **(D)** Linear polarization axis of the monolayer WSe_2 emission (ϕ) as a function of the excitation laser linear polarization axis (θ).
C and D are reproduced from Jones, et al. *Optical generation of excitonic valley coherence in monolayer WSe_2.* Nat Nano 2013.

protection of the valley degree of freedom via the spin-valley locking effect.

2.4 Charged excitons

The introduction of free charge into semiconductors is the backbone for semiconductor devices of all sorts. The electrostatic doping of 2D materials using simple field-effect electronic devices has shown to be remarkably effective. In monolayers of TMDs, the introduction of free charge carriers, both electrons and holes, is shown to give rise to stable states at lower energies than the free exciton, as shown in Fig. 2-6A. The charged states (X^+ and X^-) have been attributed to the formation of three-particle states called trions; the binding of an additional charge carrier to a free exciton[51,52]. Based on the band structure of the MX_2 monolayers, a host of different trion states are possible (c.f. low energy peaks in Fig. 2-5A). The fine structure of these states provides a quantitative assessment of the exchange energy differences between the different trion configurations[50,53,54]. The rich physics of charged excitons is an ongoing research area in the monolayer TMD community.

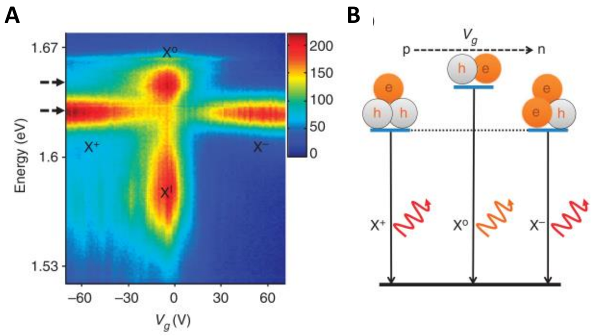

Figure 2-6 | Trion formation in monolayer TMD.
(A) Photoluminescence from monolayer MoSe$_2$ at various back gate voltages showing the emergence of lower energy, charged trions. **(B)** Illustration of the three-particle trion states as a function of doping.
Reproduced from Ross, et al. *Electrical control of neutral and charged excitons in a monolayer semiconductor*. Nat. Comm. 2013.

2.5 Bright and dark excitons

The opposite sign of the spin-splitting of the conduction band for monolayers of WSe$_2$ and MoSe$_2$ results in important differences in the exciton properties of the two materials. In MoSe$_2$ monolayers, the conduction and valence band electrons have the same spin, while in WSe$_2$ monolayers they have opposite spins. This means that the ground state exciton in WSe$_2$ is optically dark (spin-forbidden), while in the MoSe$_2$ the ground state exciton is optically bright (spin-allowed), as shown in Fig. 2-7A. The large oscillator strength of the spin-allowed transitions causes the bright excitons to have short lifetimes (~1-10 ps), but the lifetime of the dark excitons can be orders of magnitude longer. This leads to important differences in the population dynamics of the bright and dark states in the tungsten and molybdenum based TMDs. This subtle difference causes dramatic differences in the optical response of the two materials, e.g. it explains why the PL efficiency of WSe_2 decreases at lower temperatures while $MoSe_2$ becomes brighter[55,56]. There are also momentum-dark excitons, which arise when the electron and hole are located in different valleys in the momentum space, e.g. the intervalley exciton shown in Fig 2-7B.

The dark excitons in WSe_2 and WS_2 have generated much interest because they are long lived states where the valley degree of freedom is protected. However, careful theoretical treatment has shown that the lowest energy dark states are not completely dark, but that these spin-flip transitions are enabled by the spin-orbit coupling. Treating the spin-orbit coupling as a perturbation, the dark exciton acquires a finite dipole in the out-of-plane direction[57]. This has been verified experimentally, through the application of in-plane magnetic fields[58,59], coupling to surface plasmon-polaritons[60], or more simply, by collecting the light emitted in the plane of the monolayer[57] (see Fig. 2-7C). The location of the dark exciton is well resolved by these experiments, lying ~40 meV below the neutral bright exciton and just below the trion in the monolayer WSe_2, as shown in Fig. 2-7D. Additionally, the mixing of the inter- and intra-valley dark excitons breaks their degeneracy, as was shown in a recent work[61].

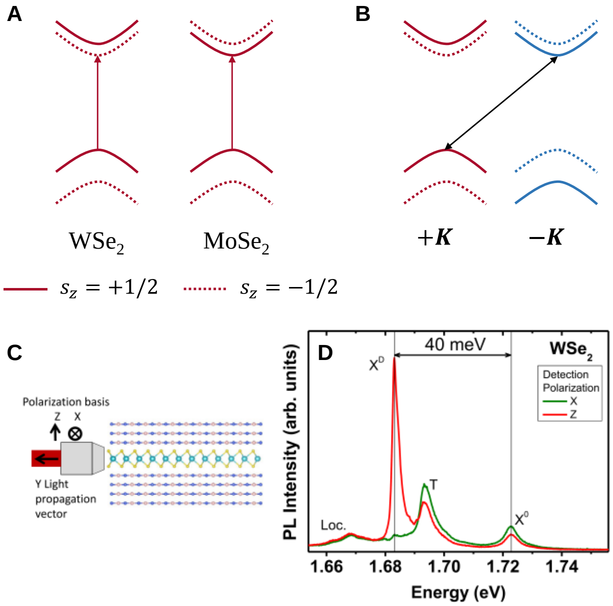

Figure 2-7 | Dark excitons in monolayer TMDs. **(A)** Illustration of the lowest energy exciton in WSe_2 and $MoSe_2$ monolayers. The transition shown in the WSe_2 is spin-forbidden, while in the $MoSe_2$ it is spin-allowed. **(B)** Illustration of the momentum indirect intervalley exciton in monolayer WSe_2. **(C)** Side angle collection geometry for measuring exciton with out-of-plane dipole. **(D)** PL from monolayer WSe_2 measured from normal (x polarization, green) and parallel to the crystal plane (z polarization, red), clearly showing the dark exciton emission lies primarily in the plane.
C and D are reproduced from Wang, et al. *In-Plane Propagation of Light in Transition Metal Dichalcogenide Monolayers: Optical Selection Rules.* Phys Rev Lett **119** (2017).

2.6 Quantum emitters in monolayer TMDs

An additional aspect of the monolayer TMDs is that defect-bound excitons have demonstrated key characteristics of single quantum emitters, which are highly desirable in the fields of quantum optics and quantum information science[62]. A number of studies have shown that localized excitons in monolayer TMDs show low energy optical emission with narrow linewidths and polarization properties that are characteristic of quantum dots in III-V systems. Second-order temporal correlation measurements reveal that the bound excitons show strong anti-bunching, i.e. are single quantum emitters[63-66]. Meanwhile, the point defects can be spatially and spectrally controlled by strain engineering[67-70], and the quantum light can also be generated on-demand through electrical pumping[71-73], e.g. via quantum LED. Based on these results, it is clear that the monolayer TMDs are also promising solid state sources of quantum light.

2.7 Outlook and limitations of monolayer TMDs

The rich exciton physics in the monolayer TMDs is a tantalizing platform for potentially breakthrough technologies based on the valley degree of freedom. However, there are several complications that limit these possibilities, including the short population and valley lifetimes of the valley excitons, the latter of which is limited by strong electron-hole exchange interactions[74]. Moreover, the quantum emitters described in 2.5 are more like quantum dots in III-V semiconductors, rather than free excitons in monolayer TMDs. This is because any asymmetry in the trapping potential breaks the rotational symmetry of the monolayers, which means the exciton polarization properties are no longer dictated by the valley degree of freedom. Thankfully, researchers like myself are not easily dissuaded, but persistent and stubborn when it comes to solving problems. Fortunately, developments in van der Waals heterostructures opens up a new avenue for creative solutions to overcome these limitations.

Chapter 3: Fabricating van der Waals Heterostructures

The ability to stack different 2D materials into arbitrarily complex van der Waals heterostructures marks a new frontier in materials science engineering and condensed matter physics. The opportunity to engineer the electronic and optical properties of these synthetic materials is truly unprecedented, which makes them provocative platforms for fundamental research in physics, as well as next generation device engineering. The following section provides a detailed description of the process of assembling these van der Waals heterostructures, as well as the methods used for fabricating electrical contacts to them.

3.1 Isolating 2D materials

The first step in fabricating any vdW heterostructure is to isolate the constituent materials. There are essentially two methods by which this is accomplished (Fig. 3-1). The first is by physical or chemical vapor deposition, which typically involves the heating of relevant source materials upstream of a target substrate in a tube furnace. The second means for isolating 2D materials is through the micromechanical exfoliation of bulk crystals onto various substrates. For all the vdW heterostructures involved in this thesis, the latter technique is employed and, while I will describe the specific procedures for graphene, hexagonal Boron Nitride (hBN), $MoSe_2$, and WSe_2, these techniques can also be used for a wide variety of other layered materials.

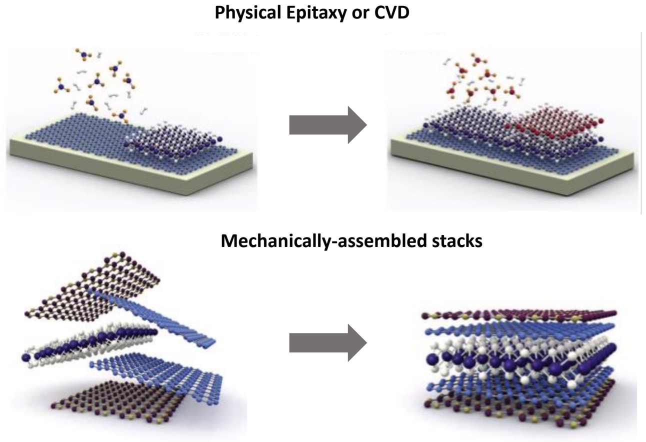

Figure 3-1 | Fabrication of van der Waals heterostructures. Arbitrarily complex layered structures can now be grown (top) using self-assembly methods, or assembled (bottom) using techniques developed during studies of graphene.
Graphics reproduced from Castro Neto, et al. *2D materials and van der Waals heterostructures.* Science. **29** Jul 2016.

Prior to exfoliation of the bulk crystals, substrate materials are chosen and prepared to optimize the yield of high quality flakes of 2D materials. For TMDs, the preferred substrate is 285 nm of thermally grown SiO_2 on top of a Si wafer. My experience does not indicate that wet- or dry- grown oxide performs any better than the other for optimizing the yield of monolayers from exfoliation. The oxide thickness optimizes the thin film interference effects for these materials, making it possible to identify the layer number of ultrathin materials by their optical contrast[75,76]. After little experience, the identification of monolayers, bilayers, and trilayers becomes fast and reliable. For identification of thin layers of graphene and hBN, 90 nm thick oxide provides slightly better contrast. For $MoSe_2$ and graphene, the size, quantity, and cleanliness of monolayer flakes is greatly increased by pretreatment of the wafers by oxygen plasma (50W for 5 min) immediately before exfoliation[77]. However, I find that this treatment does not have the same effects for WSe_2 and hBN, and bare clean wafers are preferred for these materials. It is also possible to use other substrates if one has particular reasons for doing so. For example, exfoliation on a layer of Au (from evaporation or sputtering) can isolate monolayer flakes that do not adhere to the SiO_2, as well as yield enormous flakes of monolayer TMDs (~0.5 μm or larger on a side). However, they may adhere so strongly that they cannot then be removed.

Once the substrates are prepared, a few bulk crystals are carefully placed on the sticky side of a ~2-inch sheet of scotch tape. It is beneficial to form a row or two across the tape and to have the flakes lay flat on the surface, covering ~33% of the row with crystal. The edge of the tape without any crystal is then bent over to touch the crystals, then retracted to cleave the bulk crystal. This should be done gently, and repeated approximately 6-10 times, taking care to always place clean tape against fresh crystal. It is important to avoid peeling too many times, and it is optimal to cover ~66% of the tape surface with crystals. Once the tape is prepared as described, it is inverted, and the freshly cleaved crystals are carefully placed in contact with the substrate material. The entire tape is then made to be flush with the wafer by carefully dragging a tweezer edge across the top of the tape, applying a very small amount of pressure. If the oxide wafer was treated with oxygen plasma, the wafer is then baked on a hotplate at a temperature of ~100-130 °C for ~60 s[77]. The tape is then slowly peeled away at a consistent speed to conclude the exfoliation process.

The next step in isolating the 2D materials is to search the substrate with exfoliated material on it under an optical microscope. Careful inspection will reveal bunches of thin flakes of varying thickness covering the surface, a few of which will be monolayers. Depending on the desired architecture, one may want to find flakes of different geometries, as well. For each sample found on the substrate, several microscope images are taken at different magnifications to aid in locating it during subsequent steps. I prefer to only use pictures, rather than scratching the substrate surface (e.g. with a diamond scribe), as this avoids any possible contamination from dust particles produced from the scratching.

Once suitable flakes have been found, it is critical to verify that their surfaces are pristine and that they have the desired thickness. The surface of each candidate flake is characterized by atomic force microscopy (AFM) to ensure that it is clean, and of suitable thickness for the target purpose. Considering the sensitivity of 2D materials to their surrounding environment, only pristine flakes should be used to make the highest quality devices. The flakes should be stored in inert environment, e.g. dry nitrogen or under vaccum, to prevent their degradation while preparing for device fabrication.

It has become a common practice to encapsulate many of the materials between relatively thick (20-40 nm) hBN, which provides several device advantages[26]. The atomically flat surface of the hBN minimizes the out-of-plane disorder of encapsulated samples while also protecting them from degradation from the ambient environment. Furthermore, the hBN is a wide bandgap insulator, which makes it an ideal gate dielectric. Graphene is also often used as an atomically smooth gate electrode. However, the single layer of graphene can often crack or break during subsequent assembling of the final device, so using multi-layered graphene can be advantageous.

3.2 Transfer of 2D materials

It still amazes me that it is possible to pick up the monolayer materials from their substrates and to vertically stack them in such a way that they are not destroyed. The techniques for achieving this goal have developed and evolved over the last decade. Here, I describe the state-of-the-art procedures used in the Xu Laboratory to fabricate ultra-clean vdW heterostructures, which routinely achieves <1 um positioning precision and ~1° precision in the rotational alignment of the heterostructure layers.

Once all the constituent materials have been found and characterized, the process of transferring them onto one another begins. It is prudent to have a backup sample for each layer in the transfer. Prior to fabrication, the device architecture should be carefully planned. The preferred technique for this is to load the optical images of each flake into a computer software program, such as KLayout, or Adobe Illustrator, and precisely outline them using user-defined polygons having ~50% transparent coloring. Once all the different layers are individually outlined, the generated polygons can be rotated, positioned, and overlaid to plan the final device architecture. This will also define the order in which they are transferred, according to a top-down approach. I prefer KLayout if the final device will have electrical contacts, since this program may also be used to generate the pattern file for electron beam lithography. Do not discard the images in the file, as the extraneous flakes on the substrate may also provide reference points that can be used for precision triangulation during the subsequent transfer of the materials. Furthermore, it is critical that different areas of the device are not shorted to one another by bulk flakes from the other materials, which can easily be seen by overlaying the pictures.

To remove each flake of material from its substrate, the visco-elastic polymer stamping technique is used[78]. This process takes advantage of the stronger vdW forces between the flakes and a suitable polymer material than the SiO_2 substrate, which causes them to preferentially adhere to the polymer instead of the substrate. When the polymer is then peeled away from the substrate, the flakes will remain attached to the polymer. The ‘stamp’ consists of a thin layer of polycarbonate placed on top of a relatively thick polymer, both of which are transparent. The thin layer of polycarbonate (other polymer can also be used, e.g. poly-propylene carbonate, poly-methyl methacrylate, etc.) is the polymer that comes into contact with the 2D materials, since it is very ‘sticky’ for each of the constituent materials (TMDs, graphene, and hBN). The polycarbonate has a glass transition temperature of ~165-180°C, is highly deformable, and leaves very little residue when dissolved in chloroform. The thick polymer is Poly-Dimethylsiloxane (PDMS), because it is stable at temperatures well above 200 °C, has suitable compressibility, and can be easily formed into arbitrary shapes.

I prefer to use ‘dome-stamps’ to perform the transfer of 2D materials, as it offers a number of advantages over that of flat stamps. The dome-stamp forms an optical lens that improves the image quality when looking through the stamp, making it easier to see the individual flakes during transfer. The high radius of curvature also means that the area of the dome-stamp that touches the substrate is circular and, as the stamp is pressed into contact with the substrate, the contact area exhibits reliable and repeatable radial expansion. This allows one to place the desired 2D material very close to the center of contact between the dome-stamp and substrate, minimizing the total area of the polymer in contact with the substrate. Importantly, this allows the flakes on the dome-stamp and substrate to be positioned as close to one another as possible before they touch. This provides certain advantages for the relative positioning of the flakes during the transfer, since there is some relative motion of stamp and substrate as the contact area increases, which is a significant issue with large flat stamps. All these advantages cause dome-stamps to excel in terms of positioning precision.

The dome-stamp is prepared as follows. The PDMS is prepared from Sylgard 184 kit, with 10:1 ratio. After mixing the two components very well, the solution is poured into a clean, flat, beaker, to a thickness of ~2-3 mm. The beaker is covered and placed under vacuum for ~20-30 min to remove air bubbles. Then the beaker is placed in a curing oven at ~70 C for 24 hours. A small metallic tube with honed edges and a diameter of ~5 mm is then used like a cookie cutter to remove cylinders from the PDMS film. These cylinders are placed into a clean glass beaker, where they will adhere to the surface. A second batch of PDMS is then prepared. Using a pipette, small drops of liquid PDMS are placed on top of each solid PDMS cylinder in the beaker. The droplets should cover the entire top of the cylinders, being held from spilling over the edges only by surface tension. The beaker is then covered, placed under vacuum, and baked, as described above. The resulting dome-topped pillars of PDMS are transparent substrates that will subsequently be covered by a thin layer of polycarbonate. They are durable and reusable – just wash with acetone or IPA between uses.

To produce a thin sheet of polycarbonate (PC), first a solution is made by dissolving ~10% bisphenol-A polycarbonate (Alfa Aesar) in chloroform (by weight) in a clean covered beaker, using a magnetic stirrer at ~30° C for 6-12 hours. After complete dissolution, the solution is poured into a light-shielded container (brown glass) and stored in a dark, cool, and dry place. The solution is dispensed using a clean glass pipette (the chloroform can dissolve some plastic pipettes). One can then spin the PC onto a glass slide, or put a few drops of the PC in between two clean glass slides and then slide them apart. Let the chloroform evaporate from the resulting thin films of PC, typically >5 min. Take care to keep the surface of the PC clean, as this will be the material that comes into contact with your sample flakes. Use a sharp hole-punch to cut a ~1 cm circle out of a piece of double-sided tape and adhere across the center of the end of the glass slide. Then place a single PDMS dome into the center of the double-sided tape. Next, use the same hole-punch to remove a circle from a piece of scotch tape. Push the scotch tape onto the dry PC film using tweezers (much like pushing the tape to the substrate during exfoliation). Using a razor, cut the PC along the edges of the tape and peel the tape away so that a thin film of PC is suspended across the hole in the scotch tape. Carefully center and drape the PC film over the PDMS dome and push the PC into contact with the double-sided tape, again pressing the scotch tape with PC attached to it into the double-sided tape with a tweezer. Inspect the finished dome-stamp under a microscope to ensure the apex of the dome is clean before using. The finished stamps can be stored for several weeks or even months before their use.

The physical removal of each layer and the assembling a vdW heterostructure are performed on a ‘transfer stage’ (see Fig 3-2). The transfer stage in the Xu Laboratory is a converted electrical probe station with optical microscope. A thermally-controlled block of aluminum (i.e. an embedded heater, surface temperature sensor, both connected to an external servo-controller), with center vacuum chuck hole, has been added and placed underneath long-working distance microscope objectives. The slide, with attached dome-stamp, is attached to a micro-manipulator that is mounted on the probe station side stage.

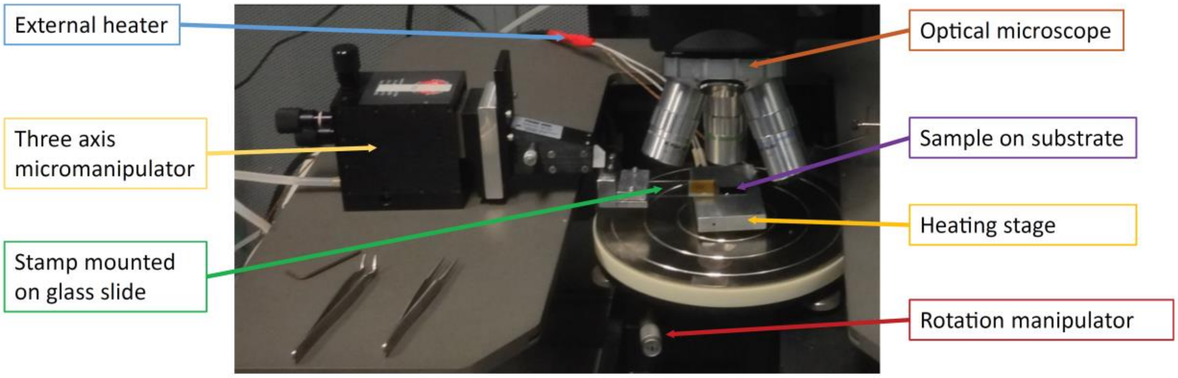

Figure 3-2 | Transfer stage for fabricating van der Waals heterostructures.
The converted probe station used to fabricate vdW heterostructures in the Xu Lab. The three axis micromanipulator can be swapped out for a three axis piezo-stage that can be controlled remotely for improved precision of the transfers.

To test the stamp prior to use, place a clean, blank substrate (not one freshly treated with oxygen plasma, since this will stick very strongly to the stamp and it will not release) on the vacuum chuck and bring the thermal stage to a temperature of ~110-150°C, which helps prevents water from accumulating on the sample surface. Locate and center the apex of the dome-stamp in the field of view of the microscope, then focus on the substrate through the stamp. Raise the focal point of the imaging system slightly, and lower the stamp until it comes into focus, just above the substrate. Repeat this process slowly until the stamp comes just into contact with the substrate, i.e. touch-down occurs. Newton’s rings will be visible just before the stamp touches the substrate. Center the ‘touch-down spot’ in the field of view. Next, lower the stamp slowly until the diameter of the PC on substrate is ~500 um. This area should be the maximum contact area between the stamp and substrate in the subsequent use. Wait a few minutes and then slowly retract the stamp until it releases from the substrate. A suitable stamp will exhibit negligible deformation or substrate pinning and release from the substrate in a smooth manner.

The vertical position of the stamp relative to the substrate can be accomplished by two means, (1) thermal expansion of the heating stage, or (2) mechanical control of the entire stamp via piezoelectric micro-manipulators. I prefer the latter, as it allows the sample temperature to be constant throughout the pick-up and for the automation of approach and retreat speeds. Once the stamp has been successfully tested, replace the blank substrate with the first sample to be picked up.

The process of picking up each flake of the heterostructure proceeds just as described above for testing the stamp. During the first flake pick-up, place the sample just outside of the minimum area that the stamp and substrate have when just in contact with one another, i.e. the ‘touch-down’ spot size. This way, the flake will not be the first area to encounter the stamp. The contact force between stamp and stage adds stability to the transfer process, as well as control over the direction in which the PC spreads to cover the flakes during the pick-up process, which can help to avoid large clusters of bulk material or tape residues. Digital control and automation of the micromanipulator positioning allows for standardized approach and retraction speeds to optimize the pick-up success rate. The success rate for picking graphene and hBN flakes directly with the stamp is very high at 130° C.

Subsequent pick-ups can be initiated following the same approach. The higher temperature of the transfer will improve the cleanliness of the final interfaces, but too high of temperature can weaken the PC layer so that it deforms or melts to the substrate. I have seen that layers will self-arrange at higher temperatures (~150°C), which may cause some variation from the desired architecture. In some cases, the van der Waals forces between the materials on the stamp and substrate can be strong enough to pull a layer up off the substrate without touching the surface with the polymer, laminating the two layers together. I believe this is the cleanest transfer achievable by these techniques.

For precision positioning of the flakes, slowly bring the stamp very close to the substrate. If the stability of the stage is sufficiently good, it will be possible to have both the sample on the stamp and the flake on the substrate in the same focal plane, which enables their simultaneous imaging. Carefully adjust the position of the stamp (or substrate) to align the flakes. Rotational control over the substrate mount adds the important ability to control the rotational alignment of the flakes. For high precision alignment, save live images of the two flakes using the optical microscope. Load the images into the design software and compare with the desired flake positioning (this will likely involve a slight resizing of the images due to the magnification added by the dome stamp). Triangulation with substrate pieces surrounding the desired flake can increase the rotational precision significantly.

Once the entire heterostructure is assembled on the stamp, affix a clean substrate to the vacuum chuck and increase the temperature to ~175° C. Slowly, but steadily, bring the stamp into contact with the substrate, going well beyond the edges of the heterostructure, just beyond the original test area. The temperature is above the glass transition of the PC, so it should spread differently and have a squeegee effect on the heterostructure, driving out the contaminants[79]. Wait a couple of minutes, then very slowly retract the stamp, paying careful attention to the edges of the PC that is now melted onto the substrate. If the edges of the PC begin to retract, following the stamp, lower the stamp back down to spread the PC and then increase the temperature by ~5° C. When the thin layer of PC detaches from the PDMS, the change in interface will be seen as a dark line that crosses the melted down region. Once this happens, continue to slowly retract the stamp, again watching the edge of the PC on substrate. The thin film may form tendrils between the PC on the substrate and on the PDMS. These will eventually melt and/or rip away to leave the sample on the substrate, covered by the thin layer of PC. Once it is clear that the PC has melted to the substrate and is completely detached from the PDMS dome, remove the stamp assembly.

Once the transfer is finished, it is best to let the sample gradually cool to room temperature. Rather than immediately removing it from the heating stage, remove the stage heat and let it cool to <70° C before removing the sample. To wash away the PC, immerse the sample in a bath of chloroform for ~6-12 hours, followed by a second chloroform bath for ~1-2 hours, and then finish with ~1 hour bath in isopropyl alcohol (IPA). Take great care to ensure that the chloroform never dries on the sample, as this will leave residues that are extremely difficult to remove. This is best achieved by constantly squirting fresh chloroform (IPA) onto the tweezers and sample as it is removed and transferred to the next bath of chloroform (IPA). Immediately after removing the sample from the IPA bath, dry it using dry nitrogen gas. Finally, obtain a high quality AFM of the completed device and take several high resolution photos (both bright and dark field) for possible publication data.

3.3 Fabricating electrodes to vdW heterostructures

The ability to control the Fermi level in 2D vdW devices requires the precise deposition of electrodes onto specific layers and regions of the heterostructure. Conventional electron beam lithography (EBL) and metal evaporation are established techniques that are suited to achieve this goal. However, steps must be taken to ensure precision alignment of the pattern to the device. In the following, I describe the processes used in fabricating a wide assortment of vdW devices.

There are two different types of electron beam lithography systems, dedicated EBL systems, and the hybrid scanning electron microscopes (SEM) with EBL functionality. The former systems are typically used for nanophotonic devices and nanoscale mask generation, have high accelerating voltages, and can achieve extremely small feature sizes (~10 nm). However, these systems are typically rather poor imaging systems compared to SEMs. The pattern alignment on the dedicated EBL systems is usually achieved by prefabrication of metallic alignment markers onto the final substrate on which the vdW device is melted down onto. The alignment and patterning of the resist is a standard process on these machines. However, the extremely high precision of the pattern alignment and small feature size is rarely necessary for vdW devices. For feature sizes greater than ~100 nm, hybrid SEM/EBL system are a more cost-effective means of creating customized vdW devices. The following procedure was developed using a TESCAN Vega SEM using a LaB_6 emitter with 30 kV accelerating voltage.

The challenge in the converted SEM systems is the precise alignment of the pattern to the device, which is defined by the flake position and architecture of the vdW device. A reliable means of achieving the alignment comes from a combination of optical images and SEM define alignment marks. After washing the polymer residue from a completed vdW heterostructure, AFM can be used to characterize the surface cleanliness and get a precise topological map of the sample. The next step is to spin a positive-tone resist on the sample. A standard recipe that works for many situations is a single ~400 nm thick layer of poly (methyl)-methacrylate in anisole (A6 PMMA 950 m.w. from MicroChem) spin-coated on the substrate (~4000 rpm for 60-90 s, baked at 180° C for 180-300 s). After spin-coating the resist mask, the wafer is cleaved down to a size of ~1 cm x 1 cm (this avoids the SiO_2 dust from contaminating the surface), preferably with the vdW heterostructure centered between sharp straight edges of the wafer. Using sharp tweezers, scratch small lines into the PMMA near the corners of the substrate. The resist is now prepared for electron beam exposure.

To locate the sample on the substrate, take one image (or several overlapping images) using the optical microscope that simultaneously include the scratched areas of the PMMA and the sample. The combination of the sharp corners and straight edges of the substrate establishes a reference coordinate system, and the optical images provide a relative translation from a point in that reference system – the end of a scratch or a corner – to the sample. The calibration of the pixel size (μm/pixel) allows one to load the images into computer software (such as KLayout) to determine the relative translation to within a few μm. It is important to get a precise calibration of the pixel size of the optical microscope compared to match that of the SEM, e.g. by imaging a SEM grid sample in both systems and comparing them to one another.

After establishing the coordinate system, the sample is then loaded into the SEM chamber, and rotated to align the substrate edges and establish the coordinate system. Using low beam current, to prevent fast PMMA exposure, focus on the edge of the PMMA scratches in the SEM up to ~10,000 magnification. The high contrast between the bare SiO_2 and the PMMA allows for precise focusing and centering on the edge of the PMMA. The beam is then blanked and the SEM system is put into the EBL mode. A pre-defined alignment pattern, typically consisting of various geometric patterns is then loaded into the EBL system. The relative translation ascertained from the optical images is then used to center the sample in the write field. Write the alignment pattern with a dose of ~300 μC/cm^2, then remove the sample from the SEM system. Develop the exposed PMMA for 60s in 3:7 ratio of cold (~0° C) H_2O:IPA and gently dry with low pressure N_2 gas. The alignment marks should be easily identified under the optical microscope, centered about the sample.

The alignment marks in the PMMA provide a precise coordinate system, located in close proximity to the vdW heterostructure, from which the final contact pattern can easily be aligned to. High resolution optical images, including both the sample and alignment marks, should be saved and then loaded into the pattern generating software to align the contact pattern. Load the sample in the SEM, align the coordinate system and translate to the sample, as done to write the alignment marks. Next, image the alignment marks with low beam current, opening small exposure windows around the alignment marks to prevent dosing areas around the sample. This image is saved and then loaded into the patterning software, providing the registration markers for final pattern alignment. The optical image can be adjusted by a combination of x-y translation, rotation, rescaling of x and y pixels, and tilt along some angle so that it matches the registration marks in the PMMA. If the initial calibration is good, the fit should be excellent with only minor adjustments. The desired resist mask pattern can now be finalized in the software and written using the same dose as above.

After writing the final pattern, develop the exposed resist and inspect the result before proceeding to contact fabrication. If the pattern did not land properly, another short round of EBL can be done to fix the pattern. Rounded edges indicate regions with too high dose (overexposure), whereas regions with thin layer of PMMA (or small dots) are underexposed. Be careful to avoid both extremes. The underexposed regions will prevent the metal evaporation from sticking to the desired region and/or make bubbles underneath the layer of metal that make it very difficult to wire bond to. The overexposed regions are problematic because the rounded edges prevent proper lift-off of the metal region, as a thin continuous film can form between the layer of metal on the substrate and the layer of metal on top of the resist mask. If the pattern is not satisfactory, it is possible to wash the PMMA away in acetone bath (followed by IPA and dry N_2 gas) and to start over.

The samples included in this thesis all have contacts deposited by electron beam evaporation of metals. Some metals, especially Au, have poor adhesion to SiO_2, so it is important to first evaporate a thin layer of a different metal that has strong adhesion to the SiO_2, before evaporating Au. This is known as a ‘sticking layer’ and should have a ratio of ~1:10 with the Au layer of metal (for example, a common recipe is V:Au, 5:50 nm). After e-beam evaporation of the metals, the resist mask is dissolved in either acetone or dichloromethane (DCM) at ~30° C for ~1-5 hours (longer is cleaner). Watch the metal surface over time. Once bubbles form in the metallic film, use a pipette to pulse the liquid onto the pattern to aid the removal of the excess metal that was deposited onto the now dissolved resist mask. Ensure that the metal in solution does not settle on top of the device and that the acetone or DCM never dry on the sample surface. After the ‘lift-off’ of the metal is complete, the sample should be transferred to a final bath of IPA (~30 min) before being dried with low pressure N_2 gas. The final vdW device can now be inspected under the optical microscope and by AFM. Here, the AFM topographic map can identify any residues, while the phase map can distinguish residues on the surface and trapped between the layers. The final device is then silver painted to a chip carrier with electrodes and wire-bonded for measurements.

In some cases, it is not desirable to have the layers in the middle of the vdW heterostructure protruding from the encapsulating materials. The procedure above must be adapted to accommodate such design. The typical means of doing this is to fabricate the vdW device in two halves. The bottom half of the device is pre-fabricated, including metallic electrodes on the surface, after which the top half of the device is carefully positioned and transferred onto the contacts. While this achieves the desired outcome, the increased processing of the surface can often result in less than pristine interface, which can have negative impacts on the device performance. To avoid this, edge contacts can be made to materials by etching through the materials[27]. Typically, the principle etchant is the hBN layers, which can be etched in an inductively coupled plasma etcher with a mixture of O_2:CHF_3 with 4.0:40.0 sccm flow rates and 70 W RF power, which gives about 0.4 nm/s etch rate (special thank you to Bosong Sun for this recipe).

Chapter 4: Electronic structure of TMD heterobilayers

4.1 Band alignment of the TMD heterobilayer

The family of semiconducting monolayer TMDs – $MoSe_2$, WSe_2, MoS_2, and WS_2 – present interesting options for vdW interface engineering because they all have different work functions and band gaps[80,81] (Fig. 4-1A). The band edge alignment of the monolayer TMDs is shown in Fig. 4-1B, which implies a staggered, or type-II, band alignment for the combination of any two different monolayers. This makes the TMD heterobilayer a highly provocative system, since modern computational and communications technologies depend heavily on devices with this architecture. The following discussion focuses on the WSe_2-$MoSe_2$ heterobilayer, but the considerations apply generally to the other possible TMD heterobilayers.

The type-II band alignment of the different monolayers implies that the conduction band minimum (CBM) and valence band maximum (VBM) of the heterobilayer are in different monolayers. For the WSe_2-$MoSe_2$ heterobilayer, this means that electrons (holes) find their energy minima in the $MoSe_2$ (WSe_2) monolayer, separated by significant conduction and valence band offsets (Δ_c and Δ_v), as shown in Fig. 4-1B. In the limit of vanishing interlayer coupling, the heterobilayer band structure is just the simple sum of the band structures of the individual monolayers, which implies that the band edges of the heterobilayer remain at the high symmetry $\pm K$ points. However, the finite van der Waals forces can lead to overlapping electronic wavefunctions in the two materials. The orbital hybridization can cause band structure modifications that can rearrange the energetic positions of the band edges in the momentum space, possibly resulting in an indirect bandgap. Therefore, the impact of the interlayer coupling on the band structure has important consequences for the properties of the heterobilayer.

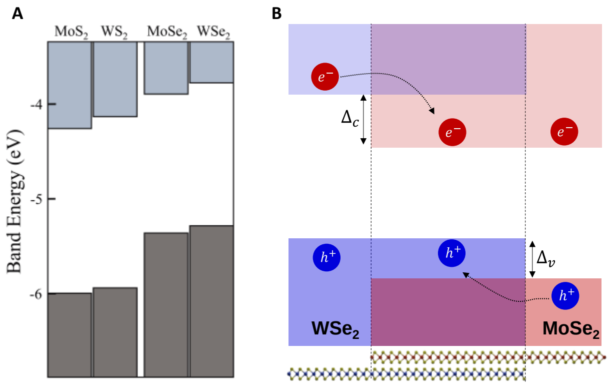

Figure 4-1 | Band alignment of the TMD heterobilayer. (A) Qualitative band alignment of the semiconducting monolayer TMDs. **(B)** The staggered electronic heterojunction in the TMD heterobilayer causes the electrons and holes to find their energy minima in different constituent monolayers. The valence and conduction band offsets are denoted by Δ_v and Δ_c, respectively.

4.2 Interlayer Hybridization

The interlayer hybridization depends on the strength of the interlayer hoppings relative to the band offsets, both of which vary across the BZ. The primary components of the electronic wavefunctions at the $\pm K$ points are orthogonal – d_{z^2} orbitals for electrons at the CBM and $\frac{1}{\sqrt{2}}\left(d_{x^2-y^2} \pm i d_{xy}\right)$ orbitals for the VBM – which suppresses the interlayer hopping strength and implies vanishing hybridization. Therefore, it is expected that the positions of the $\pm K$ points of the heterobilayer will not shift significantly compared to that of the monolayers[22,82-87]. However, away from the $\pm K$ points, the electronic wavefunctions in both layers can have interlayer hopping strengths that are comparable to the band offsets[82-84,88-90], giving rise to large layer hybridization and energetic shifts. An important question is whether these shifts can cause a transition of the heterobilayer bandgap from momentum direct to indirect, since this will have a strong impact on the optical properties.

The previous discussion can be visualized by Figure 4-2, which illustrates the band structure obtained from first-principles for the idealized commensurate $MoSe_2$-WSe_2 heterobilayer

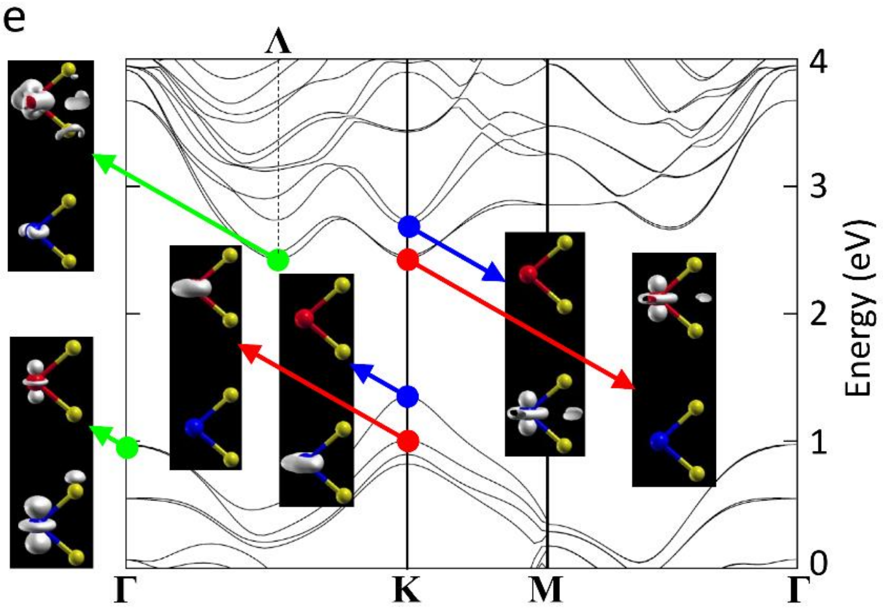

Figure 4-2 | Band structure of $MoSe_2$-WSe_2 heterobilayer. First-principles calculation of the band structure of an idealized (lattice matched) AA-type $MoSe_2$-WSe_2 heterobilayer. The Mo (W) atoms are colored red (blue) and the chalcogen atoms appear in yellow. The insets show the distributions of the electronic wavefunctions at various positions in the momentum space. At **K**, the electrons are primarily composed of the d-orbitals of the transition metal atoms and localized largely to different monolayers. At ***Γ*** and ***Λ***, significant layer hybridization causes the electrons to have significant distributions in both layers. Graphic courtesy of Hongyi Yu, Hong Kong University.

with AA-type stacking (R-type, with both monolayers perfectly overlapping each other vertically, and having the same lattice constants)[91]. Here, the white clouds in the inset graphics show the spatial distribution of the electronic wavefunction at different points in the momentum space. At $\pm K$, the electronic wavefunction of the CBM is largely localized to the d_{z^2} orbitals of the Mo atom, while at the VBM are primarily in $d_{x^2-y^2}$ and d_{xy} orbitals of the W atom. The localization of the charge to different layers reflects the vanishing interlayer hopping strength. However, there are other valleys in the heterobilayer band structure where the interlayer hopping is significant, which causes significant hybridizations. This can be seen from the layer distributions of electrons at conduction band Λ and valence band Γ, which have contributions in both layers.

While most first-principles calculations of heterobilayers agree that the CBM and VBM remains at $\pm K$, it is clear that the layer-hybridization at Γ and Λ depends sensitively on the interlayer separation used in the calculations[83,84,88,90,92]. It is expected that below certain interlayer distances the strong hybridization can cause large energy shifts at Γ and Λ, resulting in the formation of an indirect bandgap. It has also been suggested that the strong interlayer hopping near these positions can mediate the ultrafast interlayer charge transfer seen in the heterobilayer[82], which has been demonstrated experimentally[93-96] but the microscopic mechanism remains an outstanding question in the community.

4.3 Experimental determination of heterobilayer band structure

It is clear from the theoretical calculations that the interlayer coupling can have important impacts on the physics of the heterobilayer. However, there is a fundamental limitation to the first-principles calculations arising from the complexity of dealing with incommensurate lattices, which makes it computationally prohibitive to calculate the band structure for all possible stacking orders of the heterobilayer. While these techniques may prove suitable to describe some chemical vapor deposition (CVD) grown heterobilayers, which may have commensurate lattice structures[97], it is not suitable for those made from exfoliated samples, which are generally incommensurate due to the combination of finite lattice mismatch and the inevitable relative rotation between the constituent layers. Moreover, the van der Waals gap between the layers can be impacted by even the smallest surface adsorbents.

To clarify the theoretical results, we must turn to experiment. Researchers have used microbeam x-ray photoelectron spectroscopy, in conjunction with scanning-tunneling microscopy and spectroscopy to determine that the MoS_2-WSe_2 with finite twist angle exhibits type-II band alignment[98], with both VB and CB edges at $\pm K$. Similar results were found for CVD-grown MoS_2-WSe_2 heterobilayers[99]. In MoS_2-WS_2 the type-II band alignment was also confirmed, with CBM at $\pm K$ but with Γ and $\pm K$ being degenerate at the VBM[100]. The $MoSe_2$-WSe_2 heterobilayer was also studied using μ-ARPES techniques, showing that the VBM remains at $\pm K$ for both samples with closely aligned ($\theta \sim 0°$) and misaligned ($\theta \sim 30°$) crystallographic axes[101]. This study also revealed an elevated band at Γ in the aligned sample (Fig. 4-3C), which is clear evidence of interlayer hybridization. However, the fact that the band edge remains at $\pm K$ is an important result because it has important implications for the optical properties of the TMD heterobilayers. Therefore, despite the computational limitations, the experimental findings are largely in line with the theoretical predictions, and it is expected that the band edges of many TMD heterobilayers remain at the $\pm K$ points.

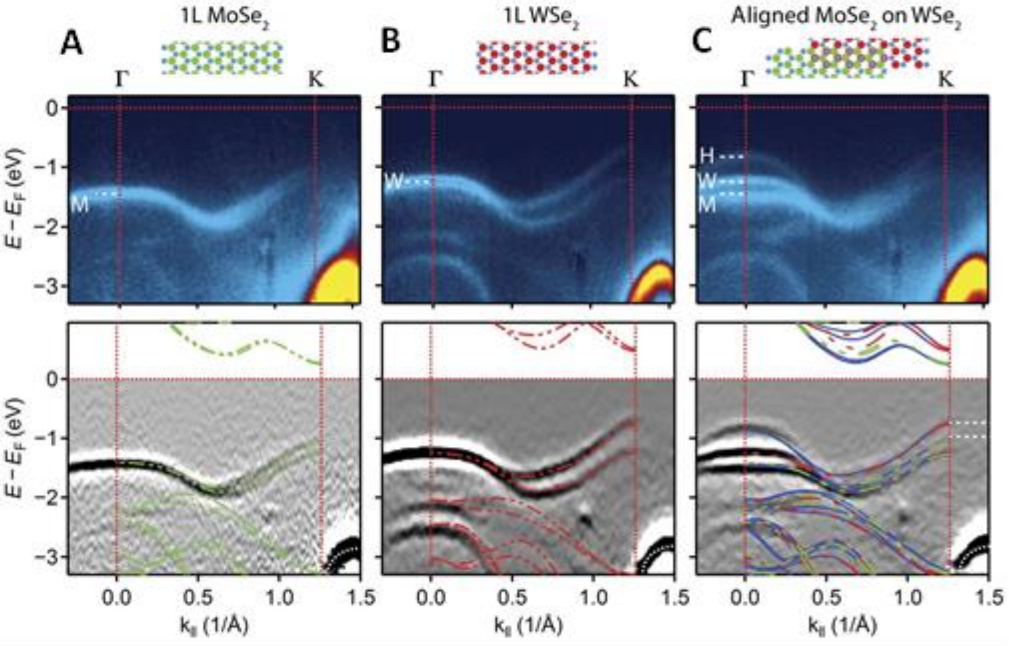

Figure 4-3 | Valence bands of $MoSe_2$-WSe_2 from μ-ARPES Momentum slices along $\Gamma \rightarrow K$ in the three regions of an $MoSe_2$-WSe_2 sample, (top) unprocessed and (bottom) twice-differentiated. The three regions are **(A)** monolayer $MoSe_2$, **(B)** monolayer WSe_2, and **(C)** $MoSe_2$-WSe_2 heterobilayer. The elevated band (H) in the heterobilayer region comes from interlayer hybridization. The white dashed lines in bottom of **(C)** indicate the relative positions of K and Γ, which are separated by ~140 meV. Graphic from Wilson et al. *Determination of band offsets, hybridization, and exciton binding in 2D semiconductor heterostructures.* Science Advances (2017).

Chapter 5: Theory of interlayer excitons

This chapter is devoted to understanding how it is possible that the interlayer exciton may efficiently radiate light despite the momentum mismatch between the band edges of a heterobilayer. The following theory illustrates how, for sufficiently small twisting angle between the layers, the momentum mismatch can be compensated by the interlayer exciton’s momentum, which eliminates the requirement of impurity or phonon scattering for photon emission. The theory was developed by collaborators at Hong Kong University to help explain the results presented in chapter 6 of this thesis. The following text is adapted from Chapter 17 of the textbook 2D Materials, which was first published in 2017 by Cambridge University Press.

5.1 Interlayer excitons in monolayer TMD heterobilayers

Let us consider, in detail, the Coulomb interactions between an electron and hole in different layers of a TMD heterobilayer. Their bound state is referred to as an interlayer exciton, the optical properties of which are of central interest. Taking the reference stacking configuration as that with both the monolayer crystal axes aligned and with the metal atom in the bottom monolayer as the origin, the real-space parameterization of the heterobilayer atomic registry may be entirely characterized by the following: a translation **r** to the transition metal atom in the top layer, a rotation $0 < \theta < 60^{\circ}$ of the top lattice with respect to the bottom lattice, and the lattice constants for the bottom (a_b) and top (a_t) monolayers, as shown in Fig. 5-1A. The real-space twisting angle θ leads to a long-range moiré pattern (Fig. 5-1B), as well as a concentric rotation of the hexagonal Brillouin zones (BZ) of the constituent monolayers, as shown in Fig. 5-1C. The rotation therefore controls the momentum mismatch of the BZ corners,

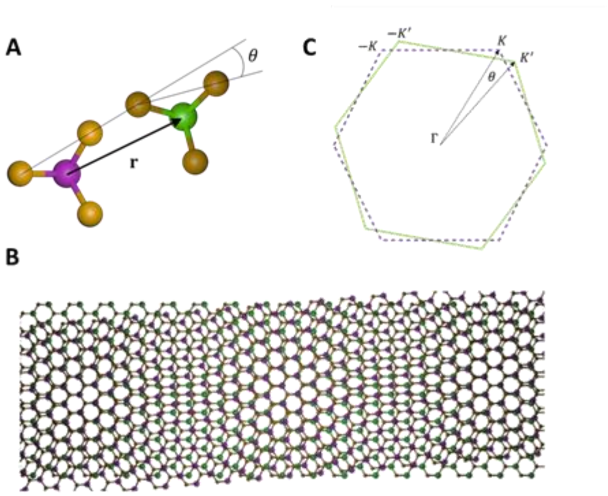

Figure 5-1 | Parameterization of the heterobilayer. (A) The heterobilayer is defined by a relative translation $\boldsymbol{r}$ and rotation θ between a metal atom in the bottom (purple) layer to the nearest metal atom in the top (green) layer. **(B)** Illustration of the first Brillouin zones of the two monolayer crystals rotated by a small angle θ. **(C)** Top-down view of the TMD heterobilayer with small twist angle showing the emergence of moiré pattern.

or K points. For large twist angles the momentum mismatch is large, which suppresses the optical transitions between ±K point charge carriers. For this reason, in the following we only consider the small angle heterobilayers, and for simplicity, we ignore the formation of the moiré pattern and its effects.

Following the pioneering work of Yu, Wang, Tong, Xu, and Yao,[91] we treat the interlayer coupling as a perturbation to determine the light coupling properties of the interlayer exciton. Since the interlayer van der Waals forces are much weaker than intralayer covalent bonding, the monolayers are a good basis for understanding the heterobilayer. The basis states are therefore chosen as the unperturbed Bloch states of electrons in the top and bottom monolayers. Since we are primarily concerned with the optical properties of the interlayer exciton when the twisting angle is small, we will focus on electrons and holes near the band edges, which are located at the corners of the hexagonal BZs of the two layers. The inequivalent valleys are denoted as $\tau\boldsymbol{K}$ and $\tau'\boldsymbol{K}'$, where $\tau, \tau' = \pm 1$ are the valley indices and the unprimed (primed) variables represent the bottom (top) layer of the heterobilayer. In the bottom monolayer, the low energy conduction $|e_{\boldsymbol{k},\tau}\rangle$ and valence $|h_{\boldsymbol{k},\tau}\rangle$ electrons are characterized by their valley index τ and in-plane momentum $\boldsymbol{k}$, measured from the nearest $\tau\boldsymbol{K}$ valley. The states in the top monolayer can similarly be expressed in terms of the primed variables.

The Hamiltonian for the interlayer exciton, in the absence of interlayer coupling, then takes the form

$$\hat{H}^{(0)} = \sum_{\boldsymbol{k}',\tau'} \big(E_e(k') + \Delta_{gap}\big)|e_{\boldsymbol{k}',\tau'}\rangle\langle e_{\boldsymbol{k}',\tau'}| + \sum_{\boldsymbol{k},\tau} E_h(k)|h_{\boldsymbol{k},\tau}\rangle\langle h_{\boldsymbol{k},\tau}|$$
$$+ \sum_{\tau,\tau',\boldsymbol{k},\boldsymbol{k}',\Delta\boldsymbol{k}} V(\Delta\boldsymbol{k})\, |e_{\boldsymbol{k}'+\Delta\boldsymbol{k}',\tau'}\rangle|h_{\boldsymbol{k}-\Delta\boldsymbol{k},\tau}\rangle\langle h_{\boldsymbol{k},\tau}|\langle e_{\boldsymbol{k}',\tau'}|,$$

where E_e (E_h) is the dispersion of the electron (hole), $V(\Delta\boldsymbol{k})$ is the intravalley term of the direct Coulomb interaction, and Δ_{gap} is the interlayer electronic bandgap. Note that the Coulomb interaction here conserves the sum of the electron and hole momenta, as the Umklapp type terms are found extremely weak, and are dropped[91]. The unperturbed interlayer exciton eigenstate is then

$$\left|X^{(0)}_{\mathbf{Q},\tau',\tau}\right\rangle = \sum_{\mathbf{k},\mathbf{k}'} \psi_I(\boldsymbol{k},\boldsymbol{k}')\, |e_{\boldsymbol{k}',\tau'}\rangle|h_{\boldsymbol{k},\tau}\rangle = \sum_{\Delta\mathbf{Q}} \psi_I(\Delta\mathbf{Q}) \left|e_{\tau',\frac{m_e}{M_0}\mathbf{Q}+\Delta\mathbf{Q}}\right\rangle \left|h_{\tau,\frac{m_h}{M_0}\mathbf{Q}-\Delta\mathbf{Q}}\right\rangle \qquad (1)$$

with $\psi_I(\mathbf{r}) \equiv \sum_{\Delta\mathbf{Q}} \psi_I(\Delta\mathbf{Q})\, e^{i\Delta\mathbf{Q}\cdot\mathbf{r}}$ representing the electron and hole relative motion and $\Delta\mathbf{Q} \equiv \frac{m_e\boldsymbol{k}'-m_h\boldsymbol{k}}{m_e+m_h}$. Here, we can see that besides the electron and hole valley indices τ' and τ, an interlayer exciton state is labeled by $\mathbf{Q}$, which is a good quantum number even in absence of translational invariance at general twisting angles (a direct consequence of the fact that the momentum sum of the electron and hole is conserved by the Coulomb interaction). Because of the nearly parabolic band edges of $MoSe_2$ and WSe_2, $\mathbf{Q}$ is also the *kinematic* momentum associated with the center-of-mass group velocity $\langle X_{\mathbf{Q}} | \frac{m_e}{M_0}\dot{\mathbf{r}}_e + \frac{m_h}{M_0}\dot{\mathbf{r}}_h | X_{\mathbf{Q}} \rangle = \frac{\hbar}{M_0}\mathbf{Q}$. Correspondingly, the eigenenergy of the interlayer exciton state is

$$E_X(\mathbf{Q}) = \frac{\hbar^2 Q^2}{2M_0} + \Delta_{gap} - E_B$$

where E_B is the interlayer exciton binding energy.

5.2 Finite momentum light cones

The light-coupling of the interlayer excitons is constrained by momentum conservation. An electron-hole pair at the band edges cannot recombine, since they have finite momentum mismatch given by θ and the lattice mismatch. However, the momentum mismatch between the minima can be compensated by the interlayer exciton's momentum. As shown in Fig. 5-2A, the electron-hole pair $|e_{\boldsymbol{k}',\tau'}\rangle|h_{\boldsymbol{k},\tau}\rangle$ may recombine if $\boldsymbol{k}' + \boldsymbol{k} = -\tau'\boldsymbol{K}' + \tau\boldsymbol{K}$ (note that the hole state $|h_{\boldsymbol{k},\tau}\rangle$ corresponds to the Bloch function $\psi^*_{\tau\boldsymbol{K}-\boldsymbol{k},\mathrm{v}}$). Thus, unlike conventional excitons, which are optically bright at zero kinematic momentum, the interlayer excitons in heterobilayers are bright at finite kinematic momentum $\boldsymbol{Q} = \tau\boldsymbol{K} - \tau'\boldsymbol{K}'$. Including the Umklapp-assisted momentum conservation, interlayer excitons can also recombine in principle at $\boldsymbol{Q} = \tau\boldsymbol{\kappa} - \tau'\boldsymbol{\kappa}'$ where $\tau\boldsymbol{\kappa} = \boldsymbol{\tau K} + \boldsymbol{G}$ and $\tau'\boldsymbol{\kappa}' = \tau'^{\boldsymbol{K}'} + \boldsymbol{G}'$, where $\boldsymbol{G}$ $(\boldsymbol{G}')$ represents all the reciprocal lattice vectors in the bottom (top) monolayer. The positions of $\tau\boldsymbol{\kappa}$ and $\tau'\boldsymbol{\kappa}'$ in the extended zone scheme for the $MoSe_2/WSe_2$ heterobilayer with small twisting angle, where the lattice mismatch is very small $(< 0.2\%)$, are illustrated in Fig. 5-2B. A change in θ corresponds to a concentric rotation of $\tau\boldsymbol{\kappa}$ $(\tau'\boldsymbol{\kappa}')$ along the concentric circles C_n (C_n'). The interlayer exciton light cones are located at $\boldsymbol{Q}_n$ where n is the order of the Umklapp-assisted lightcone, $i.e.$ $\boldsymbol{Q}_0 = \tau\boldsymbol{K} - \tau'\boldsymbol{K}'$ are the main light cones, $\boldsymbol{Q}_{n>0}$ are the nth order Umklapp-assisted light cones which are defined by the momentum mismatch of $\tau\boldsymbol{\kappa}$ on C_n and $\tau\boldsymbol{\kappa}'$ on C_n' (see Fig. 5-2C). From the crystal symmetry, the main light cones for $\left|X_{\boldsymbol{Q},\tau',\tau}^{(0)}\right\rangle$ are related by the $\hat{C}_3$ rotational symmetry: $\boldsymbol{Q}_0$, $\hat{C}_3\boldsymbol{Q}_0$, and $\hat{C}_3^2\boldsymbol{Q}_0$. The light cones at $-\boldsymbol{Q}_0$, $-\hat{C}_3\boldsymbol{Q}_0$, and $-\hat{C}_3^2\boldsymbol{Q}_0$ are found from time reversal and correspond to the state $\left|X_{\boldsymbol{Q},-\tau',-\tau}^{(0)}\right\rangle$.

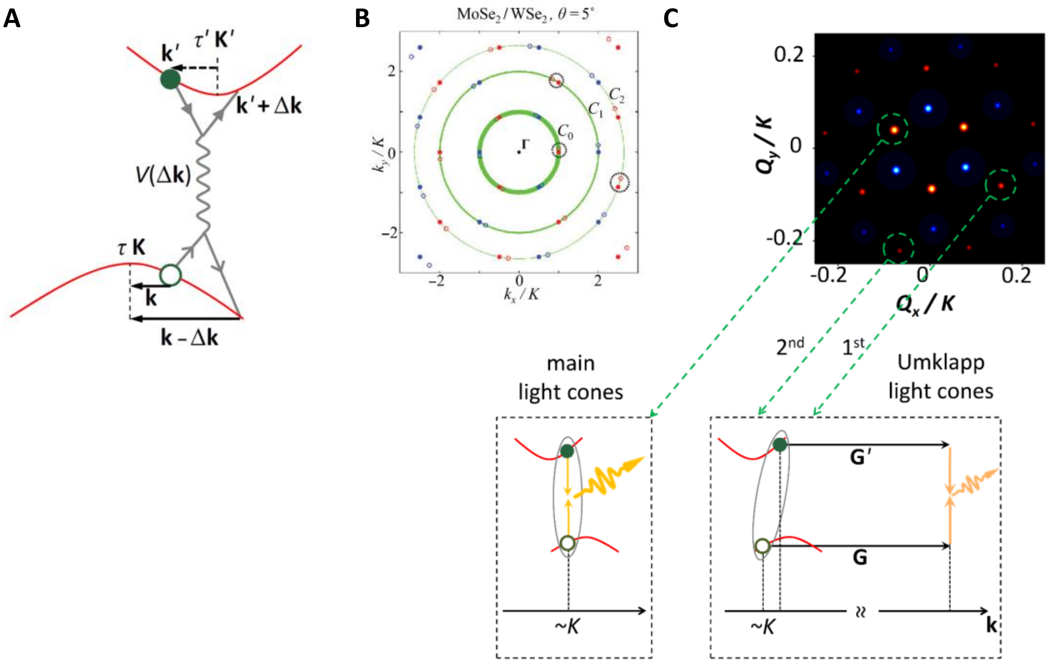

Figure 5-2 | Finite momentum light cones of interlayer exciton. **(A)** The light coupling of the interlayer exciton with momentum mismatch Q_0. **(B)** Positions of the valley in the top (dots) and bottom (circles) layers in the extended zone scheme for the MoSe$_2$-WSe$_2$ heterobilayer with $\theta = 5°$. **(C)** The lightcone positions in the phase space of $\boldsymbol{Q}$. The main light cones appear at $\boldsymbol{Q_0}$, while $\boldsymbol{Q_1}$ and $\boldsymbol{Q_2}$ correspond to the Umklapp-assisted momentum conservation, as shown in the inset. The brightness of the light cones indicates the relative strength of the corresponding optical dipole.

5.3 Interlayer exciton recombination pathways

Having the interlayer exciton wavefunction in the absence of interlayer coupling, we now introduce the interlayer hopping of electrons and holes $(\hat{H}_T)$ as a perturbation. $\hat{H}_T$ can hybridize the Bloch functions in the two layers, and the corrected interlayer exciton eigenstate, is

$$\left|X_{\boldsymbol{Q},\tau',\tau}^{(1)}\right\rangle = \left|X_{\boldsymbol{Q},\tau',\tau}^{(0)}\right\rangle + \sum_{\boldsymbol{q}'} \frac{\left\langle X_{\tau',\boldsymbol{q}'}\middle|\hat{H}_T\middle|X_{\boldsymbol{Q},\tau',\tau}^{(0)}\right\rangle}{E_I(\boldsymbol{Q}) - E_t}\left|X_{\tau',\boldsymbol{q}'}\right\rangle + \sum_{\boldsymbol{q}} \frac{\left\langle X_{\tau,\boldsymbol{q}}\middle|\hat{H}_T\middle|X_{\boldsymbol{Q},\tau',\tau}^{(0)}\right\rangle}{E_I(\boldsymbol{Q}) - E_b}\left|X_{\tau,\boldsymbol{q}}\right\rangle. \quad (2)$$

Here, $\left|X_{\tau',\boldsymbol{q}'}\right\rangle$ $\left(\left|X_{\tau,\boldsymbol{q}}\right\rangle\right)$ represents the *intralayer* exciton in the top (bottom) monolayer with energy E_t (E_b) and center-of-mass wavevector $\boldsymbol{q}'(\boldsymbol{q})$ defined in the individual monolayer. The second term on the right-hand side corresponds to the interlayer hopping of the hole from the $\tau\boldsymbol{K}$ valley in the bottom layer to the $\tau'\boldsymbol{K}'$ valley in the top layer to form the intralayer exciton. The third term similarly corresponds to the interlayer hopping of the electron from the $\tau'\boldsymbol{K}'$ valley of the top layer to the $\tau\boldsymbol{K}$ valley of the bottom layer to form the intralayer exciton. The interlayer hopping processes are shown in Figs. 5-3A & B.

The optical coupling of the interlayer exciton is of primary interest here, as this determines its impact potential for end use optoelectronic applications and provides the means to probe the unique physics found in this new system. At the light cones $\boldsymbol{Q} = \tau\boldsymbol{\kappa} - \tau'\boldsymbol{\kappa}'$, the transition matrix elements for the optical dipole of the interlayer exciton in the presence of the interlayer hopping perturbation are given by

$$\boldsymbol{\mathcal{D}}_{\tau',\tau,\boldsymbol{Q}} = \left\langle 0\middle|\widehat{\mathbf{D}}\middle|X^{(0)}_{\boldsymbol{Q},\tau',\tau}\right\rangle + \frac{\left\langle X_{\tau',\boldsymbol{q}'=\mathbf{0}}\middle|\widehat{H}_T\middle|X^{(0)}_{\boldsymbol{Q},\tau',\tau}\right\rangle}{E_I(\boldsymbol{Q}) - E_t}\langle 0|\widehat{\mathbf{D}}|X_{\tau',\boldsymbol{q}'=\mathbf{0}}\rangle + \frac{\left\langle X_{\tau,\boldsymbol{q}=\mathbf{0}}\middle|\widehat{H}_T\middle|X^{(0)}_{\boldsymbol{Q},\tau',\tau}\right\rangle}{E_I(\boldsymbol{Q}) - E_b}\langle 0|\widehat{\mathbf{D}}|X_{\tau,\boldsymbol{q}=\mathbf{0}}\rangle, \quad (3)$$

where $\widehat{\mathbf{D}}$ is the electric dipole operator and $|0\rangle$ is the vacuum state. The first term on the right represents the direct recombination of $|e_{\boldsymbol{k}',\tau'}\rangle$ and $|h_{\boldsymbol{k},\tau}\rangle$ as these basis functions for electron and hole respectively in the two layers can have finite overlap. The second and third terms represent the optical coupling mediated by the interlayer hopping to the bright intralayer exciton states in the top and bottom monolayers.

5.4 Optical selection rules of interlayer excitons

The intralayer exciton transition dipoles in the top and bottom monolayers are dictated by the valley optical selection rules $\langle 0|\widehat{D}|X_{\tau',\boldsymbol{q}'=0}\rangle = D\mathbf{e}_{\tau'}$, and $\langle 0|\widehat{D}|X_{\tau,\boldsymbol{q}=0}\rangle = D\mathbf{e}_{\tau}$, where $\mathbf{e}_{\pm} \equiv \frac{\boldsymbol{x} \pm i\boldsymbol{y}}{\sqrt{2}}$ represents the circular polarization vector of the emitted photon, and D is the interband transition dipole for the intralayer exciton. Using the two-center approximation[102,103], the three terms in Eq. (3) are respectively,

$$\left\langle 0\middle|\widehat{D}\middle|X^{(\mathbf{0})}_{\tau',\tau,\boldsymbol{Q}}\right\rangle \propto \sum_{\boldsymbol{\kappa},\boldsymbol{\kappa}'} \delta_{\mathbf{Q},\tau\boldsymbol{\kappa}-\tau'\boldsymbol{\kappa}'}\, D_0^{2\tau}(\tau\boldsymbol{\kappa})\, e^{-i\tau\boldsymbol{\kappa}\cdot\mathbf{r}},$$

$$\left\langle X_{\tau',\boldsymbol{q}'=0}\middle|\widehat{H}_T\middle|X^{(0)}_{\boldsymbol{Q},\tau',\tau}\right\rangle \approx \sum_{\boldsymbol{\kappa},\boldsymbol{\kappa}'} \delta_{\mathbf{Q},\tau\boldsymbol{\kappa}-\tau'\boldsymbol{\kappa}'}\, t^{2\tau}_{2\tau'}(\tau\boldsymbol{\kappa})e^{-i\tau\boldsymbol{\kappa}\cdot\mathbf{r}},$$

$$\left\langle X_{\tau,\boldsymbol{q}=0}\middle|\widehat{H}_T\middle|X^{(0)}_{\boldsymbol{Q},\tau',\tau}\right\rangle \approx \sum_{\boldsymbol{\kappa},\boldsymbol{\kappa}'} \delta_{\mathbf{Q},\tau\boldsymbol{\kappa}-\tau'\boldsymbol{\kappa}'}\, t^{0}_{0}(\tau\boldsymbol{\kappa})e^{-i\tau\boldsymbol{\kappa}\cdot\mathbf{r}},$$

where $t^m_{m'}$ ($D^m_{m'}$) are the Fourier components of hopping integral (transition dipole) between a W and a Mo d-orbitals with magnetic quantum numbers *m* and *m'*, respectively. $t^m_{m'}$ and $D^m_{m'}$ decay fast with the increase of $|\tau\boldsymbol{\kappa}|$, thus in practice only the main light cones ($\pm\boldsymbol{Q}_0$, $\pm\hat{C}_3\boldsymbol{Q}_0$, and $\pm\hat{C}_3^2\boldsymbol{Q}_0$) need to be considered, as the optical dipole strength becomes very weak in the Umklapp light cones ($\boldsymbol{Q}_{n>0}$) where $|\tau\boldsymbol{\kappa}|$ is large. The transition dipole for the interlayer exciton can be expressed as,

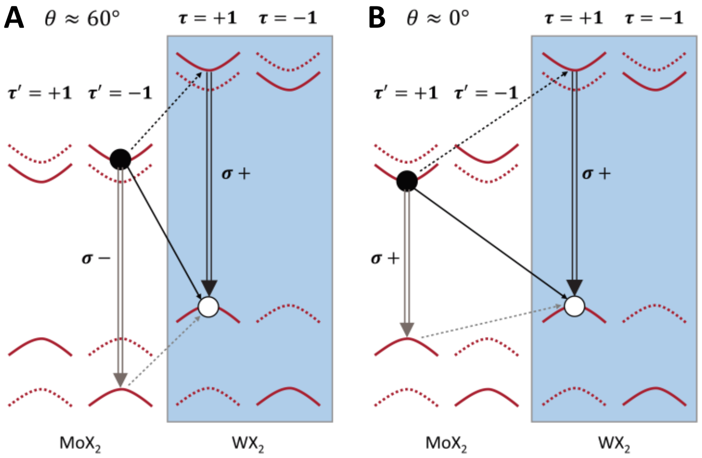

Figure 5-3 | Light coupling mediated by interlayer hopping. Interlayer hopping of the hole (gray dashed lines) and the electron (black dashed lines) couples the interlayer exciton to the interlayer excitons in MoX$_2$ and WX$_2$, respectively, for heterobilayers with twisting angle near **(A)** $\theta \sim 60°$ and **(B)** $\theta \sim 0°$.

$$\boldsymbol{\mathcal{D}}_{\tau',\tau,\boldsymbol{Q}} = e^{-i\tau\boldsymbol{\kappa}\cdot\mathbf{r}} \sum_{\boldsymbol{\kappa},\boldsymbol{\kappa}'} \delta_{\mathbf{Q},\tau\boldsymbol{\kappa}-\tau'\boldsymbol{\kappa}'} \left(D^{2\tau}_{0}(\tau\boldsymbol{\kappa})(\alpha\mathbf{e}_{\tau'} + \beta\mathbf{e}_{\tau}) + D\,\frac{t^{2\tau}_{2\tau'}(\tau\boldsymbol{\kappa})\mathbf{e}_{\tau'}}{E_I(\boldsymbol{Q}) - E_t} + D\,\frac{t^{0}_{0}(\tau\boldsymbol{\kappa})\mathbf{e}_{\tau}}{E_I(\boldsymbol{Q}) - E_b} \right),$$

where α and β are the weighted coefficients of the direct interlayer exciton emission polarization[104].

The essential result is now that $|X_{\boldsymbol{Q},\tau',\tau}\rangle$ may interconvert with photon with general form of elliptical polarization, without the assistance of phonon or impurity scattering at the finite velocity light cones $\boldsymbol{Q}$. Considering the underlying $\hat{C}_3$ rotational symmetry of the interlayer exciton states, the elliptical polarization at $\boldsymbol{Q}_0$, $\hat{C}_3\boldsymbol{Q}_0$, and $\hat{C}_3^2\boldsymbol{Q}_0$ are also $\hat{C}_3$ rotations of each other. Therefore, without mutual quantum coherence, the sum of emission from these three light cones combines to produce light with a finite degree of circular polarization but no linear polarization. The light cones $-\boldsymbol{Q}_0$, $-\hat{C}_3\boldsymbol{Q}_0$, and $-\hat{C}_3^2\boldsymbol{Q}_0$ are the time reversal counterparts of the above three where the excitons have the opposite valley configuration, and the elliptical polarization also has the opposite helicity.

Chapter 6: Observation of bright interlayer excitons

6.1 Overview

The majority of this chapter comes from my first publication, “Observation of Long-Lived Interlayer Excitons in Monolayer $MoSe_2$-WSe_2 Heterostructures”, which was first published by Nature Communications in 2014 (doi:10.1038/ncomms7242). While the following largely comes from the text of that work, I am happy to include some interesting follow-up data, in-line supplemental materials, and more detailed explanations that I am able to provide from my further and the removal of word count restrictions.

Observation of Long-Lived Interlayer Excitons in Monolayer $MoSe_2$-WSe_2 Heterostructures

Abstract: Van der Waals bound heterostructures constructed with two-dimensional materials, such as graphene, boron nitride, and transition metal dichalcogenides, have sparked wide interest in device physics and technologies at the two-dimensional limit. One highly coveted heterostructure is that of differing monolayer transition metal dichalcogenides with type II band alignment, with bound electrons and holes localized in individual monolayers, i.e. interlayer excitons. Here, we report the observation of interlayer excitons in monolayer $MoSe_2$-WSe_2 heterostructures by photoluminescence and photoluminescence excitation spectroscopy. We find that their energy and luminescence intensity are highly tunable by an applied vertical gate voltage. Moreover, we measure an interlayer exciton lifetime of approximately 1.8 ns, an order of magnitude longer than intralayer excitons in monolayers. Our work demonstrates optical pumping of interlayer electric polarization, which may provoke further exploration of interlayer exciton condensation, as well as new applications in two-dimensional lasers, light emitting diodes, and photovoltaic devices.

6.2 Introduction

The recently developed ability to vertically assemble different two-dimensional (2D) materials heralds a new realm of device physics based on van der Waals heterostructures[31]. The most successful example to date is the vertical integration of graphene on boron nitride. Such novel heterostructures not only dramatically enhance graphene’s electronic properties[26], but also give rise to super-lattice structures demonstrating exotic physical phenomena[28-30]. A fascinating counterpart to gapless graphene is a class of monolayer direct bandgap semiconductors, namely transition metal dichalcogenides (TMDs)[5,14,15]. Due to the large binding energy in these 2D semiconductors, excitons dominate the optical response, exhibiting strong light-matter interactions which are electrically tunable[51,52]. The discovery of excitonic valley physics[23,25,48,49,105] and strongly coupled spin and pseudospin physics[106,107] in 2D TMDs opens up new possibilities for device concepts not possible in other material systems.

Monolayer TMDs have the chemical formula MX_2 where the M is tungsten (W) or molybdenum (Mo), and the X is sulfur (S) or selenium (Se). Although these TMDs share the same crystalline structure, their physical properties, such as bandgap, exciton resonance, and spin-orbit coupling strength, can vary significantly. Therefore, an intriguing possibility is to stack different TMD monolayers on top of one another to form 2D heterostructures (HS). First principle calculations show that heterojunctions formed between monolayer tungsten and molybdenum dichalcogenides have type II band alignment[81,85,86]. Recently, this has been confirmed by X-ray photoelectron spectroscopy and scanning tunneling spectroscopy[98]. Since the Coulomb binding energy in 2D TMDs is much stronger than in conventional semiconductors, it is possible to realize interlayer excitonic states in van der Waals bound hetero-bilayers, i.e. bound electrons and holes that are localized in different layers. Such interlayer excitons have been intensely pursued in bilayer graphene for possible exciton condensation[108], but direct optical observation demonstrating the existence of such excitons is challenging due to the lack of a sizable bandgap in graphene. Monolayer TMDs with bandgaps in the visible range provide the opportunity to optically pump interlayer excitons, which can be directly observed through photoluminescence (PL) measurements.

In this report, we present direct observation of interlayer excitons in vertically stacked monolayer $MoSe_2$-WSe_2 HS. We show that interlayer exciton PL is enhanced under optical excitation resonant with the intralayer excitons in isolated monolayers, consistent with the interlayer charge transfer resulting from the underlying type II band structure. We demonstrate the tuning of the interlayer exciton energy by applying a vertical gate voltage, which is consistent with the permanent out-of-plane electric dipole nature of interlayer excitons. Moreover, we find a blue shift in PL energy at increasing excitation power, a hallmark of repulsive dipole-dipole interactions between spatially indirect excitons. Finally, time-resolved PL measurements yield a lifetime of 1.8 ns, which is at least an order of magnitude longer than that of intralayer excitons. Our work shows that monolayer semiconducting HS are a promising platform for exploring new optoelectronic phenomena.

6.3 $MoSe_2$-WSe_2 heterobilayer fabrication

Heterostructures are prepared by wet polymer transfer method using mechanically exfoliated monolayers of WSe_2 and $MoSe_2$. Monolayers of $MoSe_2$ are mechanically exfoliated onto 300 nm SiO_2 on heavily doped Si wafers and monolayers of WSe_2 onto a layer of poly-methyl(methacrylate) (PMMA) atop poly-vinyl alcohol (PVA) on Si. Both monolayers are identified with an optical microscope and confirmed by their photoluminescence spectra. The PVA is dissolved in H_2O and the PMMA layer is then placed on a transfer loop or thin layer of polydimethylsiloxane (PDMS). The top monolayer is then placed in contact with the bottom monolayer with the aid of an optical microscope and micromanipulators. The substrate is then heated to cause the PMMA layer to release from the transfer media. The PMMA is subsequently dissolved in acetone for ~30 min and then rinsed with IPA.

Since there is no effort made to match the crystal lattices of the two monolayers, the obtained heterostructures are considered incommensurate. An idealized depiction of the vertical $MoSe_2$-WSe_2 heterostructure is shown in Fig. 6-1A. We have fabricated six devices which all show similar results as those reported below (see Appendix Fig. A-1). The data presented here are from two independent $MoSe_2$-WSe_2 heterostructures, labelled Device 1 and Device 2. Figure 6-1B shows an optical micrograph of Device 1, which has large areas of individual monolayers, as well as vertically stacked heterostructure. This device architecture allows for the comparison of the excitonic spectrum of individual monolayers with that of the heterostructure region,

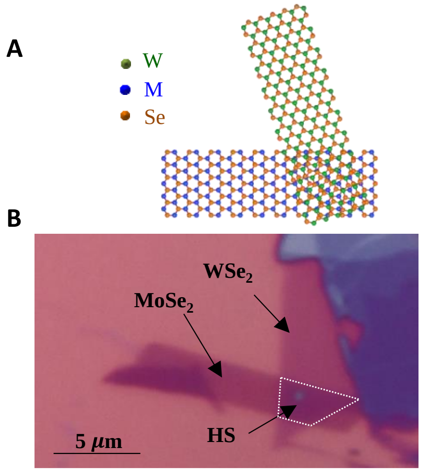

Figure 6-1 | $MoSe_2$-WSe_2 heterostructure. **(A)** Cartoon depiction of a $MoSe_2$-WSe_2 heterostructure (HS). **(B)** Microscope image of a $MoSe_2$-WSe_2 HS (Device 1) with white dashed line outlining the HS region.

allowing for a controlled identification of spectral changes resulting from interlayer coupling.

The rotational alignment of the constituent monolayers of Device 1 was determined after fabrication by analyzing the polarization of second harmonic generation (SHG) in the $MoSe_2$ and WSe_2. The monolayer TMDs are non-centrosymmetric and exhibit strong SHG along their armchair axes[109-112]. The second harmonic light is generated by exposing the samples to linearly polarized ultrafast laser pulses from a Coherent OPA (~0.85 eV). To determine the crystal axes, we analyze only the SHG that is co-polarized with the laser, which is rotated around 2π. The resulting six-fold SHG intensity patterns for the monolayers of $MoSe_2$ and WSe_2 are shown in Fig. 6-2. The lobes correspond to the armchair axes of the crystals. Comparing the orientation of the two patterns, we determine the relative rotation between the crystal axes to be ~3° for Device 1 (see Appendix Figure A-1 for the twist angles of other samples).

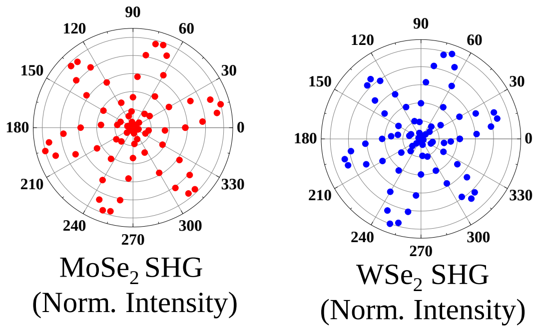

$MoSe_2$ SHG (Norm. Intensity)

WSe_2 SHG (Norm. Intensity)

Figure 6-2 | Second harmonic generation from $MoSe_2$ and WSe_2 monolayers. The normalized intensity of SHG co-polarized with the laser, as a function of the laser polarization axis, for $MoSe_2$ and WSe_2 monolayer regions of Device 1. The two six-fold patterns indicate that the two monolayer crystals are rotated from one another by ~3°.

6.4 PL characterization of the $MoSe_2$-WSe_2 heterobilayer

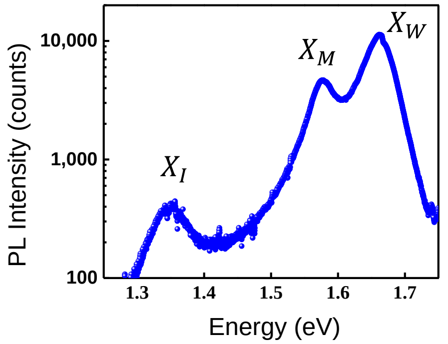

Figure 6-3 | Room temperature PL from the $MoSe_2$-WSe_2 heterostructure. Room temperature photoluminescence of the HS under 20 µW laser excitation at 2.33 eV. The excitons from monolayers of WSe_2 and $MoSe_2$ are labelled by X_W and X_M, respectively. The lowest energy peak comes from the spatially indirect, interlayer exciton, X_I.

We first characterized the photoluminescence from the $MoSe_2$-WSe_2 heterostructure sample. For steady state PL measurements, we use either 532 nm DPSS or 632 nm HeNe continuous wave (cw) laser light (beam diameter of ~1 µm) to excite the sample in a home built microscope (reflection geometry). The emitted PL is spectrally filtered through a 0.5 m monochromator (Andor Shamrock) and detected on a Si charge-coupled device (Andor Newton). Inspection of the room temperature PL from the heterostructure region, outlined by the dashed white line in Fig. 6-1B, reveals three clear spectral features (Fig. 6-3). The emission at ~1.65 eV and ~1.57 eV corresponds to the excitonic states from monolayer WSe_2 and $MoSe_2$[49,52], X_W and X_M, respectively. We attribute the anomalous reduced energy spectral feature at 1.35 eV to a spatially indirect exciton, the Coulomb bound state formed between the electron in $MoSe_2$ and hole in the WSe_2, i.e. the interlayer exciton (X_I). This state apparently has binding energy greater than room temperature and is the focus of this report.

Two-dimensional mapping of the PL from the sample shows that the three different regions of the sample exhibit different spectral responses. Spatial PL mapping is performed by raster-scanning the objective lens and excitation spot across the sample using a Mad City Labs Nano-T555 nanopositioning system. Fig. 6-4 shows the 2D maps generated by spectrally integrating the PL from the three peaks shown in Fig. 6-3 (X_W, X_{Mo}, and X_I) at each spatial position. The dashed white line outlines the heterostructure region (see Fig. 6-1B). Note that due to the spectral overlap of X_W and X_{Mo}, and the high relative intensity of X_W, it is not possible to entirely isolate the two features. However, it is clear from the spatial maps that the regions with high PL intensity of X_W (Fig. 6-4A) and X_{Mo} (Fig. 6-4C) correspond to monolayer WSe_2 and monolayer $MoSe_2$, respectively. Furthermore, the intensity of both of these peaks are suppressed on the heterostructure region. The 2D map generated by spectrally integrating the PL from X_I (Fig. 6-4B) shows that it is both uniform and isolated entirely to the HS region. The spatial map of the peak

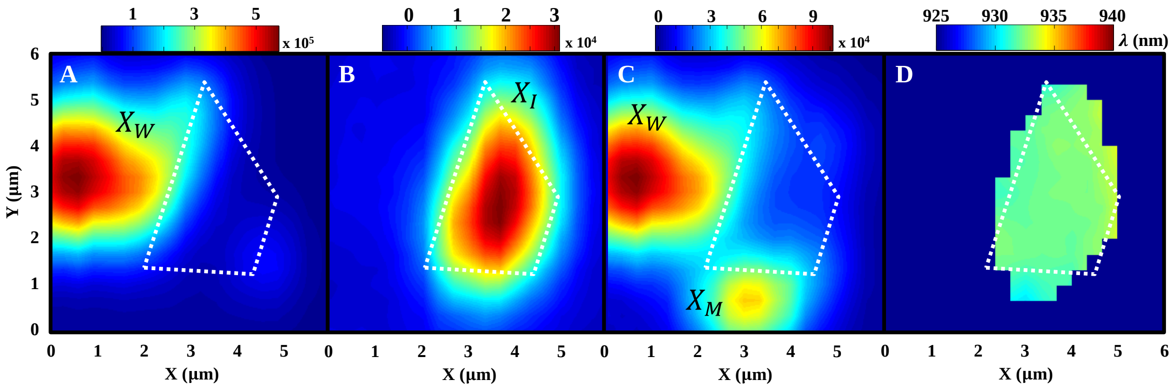

Figure 6-4 | Spatial maps of spectrally integrated PL from Device 1.
Spatial maps of the spectrally integrated photoluminescence intensity at room temperature from **(A)** intralayer excitons in monolayer WSe_2 (X_W), **(B)** interlayer excitons in the $MoSe_2$-WSe_2 heterostructure (X_I), **(C)** and intralayer excitons in monolayer $MoSe_2$ (X_M). **(D)** Spatial dependence of the center of the X_I peak in the photoluminescence, as extracted by fitting to single Gaussian peak (spatial positions with spectra at the background threshold appear solid blue). Dashed white line corresponds to the $MoSe_2$-WSe_2 heterostructure region shown in Fig. 6-1B.

position of the X_I PL is shown in Figure 6-4D, showing that the entire heterostructure has uniform spectral position of X_I. The uniform spatial and spectral isolation of X_I to the heterostructure region strongly suggests that its origin is not from defect related excitons. Another interesting note is that these maps were taken over a year after the sample was fabricated, and after more than a dozen thermal cycles to 30K or below.

Low temperature PL characterization of the HS was performed with cw laser excitation (1.88 eV) at 20K, in a temperature controlled Janis cold finger Helium flow cryostat (sample in vacuum). PL from individual monolayer WSe_2 (top), $MoSe_2$ (middle), and the heterostructure area (bottom) are shown with the same scale in Figure 6-5. At low temperature, the intralayer neutral (X_M^0) and charged ($X_M^\pm$) excitons are resolved[49,52], where M labels either W or Mo. Comparison of the three spectra shows that both intralayer X_M^0 and $X_M^\pm$ exist in the heterostructure, with emission at the same energy as from isolated monolayers, demonstrating the preservation of intralayer excitons in the heterostructure region. PL from X_I becomes more pronounced and is comparable to the intralayer excitons at low temperature. We note that the X_I energy position has considerable variation across the pool of heterostructure samples we have studied (Appendix Figure A-1), which we attribute to differences in the interlayer separation, possibly due to imperfect transfer and different twisting angle between monolayers.

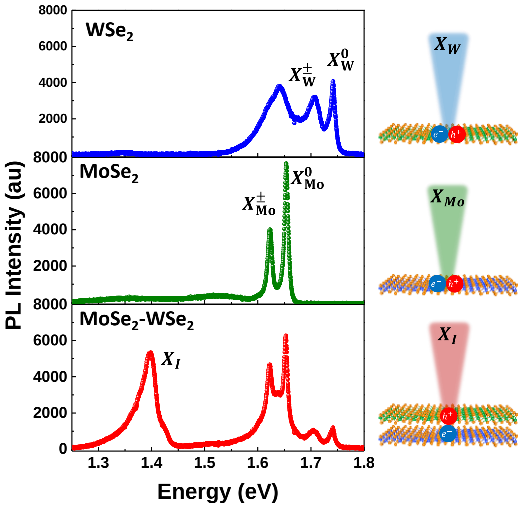

Figure 6-5 | Emergence of interlayer exciton in the low temperature PL. PL from isolated monolayer of WSe_2 (top), isolated monolayer of $MoSe_2$ (middle), and heterobilayer region (bottom) at ~20K. The emergence of the low energy PL at ~1.4eV is the hallmark of bright interlayer exciton.

6.5 PL excitation spectroscopy results

We further perform photoluminescence excitation spectroscopy (PLE) to investigate the correlation between X_I and intralayer excitons. A narrow bandwidth (<50 kHz) frequency tunable continuous wave Ti:Sapphire laser (M^2 SolsTiS) is tuned across the energy resonances of intralayer excitons (from 1.6 eV to 1.75 eV) while monitoring the X_I PL response. The laser is filtered from the PL signal using an 815 nm long pass optical filter (Semrock) before entering the spectrometer.

Fig. 6-6 shows an intensity plot of X_I emission as a function of excitation energy, from Device 2. The integrated PL intensity is plotted over the PL spectrum in Fig. 6-6B, clearly illustrating the enhancement of X_I emission when the excitation energy is resonant with intralayer exciton states.

Now we discuss the origin of X_I. Since X_I has never been observed in our exfoliated monolayer and bilayer samples, if its origin were related to defects, they must be introduced by the fabrication process. This would result in sample dependent X_I properties with non-uniform spatial dependence. However, our data shows that key physical properties of X_I, such as the resonance energy and intensity, are spatially uniform and isolated to the HS region (see Fig. 6-4). In addition, X_I has not been observed in WSe_2-WSe_2 homostructures constructed from exfoliated or PVD monolayers (Appendix Fig. A-2). All these facts suggest that X_I is not a defect related exciton.

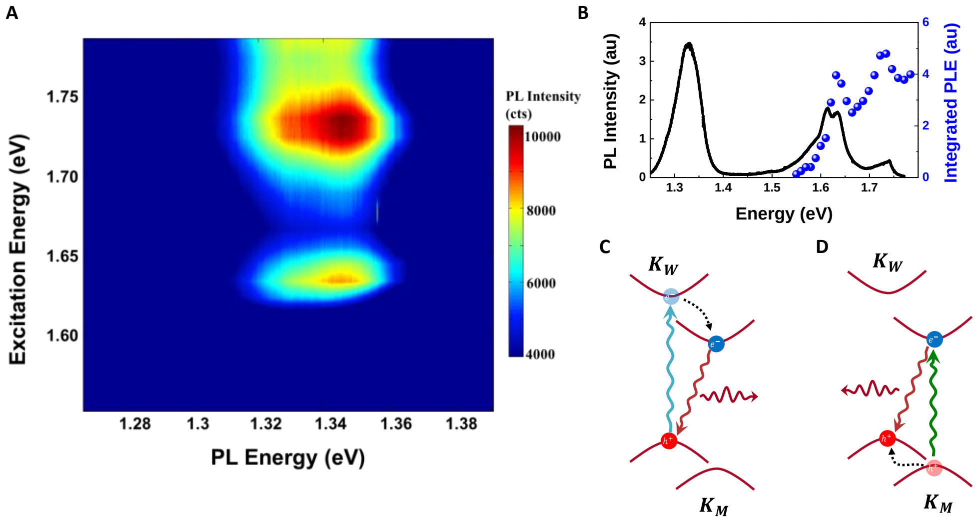

Figure 6-6 | PL excitation spectroscopy of the interlayer exciton at 20K. (A) PLE intensity plot of the heterostructure region with an excitation power of 30 μW and 5 second CCD integration time. **(B)** Spectrally integrated PLE response (blue dots) overlaid on PL (black line) with 100 μW excitation at 1.88 eV. Type II semiconductor band alignment diagram for the 2D $MoSe_2$-WSe_2 heterojunction, showing the charge transfer process for generation of interlayer exciton by resonant excitation with the intralayer exciton in (**C**) monolayer WSe_2 and **(D)** monolayer $MoSe_2$.

Instead, the experimental results support the observation of interlayer exciton. Due to the type II band alignment of the $MoSe_2$-WSe_2 HS[81,85,86], as shown in Figs. 6-6C&D, photo-excited electrons and holes will relax (dashed lines) to the conduction band edge of $MoSe_2$ and the valence band edge of WSe_2, respectively. The Coulomb attraction between electrons in the $MoSe_2$ and holes in the WSe_2 gives rise to interlayer exciton, X_I, analogous to spatially indirect excitons in coupled quantum wells. The interlayer coupling yields the lowest energy bright exciton in the heterostructure, which is consistent with the temperature dependence of X_I PL, i.e. it increases as temperature decreases (Appendix Fig. A-3).

From the intralayer and interlayer exciton spectral positions, we can infer the band offsets between the WSe_2 and $MoSe_2$ monolayers. The energy difference between X_W and X_I at room temperature is ~310 meV. Considering the smaller binding energy of interlayer than intralayer excitons (due to their spatial separation), this sets a lower bound on the conduction band offset. The energy difference between X_M and X_I then provides a lower bound on the valence band offset of 230 meV. This value is consistent with the 228 meV found in MoS_2-WSe_2 heterostructures by µXPS and STS measurements[98]. This experimental evidence strongly corroborates X_I as interlayer exciton. The observation of bright interlayer excitons in monolayer semiconducting heterostructures is of central importance, and the remainder of this paper will focus on their physical properties resulting from their spatially indirect nature and the underlying type II band alignment.

6.6 Electrical control of interlayer exciton

The spatial separation of the electron and hole implies an out-of-plane electric dipole for X_I, which couples to externally applied electric fields. To test this hypothesis, we apply an electric field to the $MoSe_2$-WSe_2 heterostructure and measure the PL. Figure 6-7A shows the contact geometry of Device 2, where an indium contact has been fabricated on the WSe_2 layer, which is vertically stacked on top of the $MoSe_2$. The heterostructure is on SiO_2, which provides insulation from the heavily doped silicon backgate. Electrostatic doping is performed by grounding the indium contact and applying a voltage to the backgate (V_g). Figure 6-7B shows the interlayer exciton PL as V_g is varied from +100 to –100 V. Over this range, the peak center blue shifts by ~45 meV. Subsequent measurements on an inverted analogue of Device 2, where the stacking order of $MoSe_2$ and WSe_2 is reversed (see Fig. 6-7C), shows the peak center red shift by ~60 meV as V_g is varied from +70 to -70 V (Fig 6-7D).

The gate dependence of X_I is consistent with that expected for the interlayer exciton, which maintains a dipole pointing from $MoSe_2$ to WSe_2 (Fig. 6-7A). At negative V_g, the electric field reduces the relative band-offset between the $MoSe_2$ and WSe_2 in Device 2, increasing the energy separation between the $MoSe_2$ conduction band and the WSe_2 valence band. The interaction of the field and the anti-aligned dipole of the interlayer exciton thus results in the observed blue shift in

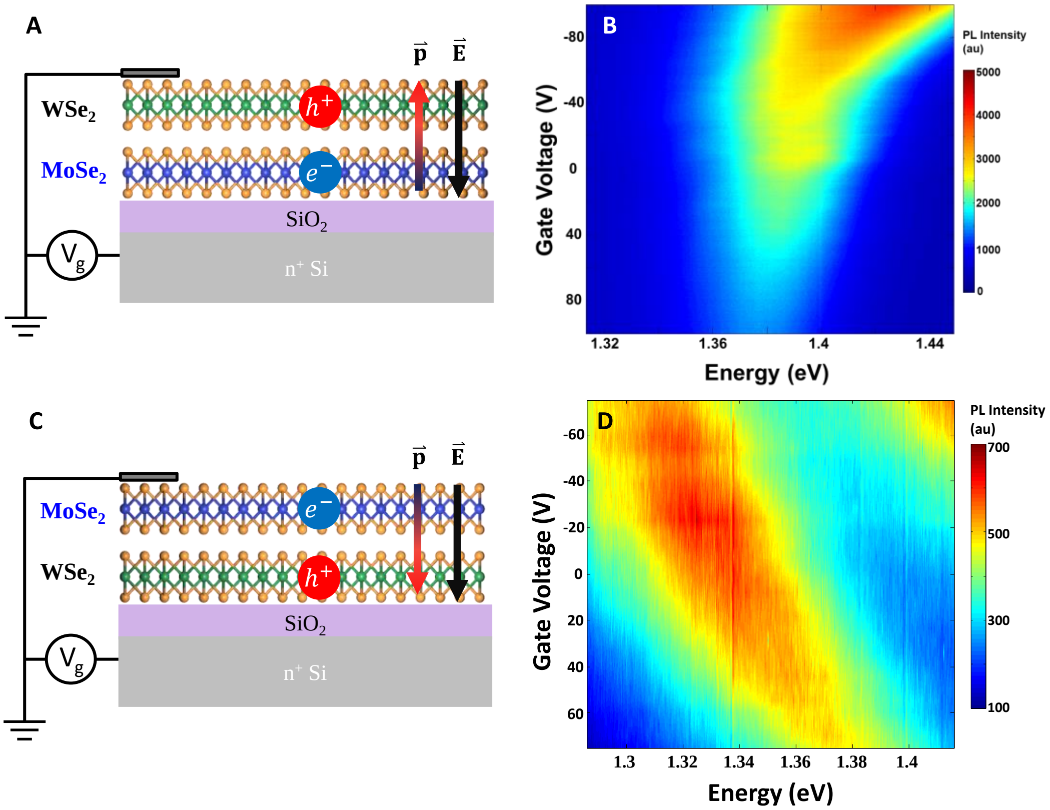

Figure 6-7 | Electrical control of the interlayer exciton energy. **(A)** Electrically contacted heterostructure with WSe_2 on top of $MoSe_2$. The interlayer exciton has a permanent electric dipole pointing up. **(B)** Interlayer exciton PL as a function of applied gate voltage. **(C)** Electrically contacted heterostructure with $MoSe_2$ on top of WSe_2. The interlayer exciton has a permanent electric dipole pointing down. **(D)** Interlayer exciton PL as a function of applied gate voltage.

the energy of PL from X_I shown in Fig 6-7B. Conversely, when $MoSe_2$ is located on top of WSe_2, as shown in Fig. 6-7C, the field effect increases the relative band-offset at negative V_g, manifesting the observed red shift in X_I PL (Fig 6-7D). The electrical control of the energy of X_I confirms the direction of its permanent dipole. However, we expect linear behavior for the electric field dependent shift, i.e. Stark effect. The lack of linearity in Fig. 6-7A shows that in addition to electrical field effect, carrier doping may play a significant role in tuning X_I intensity. We expect devices with both top and bottom gates may further elucidate the observed phenomena.

6.7 Power dependence and lifetime of interlayer exciton

The interlayer exciton spectrum as a function of laser power, with excitation energy in resonance with $\mathrm{X_W^o}$, reveals several properties of the $\mathrm{X_I}$. Inspection of the normalized PL intensity (Fig. 6-8A) shows the evolution of a doublet in the interlayer exciton spectrum, highlighted by the red and green bi-Lorentzian fits. Both peaks of the doublet display a consistent blue shift with increased laser intensity, shown by the dashed arrows, which are included as a guide to the eye. The spectrally integrated intensity of $\mathrm{X_I}$ also exhibits a strong saturation as a function of laser power, as shown in Figure 6-8B. The sublinear power response of $\mathrm{X_I}$ for excitation powers above 0.5 $\mathrm{W \cdot cm^{-2}}$ is distinctly different than that for the intralayer excitons in isolated monolayers, which display a saturation power threshold exceeding 80 μW.

The low power saturation of $\mathrm{X_I}$ PL suggests a much longer lifetime than that of intralayer excitons. In the heterostructure, the lifetime of the intralayer exciton is substantially reduced by the ultrafast interlayer charge hopping[94], which is evidenced by the strong quenching of intralayer exciton PL on the heterostructure (Fig. 6-4). Moreover, the lifetime of the interlayer exciton is

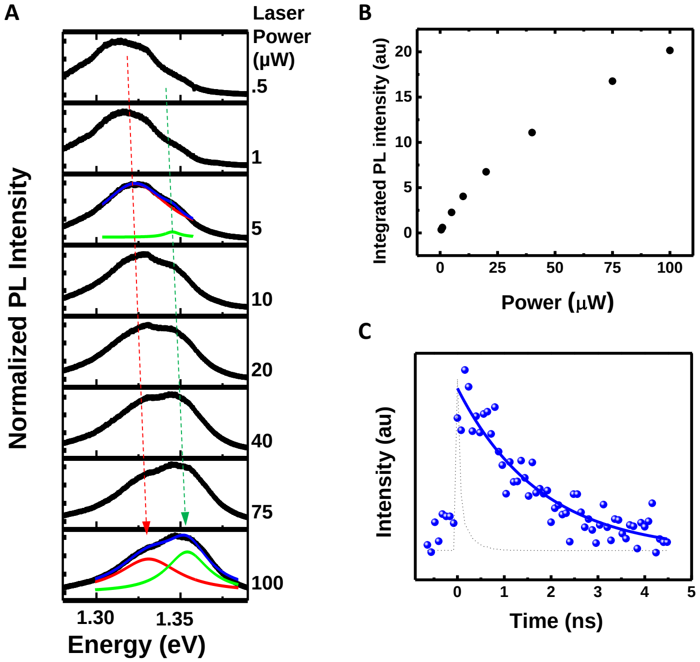

Figure 6-8 | Power dependent PL and long lifetime of interlayer exciton. (A) Power dependence of the interlayer exciton with a bi-Lorentzian fit to the 5 and 100 μW plots, normalized for power and integration time. **(B)** Spectrally integrated intensity of the interlayer exciton emission as a function of excitation power shows strong saturation. **(C)** Time resolved PL of the interlayer exciton reveals a population lifetime of about ~1.8 ns. The dashed curve is the instrument response to the excitation laser pulse.

long because it is the lowest energy configuration and its spatially indirect nature leads to a reduced optical dipole moment. This long lifetime is confirmed by time resolved PL, as shown in Figure 6-8C. For interlayer exciton PL lifetime measurements, we excite the sample with a <200 fs pulsed Ti:Sapphire laser (Coherent - MIRA). Interlayer PL is spectrally filtered through a 0.5 m monochromator (Princeton - Acton 2500), and detected with a fast time correlated single photon counting system composed of a fast (<30 ps FWHM) single photon avalanche detector (Micro Photon Devices - PDM series) and a picosecond event timer (PicoQuant - PicoHarp 300). A fit to a single exponential decay yields an interlayer exciton lifetime of 1.8 ± 0.3 ns. This time scale is much longer than the intralayer exciton lifetime, which is on the order of tens of ps[113-116]. By modeling the saturation behavior using a simplified three level diagram, the calculated saturation intensity for the interlayer exciton is about 180 times smaller than intralayer, consistent with our observation of low saturation intensity of X_I.

6.8 Discussion

We attribute the observed doublet feature in Fig. 6-8A to the spin-splitting of monolayer $MoSe_2$ conduction band. This assignment is mainly based on the fact that the extracted energy difference between the doublet is approximately 25 meV, which agrees well with $MoSe_2$ conduction band splitting predicted by first principle calculations[117]. This explanation is also supported by the evolution of the relative strength of the two peaks with increasing excitation power, as shown in Fig. 6-8A. At low power, the lowest energy configuration of interlayer excitons, with the electron in the lower spin-split band of $MoSe_{2,}$ is populated first. Due to phase space filling effects, the interlayer exciton configuration with the electron in the higher energy spin-split band starts to be filled at higher laser power. Consequently, the higher energy peak of the doublet becomes more prominent at higher excitation powers.

The observed blue shift of X_I as the excitation power increases, indicated by the dashed arrows in Fig. 6-8A, is a signature of the repulsive interaction between the dipole-aligned interlayer excitons. This is a hallmark of spatially indirect excitons in GaAs coupled quantum wells, which have been intensely studied for exciton Bose-Einsten condensation phenomena[118]. The observation of spatially indirect interlayer excitons in a type II semiconducting 2D heterostructure provides an intriguing platform to explore exciton BEC, where the observed extended lifetimes and repulsive interactions are two key ingredient towards the realization of this exotic state of matter. Moreover, the extraordinarily high binding energy for excitons in this truly 2D system may provide for degenerate exciton gases at elevated temperatures compared to other material systems[30]. The long-lived interlayer exciton may also lead to new optoelectronic applications, such as photovoltaics[36,39,119,120] and 2D heterostructure nano-lasers.

6.9 Acknowledgements

Xiaodong Xu and I designed the experiments to support the claim of interlayer exciton. Phillip Klement, an exchange student from Justus-Liebig-University in Giessen, Germany, and I fabricated the devices, assisted by Jason S. Ross. Device contact fabrication was performed at the Washington Nanofabrication Facility and NSF-funded Nanotech User Facility. John R. Schaibley, Aaron M. Jones, Jason S. Ross, Sanfeng Wu, and Grant Aivazian helped me implement the photoluminescence apparatus and to perform the measurements. Kyle Seyler provided assistance with second harmonic generation measurements. Genevieve Clark grew the monolayer WSe_2 samples used for the homobilayer preparation using physical vapor deposition techniques. The bulk $MoSe_2$ and WSe_2 crystals used to fabricate the samples used in this study were provided by Nirmal J. Ghimire, Jiaqiang Yan, and David G. Mandrus from Oak Ridge National Laboratory and the University of Tennessee. Finally, the manuscript was written by myself, John R. Schaibley, Xiaodong Xu, and our theorist, Wang Yao, from the University of Hong Kong.

Chapter 7: Valley Interlayer Excitons

7.1 Overview

Following the demonstration of long lifetime for the interlayer excitons in the $MoSe_2$-WSe_2 heterobilayer, a natural question arose regarding the polarization properties of the interlayer exciton. It was becoming clear to the community that the unique optical selection rules and valley polarized excitons in monolayer TMDs were limited by picosecond timescale depolarization arising from the exchange interactions between the electron and hole. In the heterobilayer, the reduced oscillator strength of the interlayer exciton, apparently coming from the spatial separation of the electron and hole, should lead to longer valley polarization lifetimes by suppressing the main depolarization mechanism in the monolayers. This chapter focuses on our work to address this question, providing the first demonstration of valley-polarized interlayer excitons, with long lifetime and electronic control, which was reported in "Valley-Polarized Exciton Dynamics in a 2D Semiconductor Heterostructure", first published in Science in 2016 (doi: 10.1126/science.aac7820). This chapter largely follows that manuscript, but I have added some additional comments and data and placed some of the supplementary materials and methods sections within the text, where I think it will help the interested reader to understand some of the finer details.

Valley-Polarized Exciton Dynamics in a 2D Semiconductor Heterostructure

Abstract: Heterostructures comprising different monolayer semiconductors provide an attractive setting for fundamental science and device technologies, such as in the emerging field of valleytronics. Here, we realize valley-specific interlayer excitons in monolayer WSe_2-$MoSe_2$ vertical heterostructures. We create interlayer exciton spin-valley polarization by circularly polarized optical pumping and determine a valley lifetime of 40 nanoseconds. This long-lived polarization enables the visualization of the expansion of a valley-polarized exciton cloud over several microns. The spatial pattern of the polarization evolves into a ring with increasing exciton density, a manifestation of valley exciton exchange interactions. Our work introduces van der Waals heterostructures as a promising platform to study valley exciton physics.

7.2 Introduction

Van der Waals heterostructures of two-dimensional (2D) materials provide an exciting platform for engineering artificial material systems with unique properties[31]. A beautiful example is the demonstration of the Hofstadter butterfly physics in moiré superlattice structures composed of graphene and hexagonal boron nitride[28-30]. As the library of 2D crystals is explored further, the range of possible new phenomena in condensed matter physics becomes ever more diverse. For example, heterostructures of 2D semiconductors (namely, transition metal dichalcogenide monolayers, TMDs) have been assembled with type-II band alignment[81,85,86,98], where electrons and holes energetically favor different layers. These heterobilayers form atomically thin p-n junctions which can be used for photon-energy harvesting[36,39,93,94,120-122], and host interlayer excitons (X_I) with the Coulomb-bound electron and hole located in different monolayers[93,119,122,123], as illustrated in the top of Fig. 7-1A. This species of exciton has a lifetime far exceeding those in monolayer MX_2, and the vertical separation of holes and electrons entails a permanent out-of-plane electric dipole moment, providing an optical means to pump interlayer electric polarization, and facilitating electrical control of interlayer excitons[123]. In the following, we observe long valley lifetime and valley drift-diffusion of X_I in $MoSe_2$-WSe_2 heterostructures with small twist angles.

The interlayer excitons in TMD heterobilayers are similar to spatially indirect excitons in III-V quantum wells[124-128]. In both systems, the electron-hole wave function overlap is reduced in the out-of-plane direction, suppressing the magnitude of exciton oscillator strength and the electron-hole exchange interaction. This leads to greatly enhanced population and spin lifetimes for spatially indirect excitons compared to their direct exciton counterparts. The following study seeks to clarify if and how these effects impact the properties of the interlayer exciton in the TMD heterobilayer.

Distinct from quantum well systems, TMD heterobilayers possess several unique features. First, the monolayers' band edges are at doubly degenerate corners of the hexagonal Brillouin zone, so X_I has an internal degree of freedom specified by the combination of electron and hole valley indices[23]. Second, the twist angle between the crystal axes of constituent monolayers leads to a displacement of the conduction and valence band edges in momentum space, making the X_I dark, i.e. momentum indirect, at its minimum energy and bright only at finite center-of-mass velocities. The location of the X_I light cones depends on the twist angle between the monolayers, allowing for control over the optoelectronic properties[89,90,110], such as the dipole strength and interlayer exciton lifetime[91]. Third, the constituent MX_2 monolayers exhibit unique valley-contrasting physical properties, such as spin-valley locking, optical selection rules[25,48,105], and Berry curvature[23]. The inheritance of valley physics in twisted MX_2 heterostructures is predicted to give rise to unique optical and transport properties of X_I[91], allowing the possibility of excitonic optoelectronic circuits with valley functionalities and providing a platform for investigating excitonic superfluidity and condensation[129].

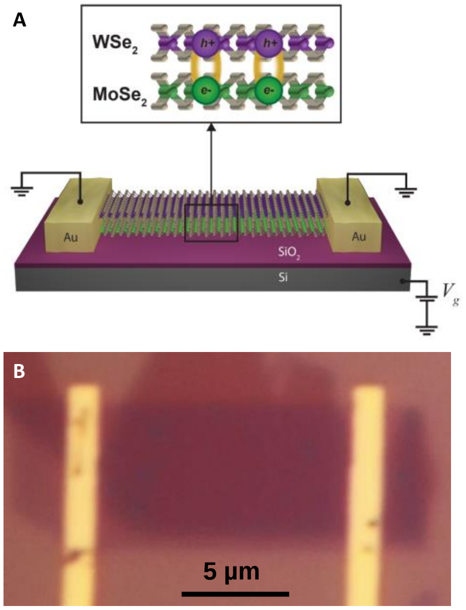

Figure 7-1 | $MoSe_2$-WSe_2 heterobilayer device.
(A) Side view of $MoSe_2$-WSe_2 heterostructure device. Boxed region depicts the interlayer exciton, with holes (h^+) and electrons (e^-) located in WSe_2 and $MoSe_2$, respectively. **(B)** Optical image of device with WSe_2 on top of $MoSe_2$.

7.3 Sample details

The samples in this study are TMD heterobilayers, i.e. van der Waals bound pairs of exfoliated monolayers of WSe_2 and $MoSe_2$. The optical brightness of the interlayer exciton in this system depends sensitively on the relative alignment of the two constituent monolayers, since this defines the relative alignment of the band edges located in the different monolayers TMDs. Theory shows that for twist angle near zero or 60°, there exist light cones at small kinematic momenta where the X_I can directly interconvert with photons[91]. In such heterobilayers, the X_I can radiatively recombine only at these light cones, e.g. hot excitons, or after scattering by exciton-phonon or exciton-exciton interactions[91]. To study the optical properties we therefore must focus on the heterobilayer with small twist angle.

The monolayer samples were exfoliated from bulk crystal onto 285 nm SiO2 on n+ doped Si. Linear-polarization-resolved second-harmonic generation (SHG) was used to identify the crystal axes of the WSe2 and MoSe2 monolayers[109,111,112]. The intensity of the SHG co-linearly

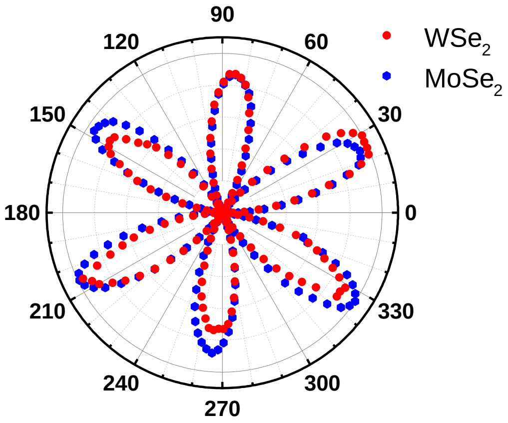

Figure 7-2 | Twist angle of heterobilayer from SHG measurements.
The relative orientation of the monolayers of $MoSe_2$ and WSe_2 are determined by SHG after the fabrication of the sample. The six-fold rotational patterns have a relative rotation of ~2°.

polarized with the excitation laser (Coherent OPA 9800, center ~0.85 eV) was analyzed as a function of crystal orientation. The orientation of the armchair edges was determined by fitting the angular dependence of the intensity to the equation, $I = I_0 \cos^2 3\theta$, where I_0 is the maximum SHG intensity and θ is the angle between the laser polarization and the armchair edge. We note that this technique is not sensitive to the SHG phase and thus the specific direction along the armchair edge is unknown.

Using a polycarbonate-based dry-transfer technique[78], we stacked exfoliated monolayers of MoSe2 and WSe2, aligning the armchair edges of the two layers to within 2 degrees. This technique yields heterobilayers with twisting angle near 0 or 60 degrees. Electron beam lithography was used to pattern contact areas and electron beam evaporation was used to deposit V/Au metal (6/60 nm) contacts. The device in the main text (Fig. 7-1B) had regions with isolated WSe2 and MoSe2 monolayers, allowing us to confirm the accuracy of stacking process after device fabrication, as shown in Fig. 7-2.

7.4 Polarization resolved PL from the $MoSe_2$-WSe_2 heterobilayer

Photoluminescence (PL) measurements were performed in reflection geometry using a home-built micro-PL setup at 30 K. The PL was collected and analyzed by a grating spectrometer (Andor SR-500i) and charge-coupled device (Andor Newton CCD). For continuous-wave (cw) excitation, we used a power-stabilized and frequency-tunable narrow band (< 50 kHz) Ti:Sapphire laser (M^2 Solstis).

The high quality and small twist angle of our heterobilayer samples allows us to observe the X_I PL, even at room temperature (Fig. 7-3A). We further note that the degree of quenching of the intralayer excitons in this sample is near unity at low temperatures, as shown in Fig. 7-3B. All data in the main text are taken at a temperature of 30 K from the device shown in the optical microscope image in Fig. 7-1B, with WSe_2 stacked on $MoSe_2$, and the excitation laser energy in resonance with the A exciton of WSe_2 (1.72 eV).

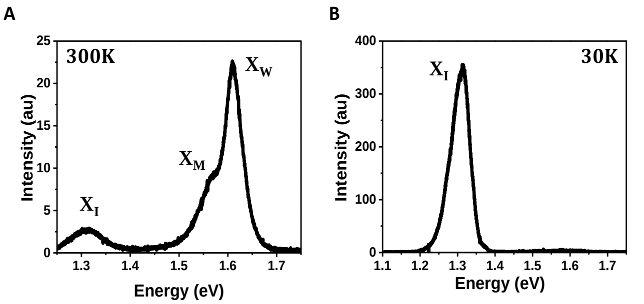

Figure 7-3 | $MoSe_2$-WSe_2 heterobilayer PL. Broad spectrum photoluminescence (PL) from the $MoSe_2$-WSe_2 heterostructure presented in the main text at a temperature of (A) 300 K and (B) 30 K. The intralayer exciton in the monolayer of $MoSe_2$ (X_M) and WSe_2 (X_W), as well as the interlayer exciton (X_I) are labeled where there is sufficient PL to resolve them. The strong quenching of the intralayer excitons at 30 K evidences the good interlayer coupling of the constituent monolayers.

We first perform polarization-resolved PL at zero gate voltage ($V_g = 0$ V). We apply circularly polarized cw laser excitation and separately detect the right circular (σ^+) and left circular (σ^-) PL. Figure 7-4 shows the σ^+ (black) and σ^- (red) components of the X_I PL under circularly polarized excitation. These results show that X_I emission is strongly co-polarized with the incident light. Denoting the degree of polarization by $\rho = \frac{I_+ - I_-}{I_+ + I_-}$, where $I_\pm$ is the intensity of the $\sigma^\pm$ PL components, we observe $|\rho_{max}| > 0.3$. Similar results are obtained from several other samples (Appendix B Fig. B-1). We also perform measurements in the linear basis, which do not show appreciable polarization (Appendix B Fig. B-2).

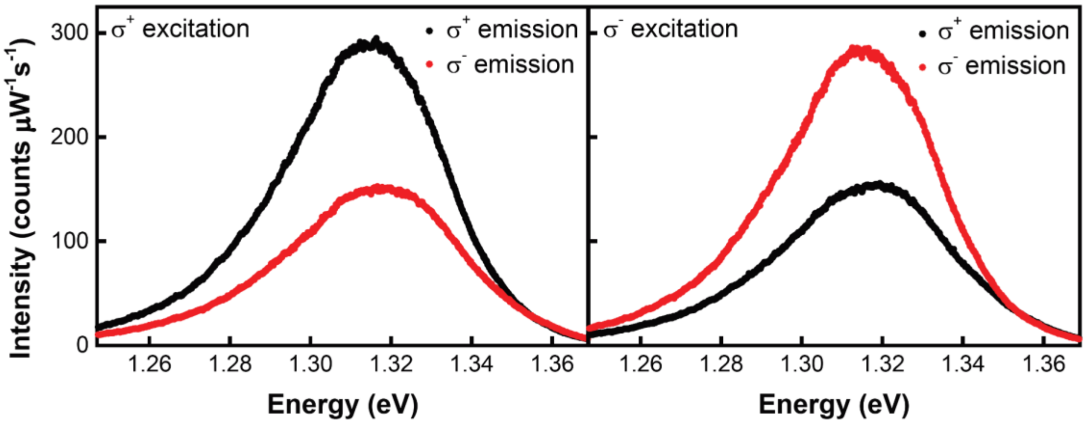

Figure 7-4 | Valley-polarized PL from interlayer exciton. Under excitation with circularly polarized light, the right (σ^+) and left (σ^-) circularly polarized emission from interlayer excitons in the $MoSe_2$-WSe_2 heterobilayer is resolved. The polarization of the PL follows the excitation laser, demonstrating valley-polarized interlayer exciton.

The observation of circularly polarized PL demonstrates that the X_I can retain memory of the excitation light helicity, which is a consequence of the valley optical selection rules in 2D heterobilayers[91]. In the following, we discuss the generation of valley polarization in heterobilayers near AA-like stacking (twist angle near 0°, illustrated in Fig. 7-5A), but similar conclusions can be drawn for heterobilayers near AB-like stacking (twist angle near 60°, see Appendix B.2)[130]. The valley configuration of X_I is specified by the valley indices of its electron and hole. With the spin-valley locking in monolayer TMDs, a universal assignment of the valley index is applicable in the twisted heterobilayers, and herein we denote the valley with electron spin up (down) as $+K$ ($-K$) in both layers.

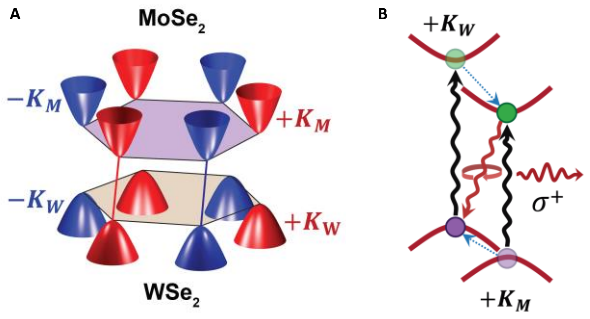

Figure 7-5 | Optical generation of valley interlayer excitons. (A) Illustration of the 2D BZ of the MoSe-WSe$_2$ heterobilayer with small twist angle. The conduction (valence) band edges appear at $\pm K_M$ ($\pm K_W$). **(B)** Illustration of the process for optical generating valley-polarized interlayer excitons. First, σ^+ circularly polarized light (black wavy lines) excites intralayer excitons in the $+K_M$ and $+K_W$ valleys. Fast interlayer charge transfer (blue dotted lines) then forms the interlayer exciton in the $+K$ valley. The optical selection rules result in σ^+PL from the interlayer exciton.

The generation of valley-polarized X_I is described by the following process. First, σ^+ excitation creates valley-polarized intralayer excitons in the $+K_W$ valley in WSe$_2$ and $+K_M$ valley in MoSe$_2$. Next, charge carriers relax to the heterobilayer band edges through interlayer charge transfer on sub-picosecond time scales[93,94] to form X_I. Because of the large momentum difference, interlayer hopping between $+K_W$ and $-K_M$ valleys is strongly suppressed. Conversely, the $+K_W$ and $+K_M$ valleys have small momentum mismatch and the spin-conserving interlayer hopping between these valleys becomes the dominant relaxation channel. Therefore, the σ^+ excitation leads to valley-polarized X_I, as illustrated in Fig. 7-5B. The situation for σ^- excitation can be obtained by time reversal. The radiative recombination of the valley-polarized X_I is then facilitated by the interlayer coupling, which allows emission of photons that are co-polarized with the excitation source[91].

7.5 Electrical control of valley polarization and interlayer exciton lifetime

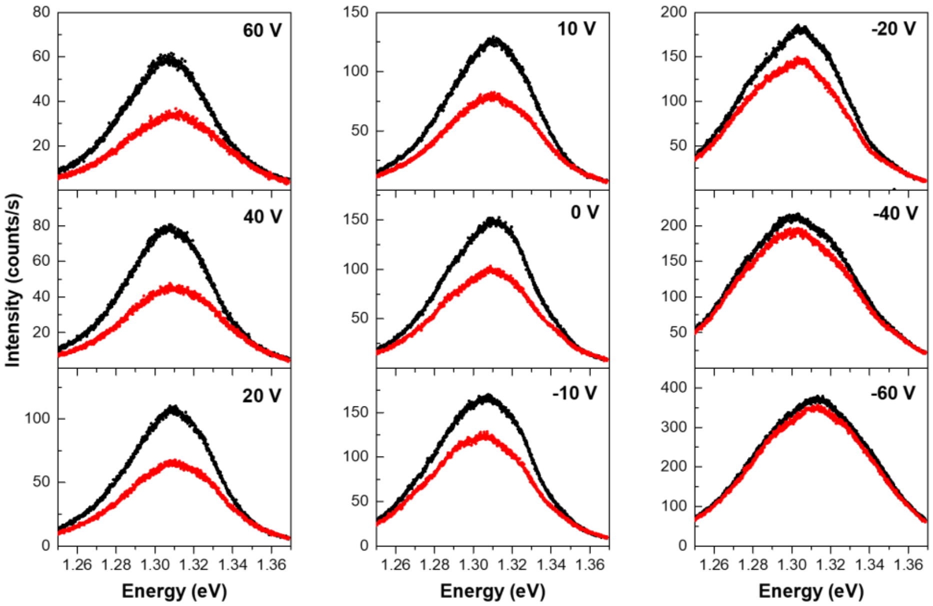

Figure 7-6 | Gate control of interlayer exciton valley polarization. Circular polarization-resolved interlayer exciton PL spectra at various gate voltages. The pulsed laser excitation is σ^+ polarized (1.72 eV) and the co-polarized (black) and cross-polarized (red) components of the interlayer exciton PL are detected separately.

We find that the degree of X_I valley polarization can be electrically controlled by the gate. Figure 7-6 shows polarization-resolved PL spectra at selected V_g under σ^+ excitation with ~50 ps laser pulses (5 MHz repetition rate). There is a strong gate dependence of the valley polarization, which is greatest at +60 V ($\rho\sim0.3$) and highly suppressed at –60 V ($\rho\sim0$). We also see a large difference in the PL yield at different gate voltages, as can be seen by the variation in the y-axis limits for the different plots in Fig. 7-6. The microscopic mechanism for the observed behaviors is not yet understood, but the fact that the energy of the interlayer exciton does not vary much indicates that the effects are not likely due to the presence of an electric field, since this would induce an energy change. Instead, this is likely a doping effect, which implies that the valley exciton polarization is dictated by the hole spin-valley degree of freedom ($V_g > 0$ corresponds to electron doping and $V_g < 0$ corresponds to electron doping). This is consistent with the fact that the spin-valley locking in the valence band is much stronger than in the conduction band. Therefore, we can conclude that the electrical injection, which is not spin or valley polarized, of holes can destroy the optically generated valley polarization. Further work is required to fully understand these details.

To determine the valley polarization lifetime, we performed time-resolved PL. Pulsed excitation was performed with a supercontinuum laser with ~2 nm bandwidth (FWHM) and single-mode Gaussian beam profile, focused to ~700 nm beam diameter. For these measurements, the peak wavelength of the interlayer exciton PL was spectrally filtered by the grating spectrometer and measured using a silicon avalanche photodiode (PicoQuant, τ-SPAD) connected to a picosecond event timer (PicoQuant PicoHarp 300) for time-correlated single photon counting. The instrument response of ~400 ps is significantly shorter than the observed interlayer exciton decay times. To accommodate long lifetimes, we used the pulsed excitation source at 100 kHz repetition rate.

In Fig. 7-7, we show the decay of co-polarized (black) and cross-polarized (red) interlayer exciton PL, as well as the degree of polarization (blue), at the same V_g values as in Fig. 7-6. The valley polarization lifetime increases with V_g, reaching 39 ± 2 ns at +60 V, as determined by fitting with a single exponential decay. Long valley lifetimes were also measured in heterostructures with the opposite stacking order (i.e. $MoSe_2$ on WSe_2, see Appendix B, Fig. B-3).

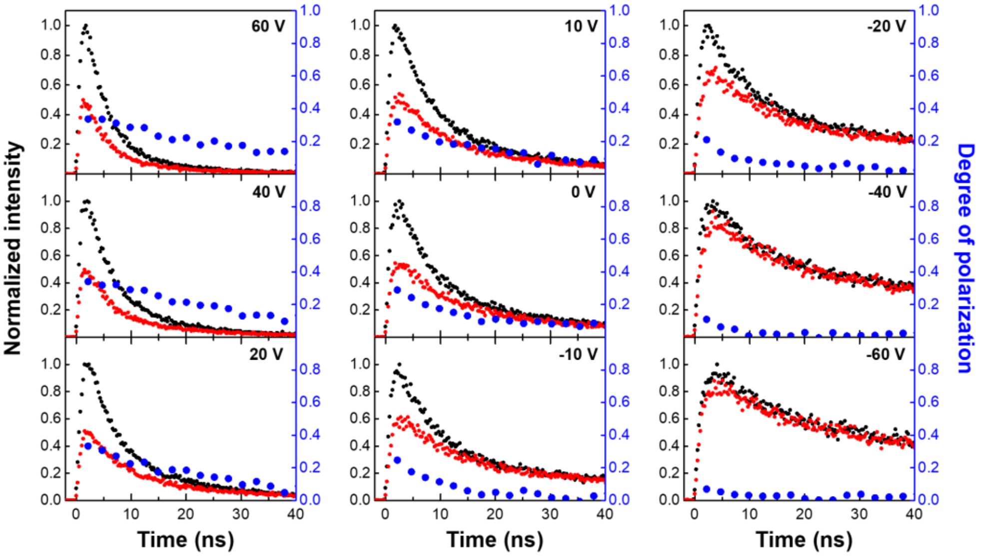

Figure 7-7 | Gate control of interlayer valley polarization dynamics. Time and circular polarization-resolved interlayer exciton PL spectra at various gate voltages under pulsed excitation (100 kHz). The pulsed laser excitation is σ^+ polarized (1.72 eV) and the co-polarized (black) and cross-polarized (red) components of the interlayer exciton PL are detected separately. The degree of valley polarization is shown in blue (right y-axes). The valley lifetime is longest for large positive gate voltage and decreases with lower gate voltages.

These measurements imply a strong suppression of intervalley scattering for the X_I and a valley lifetime several orders of magnitude longer than that of intralayer excitons in monolayers, where valley depolarization occurs on picosecond timescales[116,131,132]. Our measurement also shows that the initial PL polarization of X_I is about 40% at +60 V. The imperfect initial valley polarization of X_I is likely due to valley depolarization of intralayer excitons in the constituent monolayers, which mediate the X_I formation. We note that because the X_I is dark at the minimum of the energy dispersion[91], due to the finite twisting angle and slight lattice mismatch between the two layers, it effectively provides a reservoir from which the X_I are scattered into the light cones and luminesce. The momentum-indirect nature of X_I is supported by temperature-dependent measurements, which show enhanced lifetime at low temperature (see Appendix B, Fig. B-4). This complicated exciton-light coupling is likely responsible for the subtle but intriguing features in Fig. 7-7, such as the increase of PL lifetime accompanying the decrease of valley polarization lifetime. However, future studies are required to gain a clear understanding of the microscopic mechanism for the observed gate-dependent PL dynamics of the X_I.

7.6 Drift and diffusion of interlayer excitons

The long valley lifetime of the X_I allows visualization of their lateral drift and diffusion through spatially resolved PL measurements. Here, we magnified the PL and set the spectrometer grating to its zero-order mode to image the emission on the charge coupled device (CCD). A dichroic beamsplitter and an interference longpass filter ensured that only interlayer exciton PL was collected. Figure 7-8 displays a sequence of spatial maps of the spatial distribution of the co-polarized (σ^+, top) and cross-polarized (σ^-, middle) X_I PL, and valley polarization (ρ, bottom) under pulsed excitation (40 MHz repetition rate) at V_g = 60 V, for selected average excitation powers (P_0 = 1 μW). The salient feature is that the spatial pattern of ρ shows the evolution of a ring with diameter that increases with excitation intensity.

The observed ring pattern in the valley polarization stands in contrast to the spatial distribution of the emission. The spatial maps of the polarization-resolved PL intensity at 20 μW show that both $\sigma^+$and σ^- PL components display an approximately Gaussian profile centered at the excitation spot. For direct comparison of the different spatial profiles, Fig. 7-9 shows the σ^+ (black) and σ^- (red) components of the X_I PL, as well as the valley polarization (ρ) along linecuts

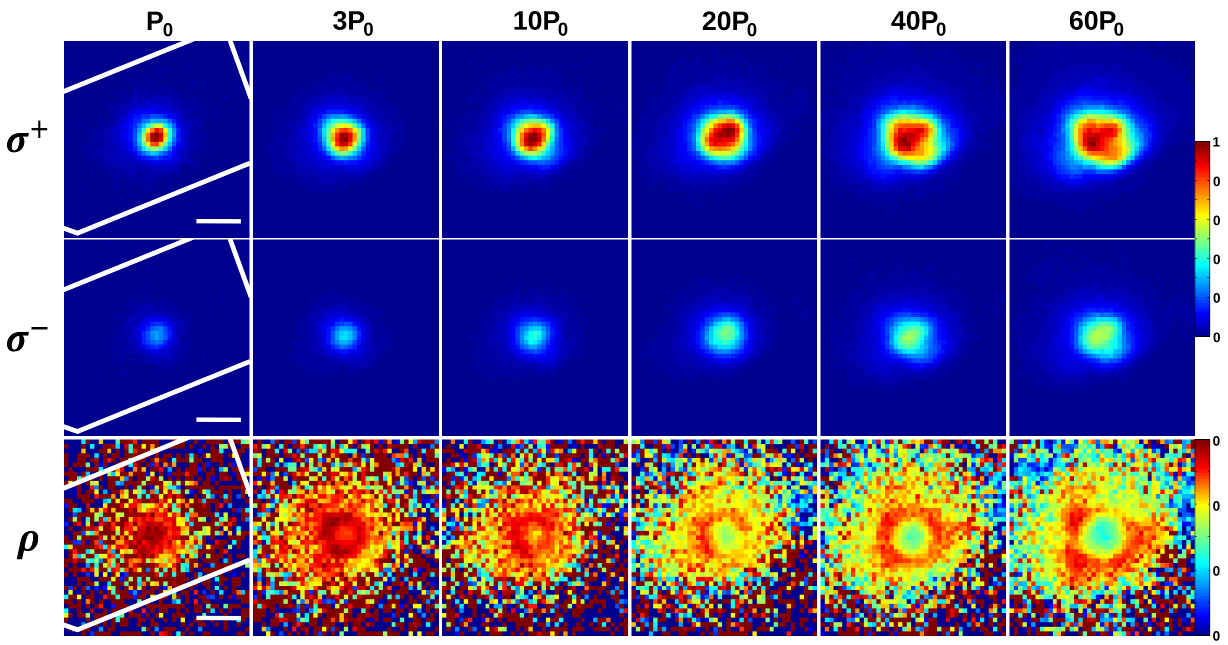

Figure 7-8 | Density dependent drift-diffusion of valley-polarized interlayer exciton gas. Spatial maps of valley polarization under σ + pulsed laser excitation at 1.72 eV with P0 = 1 μW. Scale bar is 2 μm. At each power, the spatial profile of co- and cross-polarized emission is shown (normalized to the peak co-polarized intensity) in the top and middle panels, respectively, and the degree of valley polarization is shown in the bottom. The spatial pattern of valley polarization displays the evolution of a ring with increasing diameter under higher excitation power. We note that the maps of the exciton population show noticeable distortion for P > $20P0$, which indicates the strong role of exciton-exciton interactions with increasing power.

(radially averaged) through the center of the laser beamspot (dashed gray line). The data shows increased drift-diffusion lengths for $+K$ and $-K$ valley excitons moving away from the laser spot (0.7 μm FWHM, dashed) at higher powers corresponding to higher exciton density. However, there is a striking difference between the inferred exciton density, which has approximately Gaussian shape, and the spatial distribution of valley polarization, which shows the formation of a ring. We attribute the formation of the ring to strong exciton-exciton interactions at high X_I densities, as described in the following section.

7.7 Valley dependent exchange interactions

One possible explanation for the observed polarization ring is density-dependent intervalley scattering. However, consideration of the valley polarization as a function of excitation intensity suggests otherwise. Figure 7-10 shows the power dependence of valley polarization from the spatially integrated intensity of σ^+ and σ^-, which decreases by ~25% over a 60-fold increase in excitation power, corresponding to at least an order of magnitude increase in the exciton density.

Yet, the radial dependence of ρ shows a decrease of nearly 40% from its peak, at the radius of the ring of polarization, to its minimum at the excitation center (e.g. 40P$_0$ or 60P$_0$ in Fig 7-9). This is a dramatic change in ρ considering that the exciton density drops by only a factor of two over this region (i.e., the corresponding PL intensity decreases by approximately 50%). The weak dependence of the integrated valley polarization on excitation intensity, contrasted with the strong variation of ρ in the ring feature, implies that density-dependent intervalley scattering is not the dominant mechanism in the ring formation.

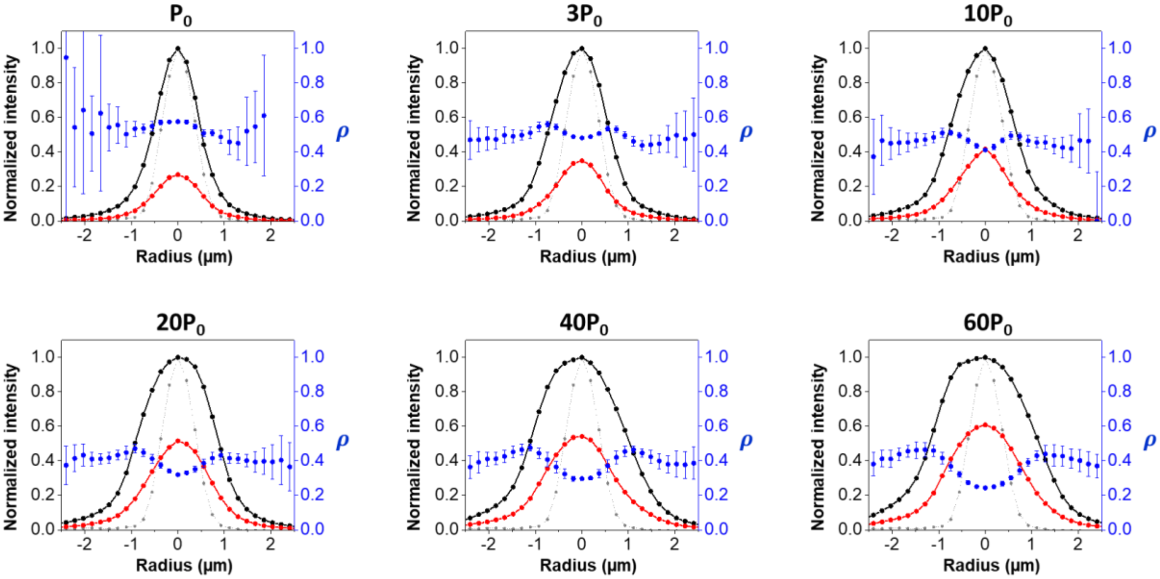

Figure 7-9 | Power dependent spatial distribution of valley exciton density and polarization. Radially averaged linecuts through the center of the laser spot (gray dashed line), showing the spatial distribution of intensity for co-polarized (σ^+, black) and cross-polarized (σ^-, red) polarized components of the interlayer exciton PL, and the valley polarization ρ (blue), under pulsed laser excitation at 1.72 eV. P$_0$ = 1 μW. At each power, the PL linecuts are normalized to the peak co-polarized intensity. While the spatial distribution of the PL shows approximately Gaussian shape for both polarizations, the spatial distribution of ρ displays the evolution of a ring with increasing diameter under higher excitation power.

The observed spatial patterns in the valley polarization can be understood as manifestations of valley-dependent many-body interactions in the dense interlayer exciton gas[130]. The spin-valley polarized X_I, which possess out-of-plane dipoles, interact through dipole-dipole and exchange interactions, both of which are repulsive. Due to the small interlayer separation of about 7 Å, we estimate that the exchange interaction is stronger than the dipole-dipole repulsion[130] (see Appendix B.3 for discussion). Because the exchange interactions are appreciable only between excitons of the same valley species[130], in a cloud of valley-polarized interlayer excitons, the majority valley excitons experience stronger mutually repulsive force (Fig. 7-11A), leading to more rapid expansion than the minority valley excitons (Fig. 7-11B). On the other hand, the density gradient of excitons will also give rise to diffusion, which is valley-independent and does not produce a ring pattern. Therefore, the relative strength of the diffusion and valley-dependent drift controls the pattern of the spatial polarization, such that if the interlayer exciton density is large enough that the valley-dependent repulsive interaction dominates the expansion of the exciton gas, higher valley polarization can appear away from the excitation center. Indeed, simulations predict that a pronounced ring in the polarization will appear at sufficiently high excitation intensity, just as witnessed in Fig. 7-9 (see Appendices B.5 & B.6 for details).

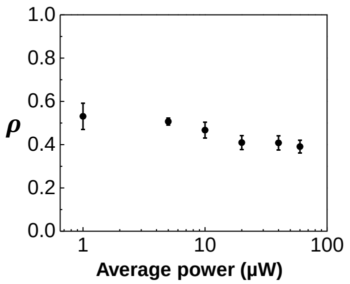

Figure 7-10 | Power dependence of the total valley polarization. The degree of valley polarization from the spatially integrated σ^+ and σ^- components of the interlayer exciton photoluminescence.

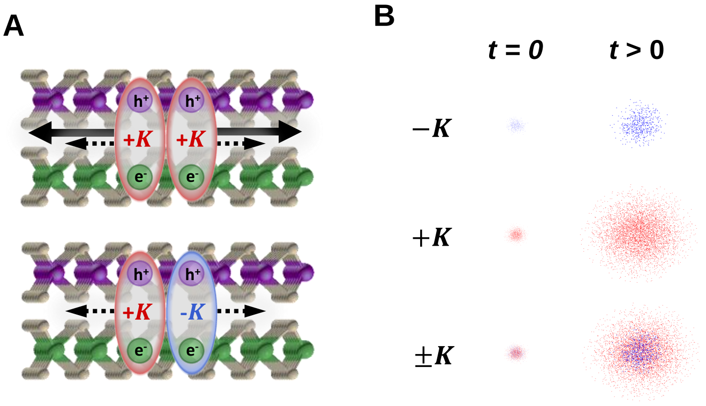

Figure 7-11 | Valley dependent exchange interactions and drift-diffusion. (A) Illustration of the valley-dependent repulsive interactions between interlayer excitons. Excitons in the same valley (top) experience repulsive forces due to the dipole-dipole repulsion (short dotted arros) as well as the exchange interaction (long solid arrows), whereas excitons in opposite valleys (bottom) only experience the dipole-dipole interaction. **(B)** Under short, intense σ^+ excitation, the spatial distribution of $+K$ (red) and $-K$ (blue) excitons is the same, but the population density of $+K$ is larger i.e. a valley polarized exciton gas is created (t=0, left). The majority $+K$ excitons experience higher repulsive forces and thus expand faster, and farther, than the minority $-K$ excitons, leading to the formation of a ring pattern in the spatial distribution of valley polarization.

7.8 Discussion

We note that a temperature difference between the majority and minority X_I could, in principle, cause them to expand at different speeds. However, under excitation by polarized laser pulse, the minority excitons are created at the excitation spot through intervalley relaxation. Since the relaxation of this internal degree of freedom does not change the kinetic energy of the exciton, the majority and minority X_I are expected to have the same initial temperature before the expansion of the exciton cloud. This precludes valley-dependent temperature as a driving force for the ring formation.

7.9 Acknowledgments

Xiaodong Xu and Wang Yao supervised the project. Sample fabrication was performed by Kyle Seyler and myself, assisted by Jason S. Ross. Kyle Seyler, Xiaodong Xu, and I performed the data analysis and interpretation. Theoretical support was provided by Hongyi Yu and Wang Yao, who also performed the simulations. Jiaqiang Yan and David Mandrus provided the bulk $MoSe_2$ and WSe_2. I wrote the paper with Kyle Seyler, Xiaodong Xu, Wang Yao, and Hongyi Yu.

Chapter 8: Interlayer excitons coupled to photonic crystal cavity

8.1 Overview

The advantageous properties of the interlayer exciton, such as long population and valley lifetime, motivated a study into the coupling of these states to the cavity of a photonic crystal (PhC). Previous studies in the Xu Laboratory demonstrated that the monolayer WSe_2 placed on top of the PhC showed characteristics of an ultra-low power threshold laser[133], and that the excitonic emission pattern could be affected by the PhC[134]. Naturally, these studies motivated the placement of the heterobilayer on the PhC. A common question in the community has been how the interlayer exciton can be an out-of-plane dipole yet emit light along the dipole (i.e. has in-plane optical dipole). The results from this study addresses this question, demonstrating that the interlayer exciton possesses significant in-plane optical dipole, which is in line with recent theoretical considerations of higher-order emission pathways[135]. At the time of this thesis, the following manuscript is about to be submitted for publication.

Interlayer Exciton Emission Enhanced by Photonic Crystal Cavity

Abstract: The advent of van der Waals heterostructures marks the emergence of a new class of synthetic materials with novel and unique properties, unattainable in their constituent materials. The two-dimensional architecture of these heterostructures makes them naturally suited for integration with a wide variety of planar photonic cavities for next-generation low-power optoelectronic devices and explorations of fundamental physical effects in these new systems. Here, we report the coupling of the interlayer exciton in a transition metal dichalcogenide heterobilayer with a gallium phosphide photonic crystal cavity. The exciton-cavity coupling is found to be in the weak regime, resulting in ~10-fold increase in the photoluminescence intensity for interlayer exciton in resonance with the cavity. The order of magnitude enhancement of the photoluminescence yield offsets the low oscillator strength of the interlayer exciton, adding a new tool for probing the underlying physics of this novel excitonic system.

8.2 Introduction

The recent advances in two-dimensional (2D) materials characterization and the fabrication of van der Waals (vdW) heterostructures present new opportunities for the quantum engineering of ultrathin synthetic materials with unique physical properties[31,32]. In parallel with the discovery of these new material systems, one promising research direction is to investigate how these materials behave when integrated with nanophotonic structures[33,136,137]. Heterobilayers formed from different monolayer transition metal dichalcogenides (TMDs) have attracted intense research efforts in recent years due to their atomically sharp type-II electronic interface[39,120], and the resulting formation of interlayer exciton[93,123] – the Coulomb bound state composed of electron and hole localized in different layers. The spatially indirect nature of the interlayer exciton imbues it with a number of advantageous properties for developing valley functional optical devices, but also results in a low oscillator strength, which has limited progress towards characterizing the interlayer exciton properties. Here, we show that the placement of the TMD heterobilayer on top of a gallium phosphide photonic crystal (PhC) cavity results in exciton-cavity coupling in the weak regime, with a significant enhancement of the PL from the interlayer exciton in resonance with the PhC cavity modes.

In the past several years, the TMD heterobilayer (Fig. 8-1A) has emerged as a promising vdW heterostructure with potential applications for valleytronic optoelectronic devices. This is because the lowest lying excitation is the interlayer exciton (IX), the Coulomb bound state with electron and hole from different layers (Fig. 8-1B). Resulting from the spatial separation of the constituent charges, the IX exhibits enhanced exciton population[123,138] and valley lifetimes[139-141], compared to its monolayer TMD counterparts. Moreover, the intrinsic electric dipole moment of the IX gives rise to a simple control over the exciton energy by externally applied electric field (via DC Stark effect)[123]. However, recent theoretical[91] and experimental[142] works have revealed small optical dipole moment for IX, with oscillator strength at least 2 orders of magnitude lower than that of a single monolayer TMD. This limitation has made studies of the IX properties challenging. However, the high sensitivity of 2D materials to their dielectric environment makes them especially suitable for coupling to planar nano-cavities, which presents an opportunity to overcome this shortcoming. Already, monolayer TMDs embedded in distributed Bragg reflector microcavities have demonstrated the formation of valley polaritons[143,144], and surface coupling with photonic crystal cavity has given rise to ultra-low threshold nanoscale lasers[133], cavity enhanced LED[145], and enhanced second harmonic generation[146]. Integrating the TMD heterobilayer with a micro-cavity is therefore a promising way to circumvent its low oscillator strength, which would facilitate optical studies of the IX properties.

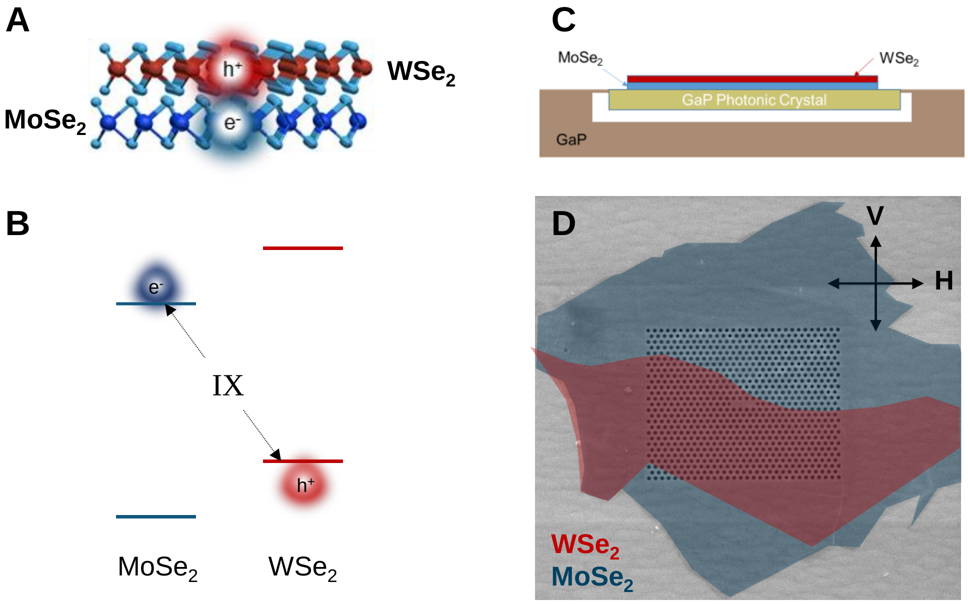

Figure 8-1 | MoSe$_2$-WSe$_2$ heterobilayer integrated with GaP photonic crystal. (A) Side-view illustration of the spatially separated electron and hole in the MoSe$_2$-WSe$_2$ heterobilayer. **(B)** Band alignment of the MoSe$_2$-WSe$_2$ heterobilayer with the interlayer exciton (IX) transition highlighted. **(C)** Side-view of the heterobilayer placed on top of the gallium phosphide photonic crystal (PhC). **(D)** Scanning electron micrograph of the MoSe$_2$-WSe$_2$ heterobilayer on PhC. The monolayer of WSe$_2$ is overlaid in red, while the monolayer MoSe$_2$ in blue, for clarity. The V and H axes are indicated in the inset.

8.3 Sample details

The sample in our study consists of a MoSe$_2$-WSe$_2$ heterobilayer placed on top of a gallium phosphide (GaP) three linear 3-hole defect (L3) photonic crystal cavity, as illustrated in Figure 8-1C. The photonic crystal and cavity were fabricated from a 125 nm thick GaP membrane grown via molecular beam epitaxy on 1 μm thick sacrificial Al$_{0.8}$Ga$_{0.2}$P layer on a GaP wafer. The patterns were first defined in ZEP520 resist by electron-beam lithography (JEOL JBX 6300, 100 keV) and then transferred to the GaP membrane by a chlorine-based reactive ion etch. Excess resist was removed with Microposit remover 1165 followed by oxygen plasma. The sacrificial layer was undercut with hydrofluoric acid to yield suspended membrane structures with high index contrast, followed by cleaning in dilute KOH to remove any by-products of the undercut.

The quality factor of the photonic crystal cavity was characterized by linear polarization resolved reflectivity measurements at 300K, prior to fabrication and transfer of the heterobilayer.

These measurements revealed bare cavity resonances at $\hbar\omega_1 = 1.369$ eV and $\hbar\omega_2 = 1.325$ eV with quality factors of $Q_1 = 1370 \pm 140$ and $Q_2 = 780 \pm 50$ (see Fig. C1 in Appendix C). This particular cavity was chosen because the higher energy resonance is well-matched to the IX PL energy in $MoSe_2$-WSe_2 heterobilayers.

The heterobilayer was assembled from monolayers of $MoSe_2$ and WSe_2 that were mechanically exfoliated from high quality bulk materials, using the top-down PC-based viscoelastic stamping technique[78]. The straight edges of the monolayer flakes of WSe_2 and $MoSe_2$ were carefully aligned during the fabrication, and the final transfer was directed onto the photonic crystal cavity. The PC transfer media was then dissolved in chloroform to yield the heterobilayer on top of the photonic crystal. A scanning electron micrograph of the completed device is shown in Figure 8-1D, with the different layers of the heterobilayer outlined and highlighted for clarity.

8.4 PL characterization of heterobilayer integrated with photonic crystal

The optical response of the TMD heterobilayer on photonic crystal was characterized using confocal PL spectroscopy in reflection geometry, normal to the plane of the heterobilayer, at a temperature of ~5 K with a 40x objective lens (0.6 NA). A diode-pumped solid-state continuous wave (cw) laser (λ = 532 nm) was used to excite the sample. Cryogenic measurements were performed with the sample attached to the cold head of a Montana Instruments Cryostation, in vacuum. The PL was dispersed by a 0.5 m monochromator equipped with a 600 line/mm groove density diffraction grating and a thermoelectrically cooled charge-coupled device (Andor Shamrock + Newton CCD) for time-integrated measurements. In all PL measurements, the excitation beam was spectrally filtered from the signal using a combination of dichroic beam splitters and long-pass filters.

The low energy PL spectra from the heterobilayer shows two broad peaks in the interlayer exciton spectrum, centered at approximately 1.33 eV and 1.38 eV (see Fig. 8-2), which spectrally overlap the photonic crystal cavity modes. Two narrow peaks appear in the PL spectrum ON the cavity (Fig. 8-2A, left), that are absent from the spectrum taken OFF the cavity (Fig. 8-2A, right). The energetic positions of the narrow peaks, 1.361 eV and 1.322 eV, closely match the energies of the bare photonic crystal cavity modes, measured at room temperature. Moreover, these PL

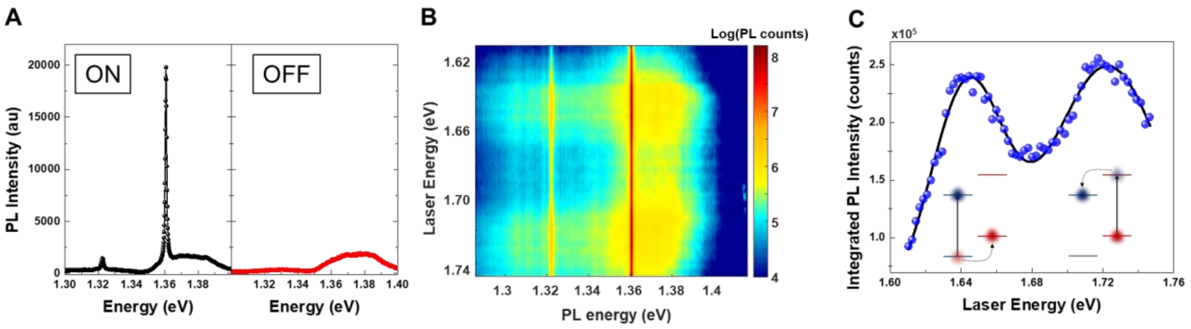

Figure 8-2 | Cavity coupling of the interlayer exciton. (A) Photoluminescence (PL) spectra from ON (left) and OFF (right) of the linear 3-hole defect cavity in the photonic crystal (PhC). The sharp peak present ON the cavity is spectrally degenerate with the cavity mode (see Figure S1). **(B)** Photoluminescence excitation (PLE) response from the $MoSe_2$-WSe_2 heterobilayer ON the PhC cavity. **(C)** Integrated PL intensity of the $MoSe_2$-WSe_2 heterobilayer at various excitation energies. The insets illustrate the formation process of interlayer exciton by photon absorption (solid vertical arrows) in monolayer $MoSe_2$ (left) and monolayer WSe_2 (right), followed by interlayer charge transfer (dashed arrows). This gives rise to the two peaks in the PLE response of the interlayer exciton (biGaussian fit, shown in solid black lines).

resonances have similar quality factors as the bare cavities (see Fig. C-2 in Appendix C), indicating low absorptive loss from the IX.

8.5 PLE of cavity-enhanced interlayer exciton

To confirm that the low energy PL is coming from the interlayer excitons, we performed photoluminescence excitation spectroscopy (PLE). For PLE measurements, the excitation source was a power stabilized frequency tunable cw laser (M^2 SolsTiS). For time-resolved measurements, the excitation source was spectrally filtered output (~3 nm FWHM) from a supercontinuum laser with ~6 ps pulse duration and 1 MHz repetition rate. The PL was spectrally filtered (~2 nm FWHM) using a slit assembly mounted at the side port output of the monochromator before being directed onto a single-photon detector (Excelitas SPCM) connected to a time-correlated counting system (PicoHarp 300), with an overall instrument response time of ~450 ps.

The excitation laser energy was tuned across the excitonic manifolds of the isolated TMD monolayers (1.61 to 1.75 eV) while collecting the low energy PL from ON the cavity. The PLE response, shown in Figure 8-2B, displays two broad resonances for the PL, both in and out of resonance with the cavity modes. Figure 8-2C presents the spectrally integrated PL as a function of laser energy, which shows that the two PLE resonances appear at the energetic positions of intralayer excitons in monolayer WSe_2 (~1.72 eV) and monolayer $MoSe_2$ (~1.65 eV). This result indicates that the PL comes from interlayer excitons[123,138], which are excited through photon absorption in either monolayer TMD, followed by ultrafast interlayer charge transfer and subsequent formation of interlayer exciton, as illustrated in the insets of Figure 8-2C.

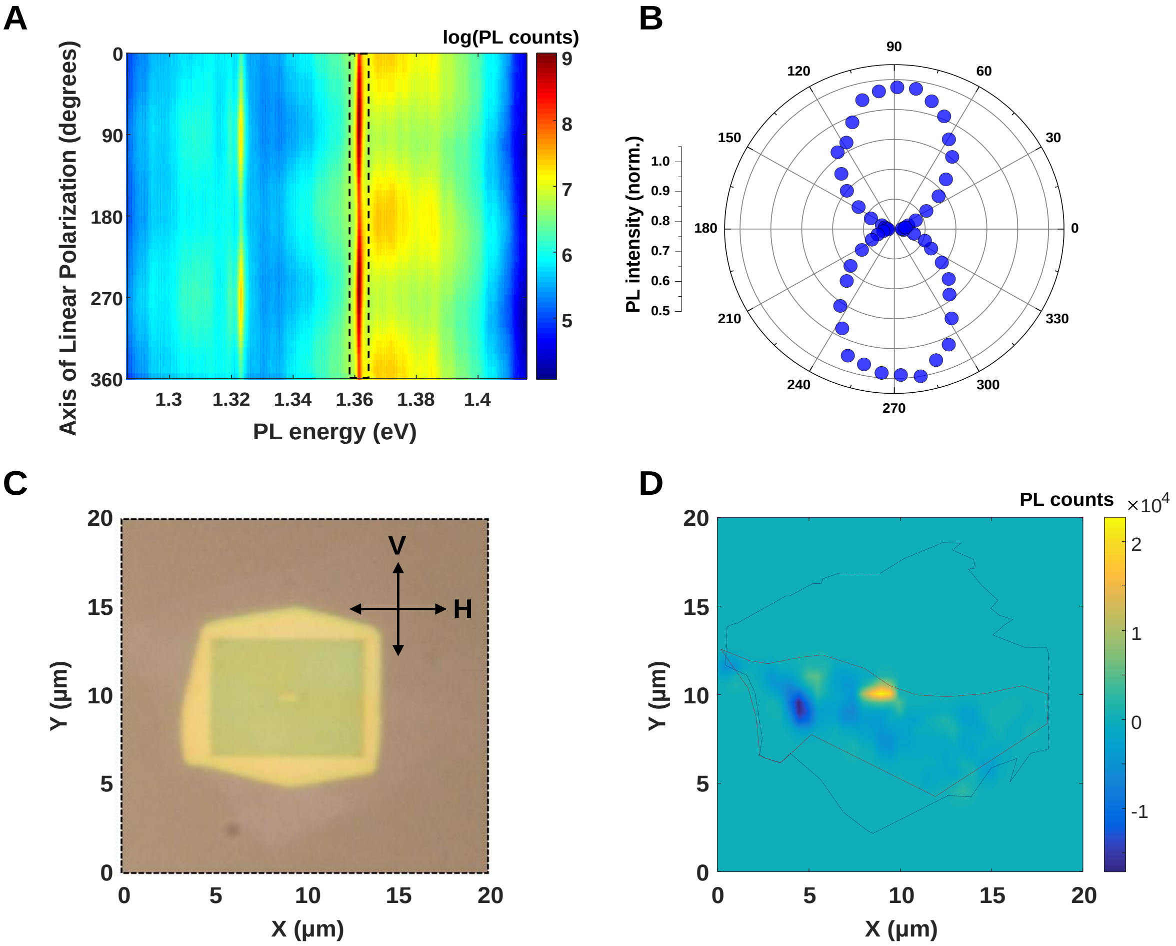

Figure 8-3 | Polarization of cavity-enhanced interlayer exciton PL. (A) Polarization-resolved photoluminescence (PL) from the interlayer exciton ON the photonic crystal (PhC) cavity, in the linear basis. **(B)** Integrated PL intensity in resonance with the higher energy PhC cavity mode (region outlined by dashed black lines in A). The major axis of the linear polarization is along the vertical direction (V axis). **(C)** Optical image of the sample during spectroscopic measurements. The V and H axes correspond to 90° and 0° in B. **(D)** Spatial map of the cavity-enhanced PL, given by the difference between the V and H polarized emission intensity in resonance with the higher energy PhC cavity mode. The monolayers of $MoSe_2$ and WSe_2 are outlined in blue and red, respectively. The peak intensity of the cavity-enhanced PL is located on the L3 cavity of the PhC.

8.6 Spatial and polarization dependence of cavity-enhanced interlayer exciton

The polarization of the interlayer exciton PL from the heterobilayer ON the cavity was then analyzed in the linear basis. Polarization specific detection was accomplished by first directing the

PL through an achromatic $\lambda/2$ waveplate (Newport 10RP52-2), then through a stationary linear polarizer before entering the monochromator. The polarization-resolved PL spectra measured ON the cavity (Fig. 8-3A) show strong linear polarization of the cavity-coupled PL for both cavity resonances. The integrated PL at the higher energy cavity resonance (ω_1) is plotted as a function of the axis of linear polarization in Figure 8-3B. Comparison of the major axis of the linearly polarized PL with the orientation of the photonic crystal (Fig. 8-3C) shows that it is directed along the V axis of the L3 cavity. By scanning the objective lens, we also performed confocal spatial mapping of the polarization dependence of the PL response across the entire photonic crystal. The polarization-resolved spatial PL maps reveal a sharp peak in the intensity of V-polarized PL located ON the cavity that is absent from the spatial map of the H polarized PL intensity. The spatial map of the cavity-enhanced PL $(I_{\mathrm{PhC}} \equiv I_{\mathrm{V}} - I_{\mathrm{H}})$ is shown in Figure 8-3D, which reveals that I_{PhC} is spatially localized to the cavity.

8.7 Discussion

The spectroscopic results presented here demonstrate the coupling of the interlayer exciton in the $MoSe_2$-WSe_2 heterobilayer to the cavity of a PhC. In this sample, the cavity-exciton coupling strength is found to be in the weak regime, resulting in approximately one order of magnitude enhancement of the PL from interlayer excitons in resonance with the PhC cavity modes. The coupling strength is limited by the fact that the heterobilayer is not embedded within the cavity, but simply placed on top of it, which restricts the exciton-cavity interaction to evanescent fields. The long non-radiative lifetime and non-exponential decay dynamics of the interlayer exciton precludes the determination of the Purcell factor (see Fig. C3 in Appendix C). Meanwhile, the cavity-enhanced PL from the interlayer exciton exhibits strong linear polarization oriented along the V axis of the PhC, which corresponds to the polarization of the transverse electric cavity mode supported by the L3 cavity in our PhC (see Fig. C4 in Appendix C). Under the electric dipole approximation, this implies that the optical coupling of the spatially-indirect electron and hole comprising the interlayer exciton is primarily oriented in the plane of the heterobilayer, which is consistent with theoretical predictions.

8.8 Acknowledgements

Xiaodong Xu and Arka Majumdar conceived the project. Taylor K. Fryett fabricated and characterized the photonic crystal cavity. Essance Ray fabricated the heterobilayer and transferred it to the photonic crystal cavity. I performed spectroscopic the measurements, with help from Chang-Hua Liu. Xiaodong, Arka, and I analyzed the data. Jiaqiang Yan and David Mandrus provided the high quality bulk $MoSe_2$ and WSe_2 crystals. Takashi Taniguchi and Kenji Watanabe provided the bulk hBN crystals. Fariba Hatami provided the GaP crystal. I wrote the paper with some help from Arka and Xiaodong. Please see below for the author list and their affiliations.

Author List: Pasqual Rivera[1], Taylor K. Fryett[2], Chang-Hua Liu[1,2], Essance Ray[1,3], Fariba Hatami[4], Takashi Taniguchi[5], Kenji Watanabe[5], Jiaqiang Yan[6,7], David Mandrus[6,7,8], Arka Majumdar[1,2*], Xiaodong Xu[1,3*]

Affiliations:

[1]Department of Physics, University of Washington, Seattle, Washington, USA

[2]Department of Electrical Engineering, University of Washington, Seattle, Washington, USA

[3]Department of Materials Science and Engineering, University of Washington, Seattle, Washington, USA

[4]Department of Physics, Humboldt-Universität zu Berlin, Berlin, Germany

[5]Advanced Materials Laboratory, National Institute for Materials Science, Tsukuba, Ibaraki, Japan

[6]Materials Science and Technology Division, Oak Ridge National Laboratory, Oak Ridge, Tennessee, USA

[7]Department of Materials Science and Engineering, University of Tennessee, Knoxville, Tennessee, USA

[8]Department of Physics and Astronomy, University of Tennessee, Knoxville, Tennessee, USA

Chapter 9: Interlayer excitons and trions trapped in the moiré potential

9.1 Overview

Over my career in the Xu Laboratory, many hours (understated) were spent fabricating $MoSe_2$-WSe_2 heterobilayers of various architecture and quality. Meanwhile, theoretical efforts started to consider the effects of the moiré potential brought about by the finite lattice mismatch and twist angle of manually assembled heterobilayers. A number of theoretical studies suggested that the moire pattern could have dramatic effects on the potential landscape, as well as the optical coupling of the interlayer excitons[135,147,148]. With the addition of a lower temperature cryostat with magnetic field, we took another look at many of these samples. At the lower temperature, many sharp peaks began to appear on several of the samples, indicating trapped interlayer excitons over large areas. Magnetic field and polarization dependent PL measurements indicated that the trapping potential arose from the moiré superlattice potential, as shown in the following work.

Signatures of moiré-trapped valley excitons in $MoSe_2$-WSe_2 heterobilayers

Abstract: The creation of moiré patterns in crystalline solids is a powerful approach to generating periodic potential landscapes to control the material properties. In two-dimensional (2D) materials, a moiré pattern can form by vertically stacking two layered materials with a twist and/or finite lattice constant difference. This moiré pattern is accompanied by a periodic superlattice potential, which can lead to emergent electronic phenomena, including the fractal quantum Hall effect[28-30], tunable Mott insulators[149,150], and unconventional superconductivity[151]. Furthermore, theory predicts intriguing effects on optical excitations by a moiré potential in TMD heterobilayers[91,147,148], but these signatures have yet to be demonstrated. Here, we report experimental evidence of interlayer valley excitons trapped in the moiré potential formed in $MoSe_2$-WSe_2 heterobilayers. At low temperatures, we observe photoluminescence near the *free* interlayer exciton energy but with over 100 times narrower linewidths (~100 μeV), indicating the presence of localized emitters. The emitter g-factors are homogeneous across the same sample and only take two values, -15.9 and 6.7, in samples with twisting angles near 60° and 0°, respectively. The g-factors match those of the free interlayer exciton, which is determined by one of two possible

valley pairing configurations. At a twist angle near 20°, the emitters become two orders of magnitude dimmer, but they possess the same *g*-factor as the heterobilayer near 60°, a remarkable signature of the Umklapp recombination of interlayer excitons near the commensurate 21.8° twist angle[91]. The localized interlayer excitons also exhibit strong circular polarization, which implies a smooth trapping potential that preserves the three-fold rotational symmetry. These facts, combined with the power and excitation energy dependence reported herein, cause us to ascribe the emitters to interlayer excitons trapped in a smooth moiré superlattice potential. Our results open opportunities for 2D moiré optics with twist angle dependent control.

9.2 Introduction

Heterobilayers formed by monolayer semiconducting transition metal dichalcogenides are a fascinating system for exploring nanoscale semiconductor optoelectronics with valley functionality[139,152]. Vertically stacked MoSe$_2$ and WSe$_2$ monolayers, for example, exhibit an atomically sharp interface and type-II band alignment which hosts interlayer excitons—the Coulomb bound state between electrons and holes located in different monolayers[153]. Under circularly polarized optical pumping, electrons and holes preferentially populate the ±K valleys in the MoSe$_2$ conduction band and WSe$_2$ valence band, respectively. This allows for the formation of interlayer excitons with a plethora of appealing properties, such as valley-contrasting physics[91,97,139,140,147,154], long population and valley lifetimes[123,138,139,141], high electrical tunability[123,139,14210,15,18], and strong many-body interactions[123,138,13910,15,16].

One enticing possibility, which has so far only been theoretically explored, is to harness the spatially periodic moiré superlattice potential for excitonic manipulation. Recent scanning tunneling microscopy/spectroscopy measurements have directly measured the moiré pattern of 2D semiconductor heterobilayers, showing a periodically varying interlayer separation and electronic band gap approaching ~150 meV[99]. The periodicity of this moiré superlattice is determined by the lattice constant mismatch and twist angle (θ) between the layers (Fig. 9-1A). When the moiré period is larger than the interlayer exciton Bohr radius (~1 nm), the excitons will experience a spatially periodic potential modulation, forming a solid-state analogue of a bosonic quantum gas in an optical lattice[155]. The moiré potential minima function as smooth confinement potentials (Fig. 9-1B), but they uniquely preserve the local three-fold rotational (C$_3$) symmetry[147,148]. Therefore, interlayer excitons confined by the superlattice potential should inherit valley-contrasting properties, a feature which distinguishes them from excitons bound to other randomly formed potential traps (e.g. defects, impurities, strain, etc.).

9.3 Sample details

In this work, we report experimental signatures of interlayer excitons trapped in a moiré potential in $MoSe_2$/WSe_2 heterobilayers. The samples consist of exfoliated monolayers of $MoSe_2$ and WSe_2, stacked using a dry-transfer technique and aligned deterministically with 1° uncertainty. Additionally, these samples are encapsulated between ~10 to 30 nm hexagonal boron nitride to provide atomically smooth substrates and protection from exposure to the ambient environment. Data from two devices are presented in the main text. Each device contains two heterobilayers that were simultaneously fabricated from the same pair of monolayers, but have regions with different θ (see Methods). This procedure minimizes the uncertainties when comparing the interlayer exciton properties at different twist angles. Device 1 contains heterobilayers with $\theta = 2^{o}$ and 20^{o} (Fig. 9-1C), while device 2 has regions with $\theta = 6^{o}$ and 57^{o}. For sample specific details, see Methods.

9.4 Temperature and power dependent PL from trapped interlayer excitons

$MoSe_2$/WSe_2 heterobilayers with aligned crystallographic axes generally exhibit bright interlayer exciton photoluminescence (PL) around 1.3 to 1.4 eV with a typical linewidth $\gtrsim$10 meV. Figure 9-1D shows PL spectra from the $\theta = 2°$ and 20° regions of device 1 under 5 µW 632.8 nm HeNe laser excitation (beam spot size ~ 1 µm^2) at a temperature of 1.6 K. For further details, see Methods. In both heterobilayer regions, the intralayer exciton PL near 1.65 eV is strongly quenched relative to PL from the isolated monolayers due to ultrafast interlayer charge transfer[94]. However, there is a stark contrast in the interlayer exciton PL intensity, with the 2° region being over two orders of magnitude brighter than the 20° region. This is due to the large mismatch of the first Brillouin zone corners between electrons and holes in 20° heterobilayer, which strongly suppresses the PL quantum yield compared to the nearly aligned 2° sample.

Under much lower excitation power (20 nW) near the monolayer WSe_2 A exciton resonance (1.72 eV), the broad interlayer PL develops into several narrow peaks near the free interlayer exciton energy around 1.33 eV (Fig. 9-1E and Appendix D, Fig. D-1), which are fit well by

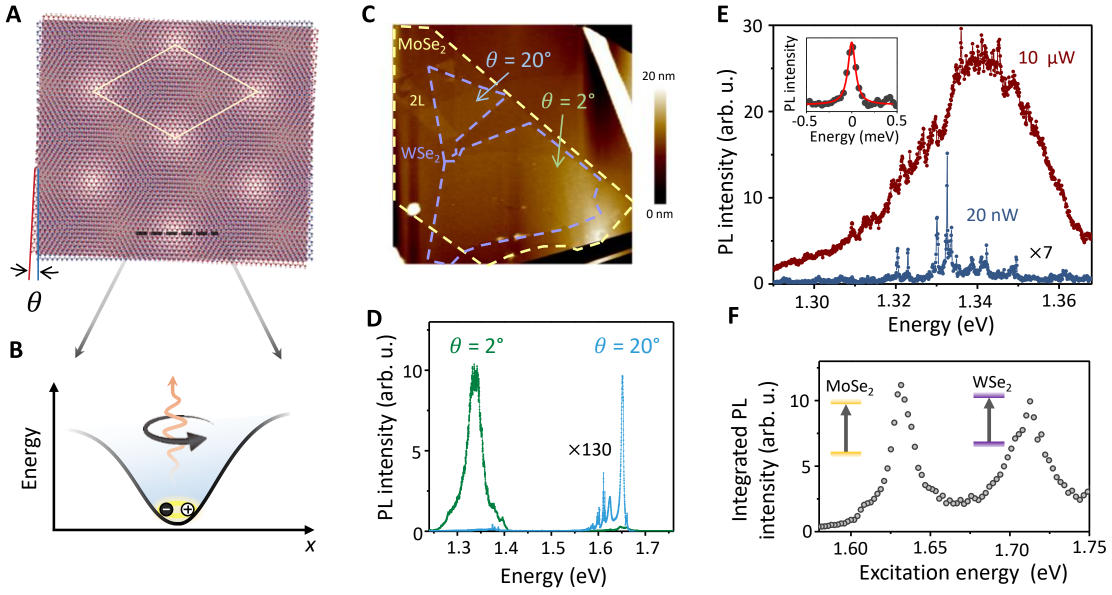

Figure 9-1 | Moiré superlattice potential and observation of trapped interlayer excitons. (A) Illustration of the moiré superlattice formed in a heterobilayer with twist angle θ. **(B)** Cartoon of an exciton trapped in a moiré potential. **(C)** Topographical height map of $MoSe_2/WSe_2$ heterobilayers encapsulated by hexagonal boron nitride, obtained from an atomic force microscope. Orange and purple solid lines indicate the $MoSe_2$ and WSe_2 monolayers, respectively. The heterobilayers have different twist angles, as indicated. **(D)** Photoluminescence (PL) spectra from the heterobilayer with 2° (green) and 20° (blue, intensity scaled by 130×) twist angle, at 5 μW excitation power. **(E)** Comparison of interlayer exciton PL from the 20° twist angle heterobilayer at 10 μW (orange) and 20 nW (purple, intensity scaled by 7×) excitation power. Inset, Lorentzian fit to a representative PL peak indicates a linewidth of ~100 μeV (20 nW excitation power). **(F)** PL excitation intensity plot on a narrow PL peak showing two prominent resonances corresponding to the intralayer exciton states in the monolayers of $MoSe_2$ and WSe_2. The intensity is integrated over a single peak of the θ = 57° sample, but the results are qualitatively similar for all other emission lines on each sample.

Lorentzian curves (Fig. 9-1E, inset). The average linewidth of the observed peaks is about 100 μeV, which is comparable to the quantum emitters reported in monolayers of WSe_2[63,65,66,156] and hexagonal boron nitride[157], and two orders of magnitude narrower than previous reports of interlayer exciton PL[97,138-141,154,158]. Narrow PL peaks and power broadening were also observed in the 57° and 20° sample (Appendix D, Fig. D-1).

The evolution of the broad interlayer PL peak into several narrow lines at low power suggests that the interlayer excitons are confined. The strong power saturation and broadening is characteristic of trapped excitons, where under high-power excitation, the traps are filled, and the emission becomes dominated by delocalized excitons that have broadened linewidth. Moreover, the narrow-line emission is suppressed above 30 K, after which the broader PL peaks dominate the spectrum (Appendix D, Fig. D-2). To substantiate the assignment of these features to interlayer excitons, we performed low-power PL excitation (PLE) spectroscopy, scanning a continuous-wave laser from 1.55 to 1.77 eV while monitoring the intensity of the narrow PL peaks. The PLE spectrum in Fig. 9-1F features two prominent resonances, consistent with the absorption of the $MoSe_2$ and WSe_2 intralayer excitons, which establishes the interlayer exciton character of the narrow PL lines.

9.5 Valley polarization of the trapped interlayer exciton PL

The trapped interlayer excitons exhibit strong valley polarization. Figure 9-2 shows circular polarization-resolved PL spectra under σ^+ excitation for heterobilayers with $\theta = 57°$, 20°, and 2°. Denoting the valley polarization $\eta = \frac{I_+ - I_-}{I_+ - I_-}$, where $I_\pm$ is the $\sigma^\pm$ PL intensity, the narrow peaks in the 57° and 20° heterobilayers display over 70% valley polarization (Figs. 9-2A and B). On the other hand, the selection rule is reversed for the 2° sample, with σ^-emission dominating under σ^+excitation (i.e. $\eta < 0$). Using σ^- excitation, we confirmed the time-reversal process, establishing the observation of co-circularly polarized PL for 57° and 20° and cross-circularly polarized PL for 2° (Appendix D, Fig. D-3). Furthermore, under linearly polarized excitation, no significant linear PL polarization components were detected (Appendix D, Fig. D-4). Additional samples near 0° and 60° stacking show similar narrow PL features and polarization properties (Appendix D, Fig. D-3).

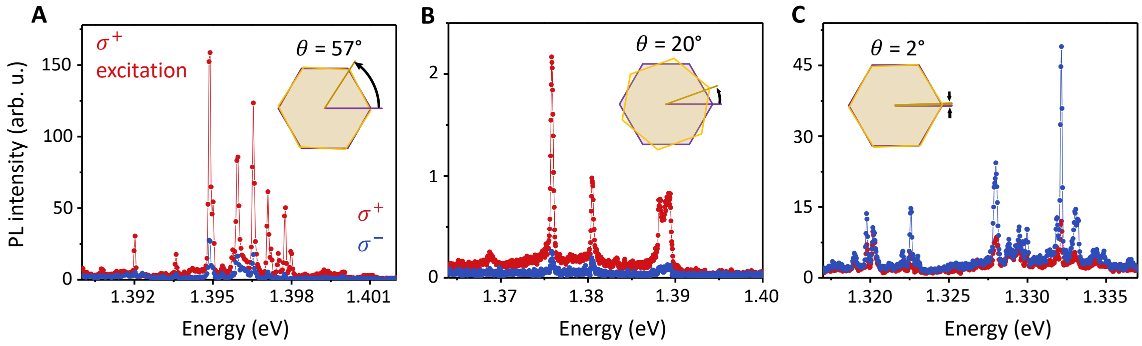

Figure 9-2 | Valley polarization of trapped interlayer excitons. Helicity-resolved photoluminescence (PL) spectra of trapped interlayer excitons of $MoSe_2/WSe_2$ heterobilayers with twist angle of **(A)** 57°, **(B)** 20°, **(C)** and 2°. Insets illustrate the twist angle of the three samples. The samples are excited with σ^+-polarized light at 1.72 eV. The σ^+ and σ^- components of the PL are shown in red and blue, respectively. The PL from heterobilayers with twist angles of 57° and 20° are co-circularly polarized, while PL from the heterobilayer with twist angle of 2° is cross-circularly polarized.

The circular polarization properties of the trapped interlayer excitons are distinct from the quantum emitters reported in monolayer materials, which exhibit either intrinsically linearly or unpolarized PL[63,65,66,156]. In those systems, high magnetic fields or trion formation under strong electron doping are required to restore modest circularly polarized PL. Fine structure splitting observed in linearly polarized monolayer emitters implies anisotropy of the trapping potential, which breaks the three-fold rotational symmetry of the host lattice[65]. While the exact origin of the quantum emitters in monolayers is currently unclear, they are generally thought to arise from excitons bound to defects[159], impurities, or strain-induced potential traps[69,70]. However, unlike the monolayer case, the strong circularly polarized PL from the trapped interlayer excitons implies that the confining potential must possess three-fold rotational symmetry. One possible origin for the observed exciton trapping in the heterobilayer is the potential landscape resulting from the moiré superlattice, which naturally forms arrays of confinement centers with local atomic configurations that maintain C_3 symmetry[148]. This preserves valley optical selection rules and generally allows for cross-circularly polarized emission by interlayer excitons[91,97,135,158,160], which will be discussed later.

9.6 Magneto-PL and twist angle dependent g-factors

To support the moiré potential assignment, we performed magneto-PL spectroscopy to determine the Landé g-factor of trapped interlayer excitons. In Figs. 9-3A-C, we show circularly polarized PL under linearly polarized excitation as a function of perpendicular magnetic field B for heterobilayers with $\theta = 57°$, 20°, and 2°, respectively. The linearly polarized excitation equally pumps the degenerate ±K valleys of the monolayers, resulting in equal intensity and energy for σ^+ and σ^- PL at 0 T. For nonzero magnetic fields, σ^+ and σ^- PL split strongly in energy due to the valley Zeeman effect[161-165], but otherwise maintain the same peak structures, as illustrated by the spectra at 3 T (top row of Fig. 9-3). We visualize the full magnetic field dependence by plotting the total PL intensity versus the emission energy and B (middle row of Fig. 9-3). For a given twist angle, we observe that for *all* PL peaks, the energies of σ^+ and σ^- emission shift equally and oppositely to one another. Since several of the peaks are closely spaced in energy (~1 meV or less), the large energy shifts cause crossing points between the σ^+ and σ^- emission of different PL peaks at high magnetic fields.

The bottom row of Fig. 9-3 shows the energy difference between the $\sigma^{\pm}$ PL ($\Delta = E_{\sigma^+} - E_{\sigma^-}$, where $E_{\sigma^{\pm}}$ is the peak energy of $\sigma^{\pm}$ polarized PL) of representative trapped interlayer excitons in each twisted heterobilayer. The extracted g-factor of 6.72 $\pm$ 0.02 for θ = 2° heterobilayer is nearly the same as the free interlayer exciton in near 0° samples (Appendix D, Fig. D-5). For θ = 57°, the effective g-factor is -15.89 $\pm$ 0.03, which is also very close to the g-factor of -15.1 reported for free interlayer excitons in 54° twisted heterobilayer[154]. We found that the g-factor is not only uniform between different trapped interlayer excitons in the same heterobilayer, but also nearly the same for different heterobilayers with similar twist angle (Appendix D, Fig. D-6).

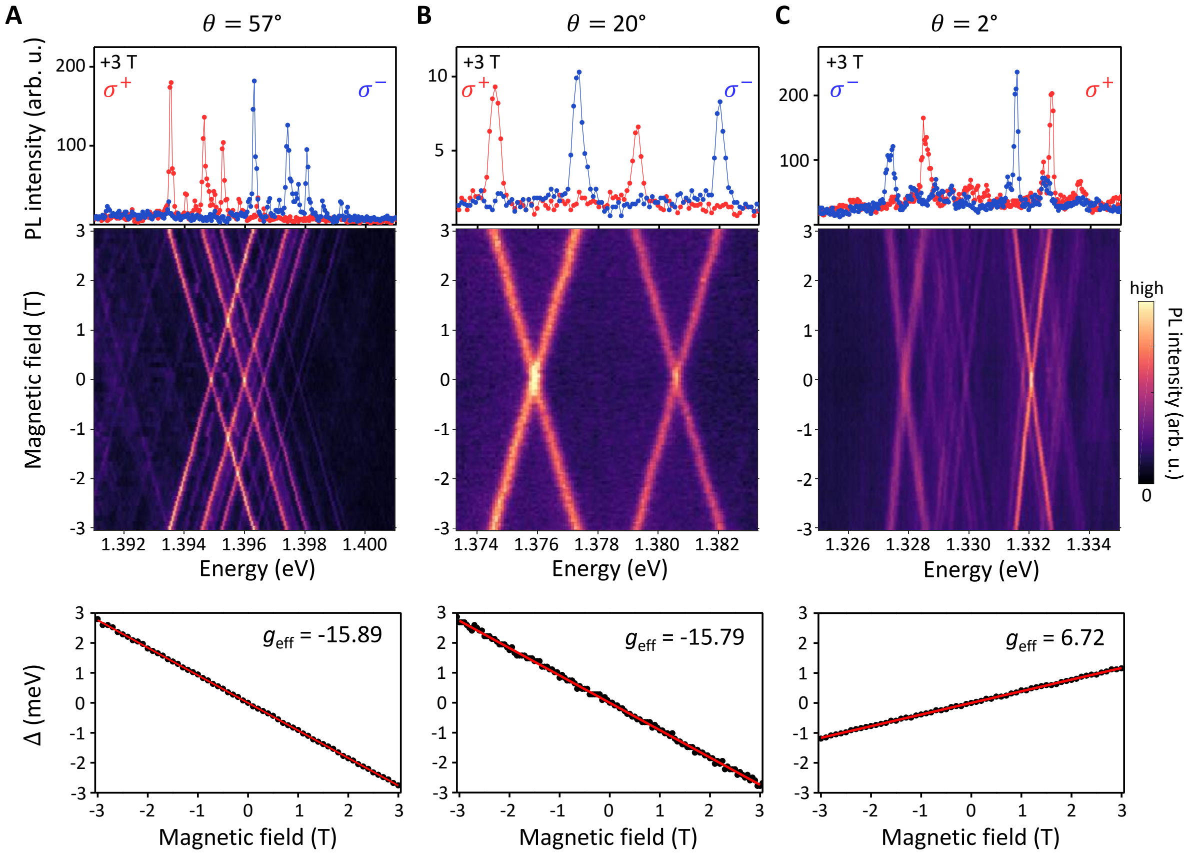

Figure 9-3 | Twist-angle-dependent Zeeman splitting of trapped interlayer excitons. Magnetic-field-dependent photoluminescence (PL) from interlayer excitons in the $MoSe_2/WSe_2$ heterobilayer with twist angle of **(A)** 57°, **(B)** 20°, **(C)** and 2°. Top row: Helicity-resolved PL spectra at 3T. The excitation is linearly polarized, and the σ^+ and σ^- components of the PL are shown in red and blue, respectively. Middle row: Total PL intensity plot as a function of magnetic field, showing a linear Zeeman shift of the σ^+ and σ^- polarized PL. Bottom row: Zeeman splitting of the polarization-resolved PL ($\Delta = E_{\sigma^+} - E_{\sigma^-}$) as a function of the applied magnetic field. The effective g-factors for the three samples (-15.89 ± 0.02, -15.79 ± 0.05, and 6.72 ± 0.02 for **(A)**, **(B)**, and **(C)**, respectively) are extracted from a linear fit of Δ versus B (red solid line).

9.7 Zeeman shift contributions by twist angle

The valley magnetic moment plays a central role in the distinct g-factors between nearly 0° and 60° heterobilayers. The Zeeman shift of carriers in the valley semiconductors has three contributions (Figs. 9-4A, B): spin ($\Delta_s = 2s_z\mu_B B$), atomic orbital ($\Delta_a = l_i\mu_B B$), and a valley contribution ($\Delta_v = \tau\alpha_i\mu_B B$) from the Berry phase effect[162-165]. Here, $\tau = \pm 1$ is valley index, $s_z = \pm 1/2$ is electron spin index, μ_B is Bohr magneton, α_i is valley g-factor for the conduction ($i = c$) or valence band ($i = v$), and l_i is the magnetic quantum number for band i ($l_c = 0$ and $l_v = 2\tau$). The Zeeman splitting of the interlayer exciton is then the difference between the Zeeman shifts of conduction band edge in $MoSe_2$ and valence band edge in WSe_2.

For interlayer excitons with spin-conserving optical transitions, spin does not contribute to the exciton Zeeman shift. Furthermore, the atomic orbital contribution to the Zeeman splitting, $-4\mu_B B$, is independent of the twist angle. The major difference between nearly 0° and 60° stacking therefore lies in the valley magnetic moment contribution because of their distinct conduction-valence valley pairing. The bright interlayer exciton configuration can be uniquely specified by the valley index pair (τ_c, τ_v), which is $(+,+)$ or $(-,-)$ for nearly 0° stacking (Fig. 9-4A), and $(+,-)$ or $(-,+)$ for nearly 60° stacking (Fig. 9-4B). Consequently, for 0° stacking, the excitonic Zeeman splitting is similar to monolayers and may be written as $\Delta_0 = -2(2-\Delta\alpha)\mu_B B$, where the valley contribution $\Delta\alpha = \alpha_c - \alpha_v$. For the 60° stacking case, the valley contribution changes from a cancellation to a sum[154], which gives rise to much larger Zeeman shift $\Delta_{60} = -2(2+\Sigma\alpha)\mu_B B$, where $\Sigma\alpha = \alpha_c + \alpha_v$ is the summation of valley g-factors, and thus larger effective interlayer g-factor than 0° stacked heterobilayer (See Appendix D).

9.8 Umklapp-assisted PL from 20° stacked region

From above analysis, we see that interlayer exciton g-factor is a fingerprint of their valley configuration and valley magnetic moment. The defect-localized excitons in monolayers do not possess valley-contrasting properties since the bulk crystal structure is not retained in the extent of the exciton wavefunction. Indeed, excitons bound to defects or strain-confined potentials observed in WSe_2 have distinct g-factors (a few times larger) compared to the free intralayer exciton counterparts, and often exhibit fine structure splitting and absence of circular polarization from the anisotropic quantum confinement[63,65,66,156]. Our observation that the trapped interlayer excitons have the same g-factors and twist angle dependence as the free ones demonstrates that the trapping potential must be smooth and three-fold rotational symmetry must be preserved. These findings strongly suggest that extrinsic factors (defects, impurities, strain) cannot be the origin of the trapping, whereas the moiré potential traps are the only known candidate.

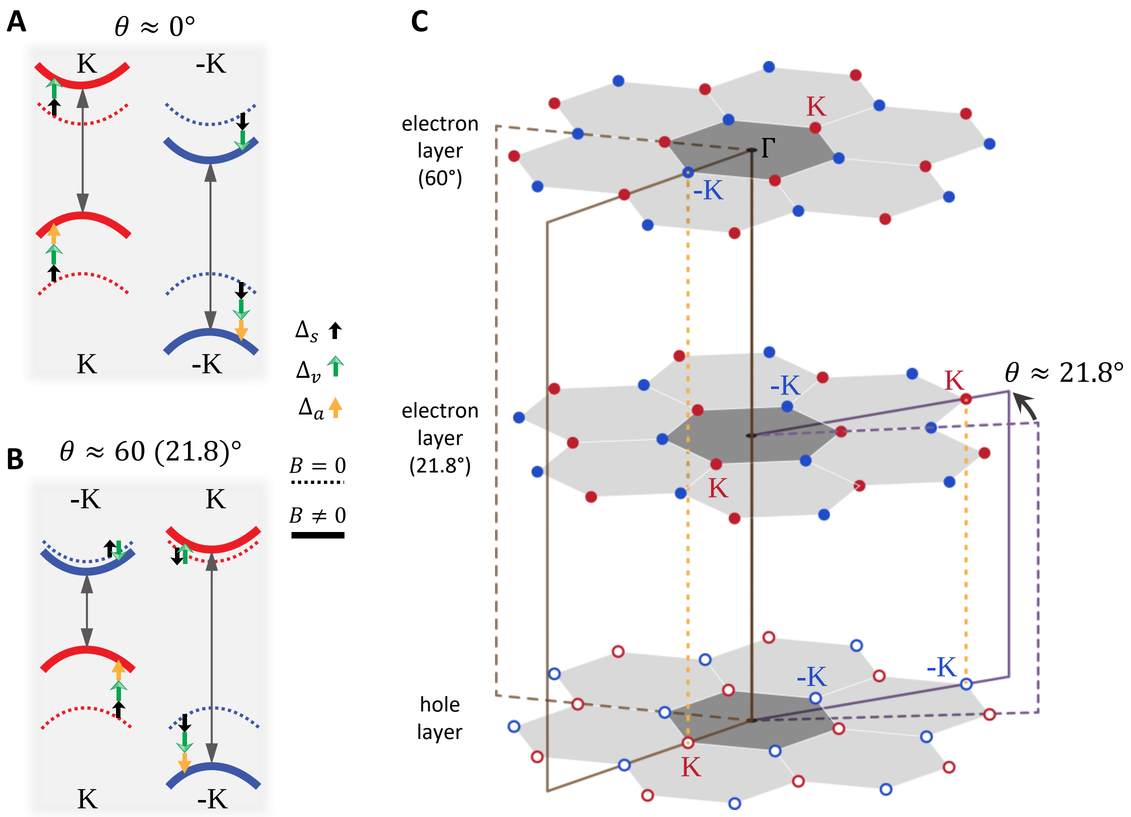

Figure 9-4 | Twist-angle-dependent g-factors and Umklapp light coupling of interlayer excitons. Energy level diagram showing the contributions of the interlayer exciton Zeeman shift by the electron spin (Δ_s, in black), valley (Δ_v, in green), and atomic orbital (Δ_a, in orange) for the $MoSe_2/WSe_2$ heterobilayer with twist angle near **(A)** 0° and **(B)** 60°. **(C)** Schematic of valley alignments in extended Brillouin zone for a twisted heterobilayer. The open and solid points represent the +K (red) and −K (blue) valleys in the hole and electron layers, respectively. Near 21.8° twist angle, the ±K and ∓K valleys align in the second Brillouin zone, which has the same valley pairing as the 60° twisted heterolayer and thus the same g-factor. Light coupling at 21.8° is facilitated by an Umklapp-type process.

Another remarkable finding which further supports the above picture is that the g-factor of interlayer excitons for $\theta = 20°$ is -15.78 ± 0.05 (bottom row, Fig. 9-3C), which is nearly the same as that of $\theta = 57°$ heterobilayer. This, at the first glance, is counterintuitive, as 20° is closer to 0° than to 60°. The mystery is solved by noticing that 21.8° is a commensurate stacking angle[91] that produces the shortest superlattice periodicity, with a supercell of size $\sqrt{7}a \times \sqrt{7}a$. Figure 9-4C shows the conduction (solid points) and valence band edges (open points) of heterobilayer in the extended Brillouin zone scheme, where red and blue denote +K and -K valley respectively. For a random twist angle, the valleys from $MoSe_2$ and WSe_2 are in general not aligned in momentum space, and thus interlayer excitons are momentum-indirect and optically dark. At 21.8° twisting angle, the conduction and valence band ±K points are misaligned in the first Brillouin zone but overlap on the second Brillouin zone, with the $(+,-)$ and $(-,+)$ valley pairings. As a result, the interlayer exciton at this commensurate stacking can directly couple to light for radiative recombination, with the momentum mismatch from the twisting compensated by the reciprocal lattice vectors from the two layers (i.e. Umklapp recombination)[91]. Since the valley pairings of 21.8° are the same as for 60° twisted heterolayers, they have the same g-factor. The optical dipole of the Umklapp recombination is expected to be very weak compared to that of the direct recombination at 0° and 60°. Indeed, our measurement reveals the PL intensity of $\theta = 2°$ is about 100 times stronger than that of $\theta = 20°$ (Appendix D, Fig. D-7).

Our heterobilayer of $\theta = 20°$ forms an interesting concatenated moiré pattern, as schematically shown in Appendix D, Fig. D-8. Close-up views of any local region resemble the commensurate moiré pattern of the 21.8° stacking, but the interlayer translation varies smoothly over a longer length scale with the periodicity $\mathrm{A} = \frac{a}{\sqrt{7}\delta\theta}$. Here, $\delta\theta$ is the small deviation of the actual twisting angle from the commensurate angle of 21.8°, and $\mathrm{A} \approx 4$ nm at $\theta = 20°$. In this concatenated moiré supercell, we can also identify three local regions that retain the three-fold rotational symmetry, which must correspond to either the minima or maxima of the moiré superlattice potential for the interlayer excitons (see Appendix D). As with the $\theta = 2°$ and $\theta = 57°$ moiré pattern, interlayer excitons in our 20° heterobilayer trapped in such potential minima can retain circularly polarized valley optical selection rules, consistent with the high degree of PL polarization observed. The experimental observations of narrow-line emission, circular selection rules, and distinct binary g-factors at a variety of twisting angles are compelling evidence of interlayer excitons trapped in moiré superlattice potential.

9.9 Discussion

Finally, we remark on some subtle features in the observed moiré-trapped interlayer excitons. The polarization of PL is determined by local crystal symmetry of moiré potential. Theory shows two high-symmetry points, A and B, in the moiré superlattice[91,148]. The former has co-circular optical selection rules, while the latter has circular polarization reversal. Our experiment implies the moiré exciton is located at the B point of the moiré supercell for $\theta = 2°$, and the A point for $\theta = 20°$ and $\theta = 57°$. This also explains why the g-factor we measured was positive for $\theta = 2°$ but negative for $\theta = 20°$ and $\theta = 57°$, because the Zeeman splitting is defined as the energy difference between $\sigma^{\pm}$ PL (See Appendix D.1).

The moiré-trapped interlayer excitons we observe are nonuniform in the number of emitters, their relative intensities, and their energies. We often detect several narrow PL peaks with sub-meV energy separation within the laser excitation spot. The intensities and valley polarization can also vary significantly between the peaks (Appendix D, Fig. D-9). These observations imply that the moiré superlattice potential has some inhomogeneity, which is not surprising because imperfections are expected during fabrication of the moiré superlattice. In fact, fabricating a homogenous moiré pattern by mechanical transfer is an open challenge in the community. On the other hand, different emitters for similar stacking configurations have a common g-factor, which is expected in a moiré potential trap but *not* in other extrinsic traps. As we mentioned, the g-factor of the moiré exciton is a property of the heterobilayer bulk determined by the valley pairing only, which is the same for every local region of a given moiré pattern. Lastly, considering that the energy spacing of several PL lines is on the same order as the repulsive interaction between proximate interlayer excitons, there is a possibility that some of the narrow PL peaks may originate from the cascaded emission of multi-exciton states in a single trap or several neighboring traps[153]. All these possibilities require future studies with improved sample quality and possibly new scanning probe techniques, such as near-field scanning microscopy with sub-10 nm spatial resolution. Nevertheless, our observation of moiré excitons provides a promising starting point to explore several intriguing theoretical proposals related to quantum photonics, such as entangled photon sources, giant spin-orbit coupling[147], topological excitons[147,160], and much more.

9.10 Methods

Sample fabrication

The samples were fabricated by dry-transfer of monolayers obtained from the mechanical exfoliation from bulk crystals. The crystal orientation of the individual monolayers was determined by linear-polarization-resolved second-harmonic generation[139] prior to transfer. During the transfer process for device 1, a region of the WSe_2 monolayer tore off and twisted 18° relative to the original piece (see Fig. 9-1C). This yield heterobilayers with $\theta = 2°$ and 20°. Device 2 was fabricated from a large WSe_2 monolayer and a $MoSe_2$ piece with two overlapping monolayers (monolayer-bilayer-monolayer). The two $MoSe_2$ monolayer regions are formed from different layers of a 2H-bilayer, so they were oriented 180° relative to one another prior to transfer. Therefore, after transfer, device 2 possessed two heterobilayer regions, one with near 0° twist angle (6°) and another close to 60° (57°). The difference in twist angle between the two heterobilayer regions deviates from the expected 60° because one of the $MoSe_2$ monolayer regions rotated slightly during transfer. To verify the absolute stacking orientation, we used a phase-resolved second-harmonic generation technique, as described in our previous work [166]. This yielded a reference heterobilayer sample with 56° twist angle, on which we measured a g-factor near -15.9 (Appendix D, Fig D-6C). The two regions of device 2 were then measured to have a g-factor of 6.7 and -15.9, which confirmed their different stacking orientations as well as the general correspondence between samples with twist angle near 0° or 60° and their g-factor. The absolute twist angle for samples with near 0° or 60° was ultimately determined by the g-factor (close to 6.7 for $\theta \approx 0°$ and close to -15.9 for $\theta \approx 60°$).

PL measurements

PL measurements were performed in a home-built confocal microscope in reflection geometry, with the sample mounted in an exchange-gas cooled cryostat equipped with a 9 T superconducting magnet in Faraday configuration. The sample temperature was kept at 1.6 K, unless otherwise specified. A power-stabilized and frequency-tunable narrow-band continuous-wave Ti:sapphire laser (M^2 SolsTiS) was used to excite the sample, unless otherwise specified. The PL was spectrally filtered from the laser using a long-pass filter before being directed into a spectrometer, where the PL was dispersed by a diffraction grating (600 or 1200 grooves/mm) and detected on a Si charge-coupled-device. At the interlayer PL energies of ~1.4 eV, the spectral resolution was ~160 μeV for the 600 grooves/mm grating (Figs. 9-1D-E, 9-2B, 9-3B) and ~80 μeV for 1200 grooves/mm (Figs. 9-1E inset, 9-2A, 9-2C, 9-3A, 9-3C). Polarization-resolved PL data were acquired using a combination of quarter-wave plates, half-wave plates, and linear polarizers for excitation and collection.

9.10 Acknowledgements

Xiaodong Xu, Wang Yao, Kyle L. Seyler, and myself conceived the experiment. I fabricated the devices, assisted by Kyle and Essance Ray. We also acknowledge significant efforts in fabrication by Jordan Fonseca, and the g(2) measurements attempted by Edo Waks (data not shown here). Kyle and I performed the measurements, assisted by Nathan P. Wilson. Kyle, Xiaodong, Wang, Hongyi, and I analyzed and interpreted the results. Jiaqiang Yan and David Mandrus provided the high quality bulk $MoSe_2$ and WSe_2 crystals. Takashi Taniguchi and Kenji Watanabe provided the bulk hBN crystals. Kyle L. Seyler wrote the paper with assistance from Xiaodong Xu, Wang Yao, Hongyi Yu, and myself.

Chapter 10: Outlook

The unique aspect of the TMD heterobilayer system is the unprecedented control over the band structure given by the ability to tune the twist angle. Since the underlying band structure determines the properties of the interlayer exciton, there are exciting possibilities for future explorations in this system. In fact, this system is on the rise in the condensed matter community[153], and many researchers will pick up where I have left off to explore the possibilities. I think the following possibilities are the most intriguing:

The ultralong population lifetime of the interlayer exciton may be combined with its ultralong valley lifetime to manifest a real valleytronic system. Considering that the rotationally mismatched heterobilayers have yet to be studied, both these timescales may be extended by several more orders of magnitude to make this technology competitive with current devices on the marketplace that exploit the spin of the electron. Moreover, the ability to operate valley-exciton devices is a provocative possibility for future engineering of optoelectronics. In order to realize such devices, a new means of reading out the valley information in the heterobilayer must be found, other than through light emission. A potential solution is to exploit the valley-dependent Berry curvatures of the interlayer excitons, which cause spin-valley Hall effects which generate valley currents. These valley currents can be introduced either through exciton transport or resonant optical injection at the finite velocity light cones with linearly polarized light[91,167].

Another intriguing possibility is to exploit the dipolar nature of the interlayer exciton to control its motion in the plane. This could be used to construct excitonic circuits[168,169], where the controlled flow of the excitons can be used to process information. From results not disclosed here, I am certain that this will work. The possibility to probe the interlayer exciton in such circuits could then rely on Coulomb drag effects[170]. When coupled with large valley polarizations, it may also be possible to direct the exciton current using electrodes, while probing the valley information using magneto-optical Kerr effects. This is particularly attractive for large twist angle heterobilayers, where I expect the valley information will be strongly preserved, especially at low temperatures. Considering that there are predictions of correlated excitonic behaviors, such as the formation of excitonic Bose gases and superfluidity, at relatively high temperatures compared to conventional indirect exciton systems[129], these prospects could very well become a powerful reality.

In my opinion, the most fascinating aspect of this new system lies in the intrinsic moiré superlattice potential uncovered in Chapter 9. The possibility of generating large areas of homogeneous arrays of long-lived quantum emitters with protected valley degrees of freedom is tantalizing. Moreover, the fact that the superlattice minima also have well-defined optical selection rules[147] makes this a highly desirable platform for probing the fundamental physics of interacting bosons. If it is possible to control the twist angle, the interaction between excitons could also be controlled *in situ*, which would allow for careful studies of density-dependent interactions. Furthermore, since the superlattice period is much smaller than the emission wavelength, many different sites can collectively couple to the same optical mode, which could allow for intriguing quantum optic applications, including entangled-photon lasers[171] and topological photonics[172].

I anticipate that based on the possibilities discussed above (and undoubtedly many more that I failed to mention) this field will attract even more researchers in the near future. However, above and beyond that it is my firm belief that this system and these possibilities are but just a hint of the upcoming technologies that will be enabled by van der Waals materials engineering. Considering the pace of discovery in the past decade, and the expanding library of 2D materials, there is an enormous amount of work to do on our way to these future technologies. I, for one, can’t wait to get started.

Appendix A: Supporting Materials for Chapter 6

A.1 Supplementary figures

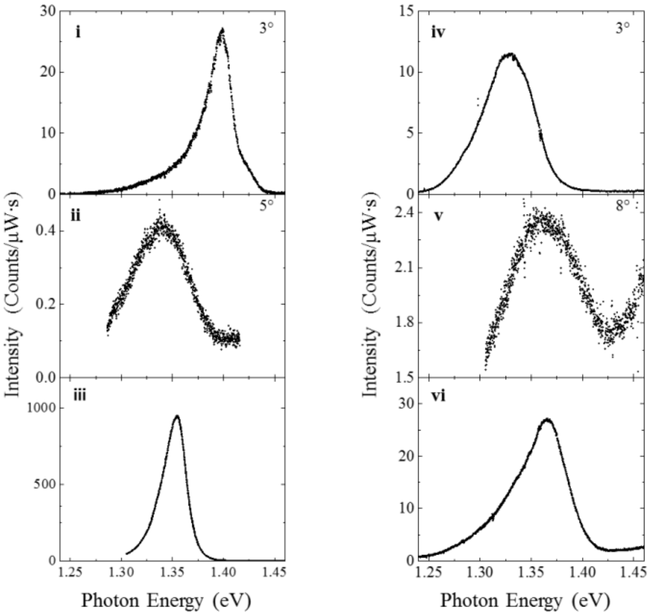

Figure A-1 | Interlayer exciton PL peak position and twist-angle. A Photoluminescence from the interlayer exciton for six WSe2-MoSe2 heterostructures under cw laser excitation at 1.96 eV. The peak position of each heterostructure is influenced by several factors, including the interlayer separation and interlayer exciton density under photoexcitation. Interlayer spacing affects the binding energy of the interlayer exciton, while interlayer exciton density affects the PL energy as a result of dipole-dipole interactions. b, Polarization resolved second harmonic generation in resonance with the intralayer exciton of isolated monolayer MoSe2 and WSe2 from i, which is Device 1 from the main text. We employ polarization resolved second harmonic generation (SHG) for crystal axis determination of individual monolayers1 . The twisting angle, or difference between the crystal axes of the constituent layers of the HS, is inset for those HS where it is possible to discern the angle. For HS i and v, the twisting angle is found from the angular difference between isolated monolayer regions that compose the HS. However, not all devices have isolated monolayers, as they are often covered during the transfer step in the fabrication procedure. Thus, we employ SHG on the attached bulk from which monolayer MoSe2 or WSe2 was exfoliated to determine the angular difference for HS ii and iii. For samples v and vi a single layer completely overlaps an isolated second layer, making the twisting angle indiscernible with this technique. We observe bright interlayer exciton for twisting angles up to 8°. We are unable to conclude any role of the twisting angle from the small sample size used in this report. However, we expect future studies more focused on the stacking orientation of constituent layers to expose the influence of the twisting angle on the properties of the WSe2-MoSe2 heterostructure and interlayer exciton.

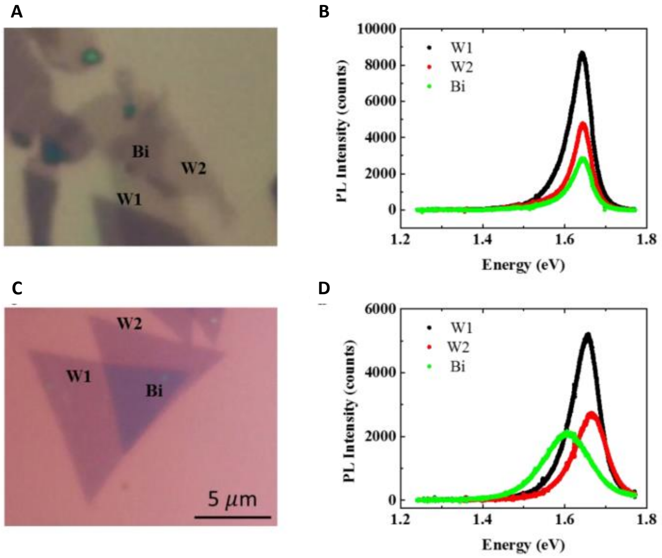

Figure A-2 | Homobilayer WSe2 photoluminescence. Microscope image of a vertically stacked WSe2-WSe2 homostructure from **(A)** exfoliated and **(C)** physical vapor transport (PVD) grown WSe2, with monolayer regions (W1, W2), and bilayer region (Bi) labeled. Photoluminescence spectra of the individual monolayers and the vertically stacked bilayer region from **(B)** exfoliated and **(D)** PVD WSe2-WSe2 homostructure. Notably, there is no low energy photoluminescence that would suggest the presence of interlayer exciton.

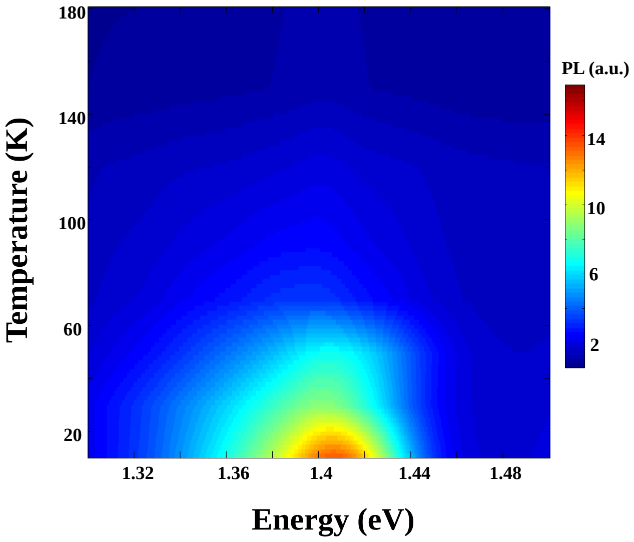

Figure A-3 | Temperature dependence of interlayer exciton. Photoluminescence intensity plot showing decreasing PL intensity of the interlayer exciton with increasing temperatures.

Appendix B: Supporting Materials for Chapter 7

B.1 Supplementary figures

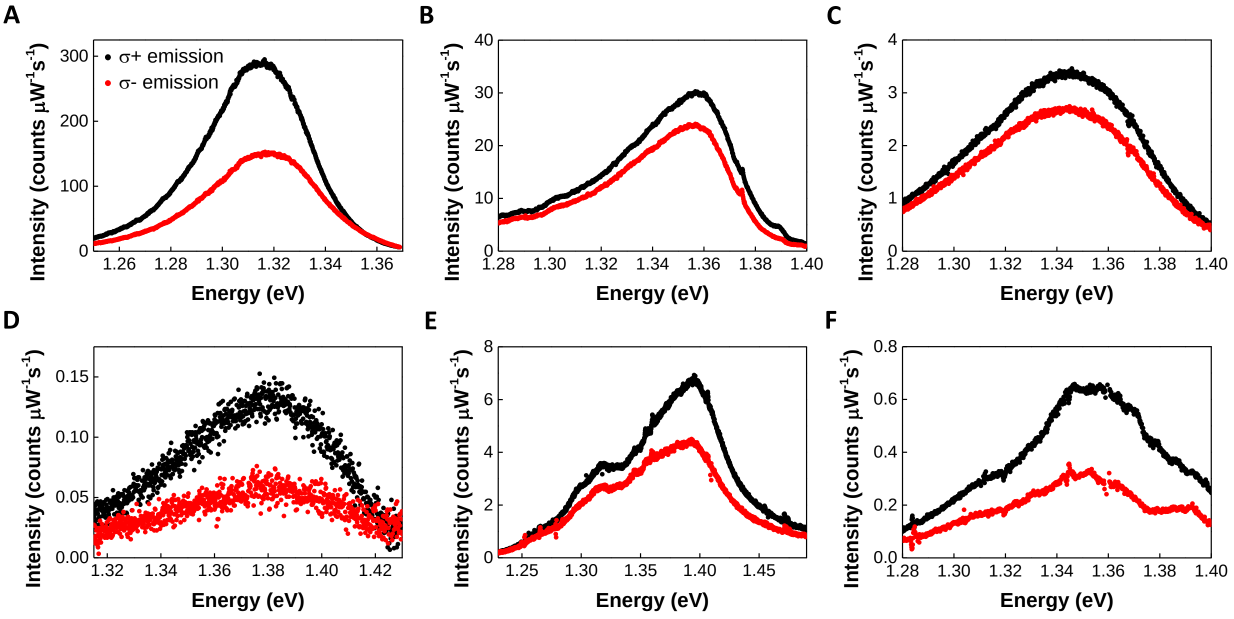

Figure B-1 | Valley-polarized interlayer excitons in supplementary heterostructures. Circular polarization-resolved interlayer exciton PL spectra from several heterostructures under σ^+ excitation. Black and red respectively denote $\sigma^+$and σ^- PL emission. The interlayer exciton PL is co-polarized with the helicity of the excitation source for all samples. (A) Device presented in the main text with WSe_2 on top of $MoSe_2$. (B-F) Inverted heterostructures ($MoSe_2$ on WSe_2) displaying similar valley polarization. All data are taken at 30 K.

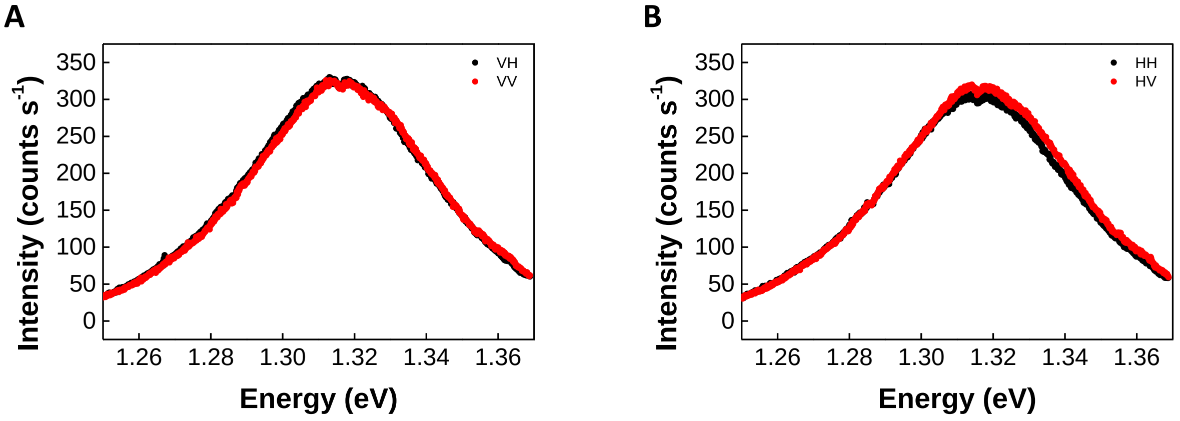

Figure B-2 | Linear polarization of interlayer excitons. Linear polarization-resolved interlayer exciton photoluminescence spectra from the device presented in the main text under **(A)** vertically polarized excitation, and **(B)** horizontally polarized excitation. Black and red respectively denote horizontal and vertical PL emission.

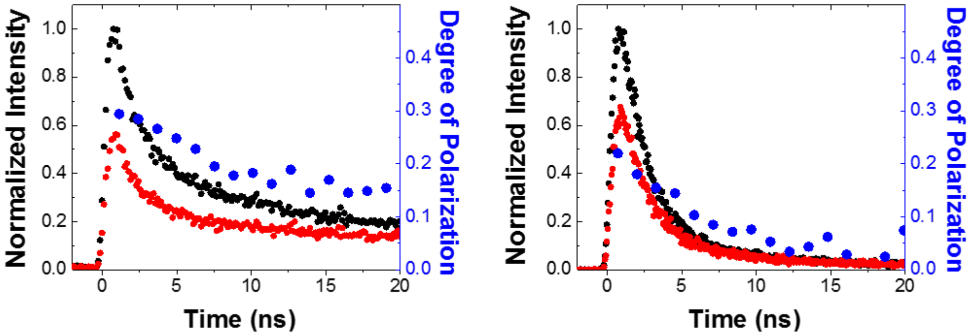

Figure B-3 | Valley lifetime in supplementary heterostructures. Time-resolved interlayer exciton PL from two supplementary heterostructures under σ^+ polarized pulsed laser excitation at 1.72 eV. Co-polarized and cross-polarized components of interlayer exciton PL are shown in black and red, respectively, and the degree of valley polarization is shown in blue. The stacking order for these devices is inverted ($MoSe_2$ on WSe_2) compared to the heterostructure in the main text.

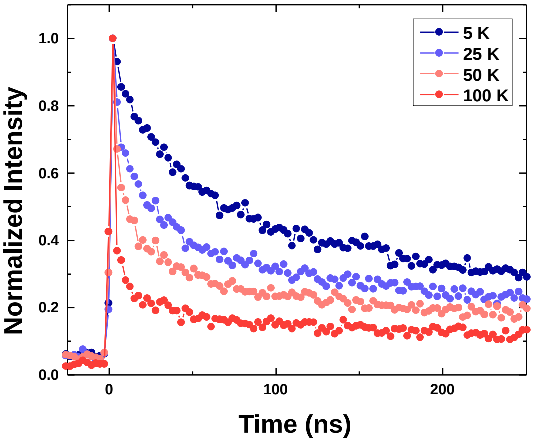

Figure B-4 | Temperature dependence of interlayer exciton lifetime. Time-resolved interlayer exciton photoluminescence as a function of temperature. The lifetime is enhanced at lower temperatures, consistent with the momentum-indirect nature of the interlayer exciton.

B.2 Optical pumping of interlayer excitons in heterostructures with AB-like stacking

Here we consider the valley polarization of interlayer excitons in heterostructures with AB-like stacking (twist angle near 60° shown in Fig. B-5A). The Brillouin zone of the bottom layer will thus be 180 degree rotation of the top layer (Fig. B-5B). In this scenario, the interlayer exciton inherits valley index $+K$ from one layer and $-K$ from the other. Consider the $X_{-,+}$ interlayer exciton as an example. Here the indices denote an electron in $-K_M$ valley of $MoSe_2$ and a hole in $+K_W$ valley of WSe_2, as shown in Fig. B-5C. The $X_{-,+}$ can radiatively recombine through three quantum pathways. The first pathway is through the virtual intermediate state of an intralayer exciton in the $+K_W$ valley: the electron in $-K_M$ conduction band hops to $+K_W$, followed by intralayer recombination in WSe_2 and subsequent emission of a σ^+ photon at the interlayer exciton energy. The second pathway is through a different virtual intermediate state, the intralayer B

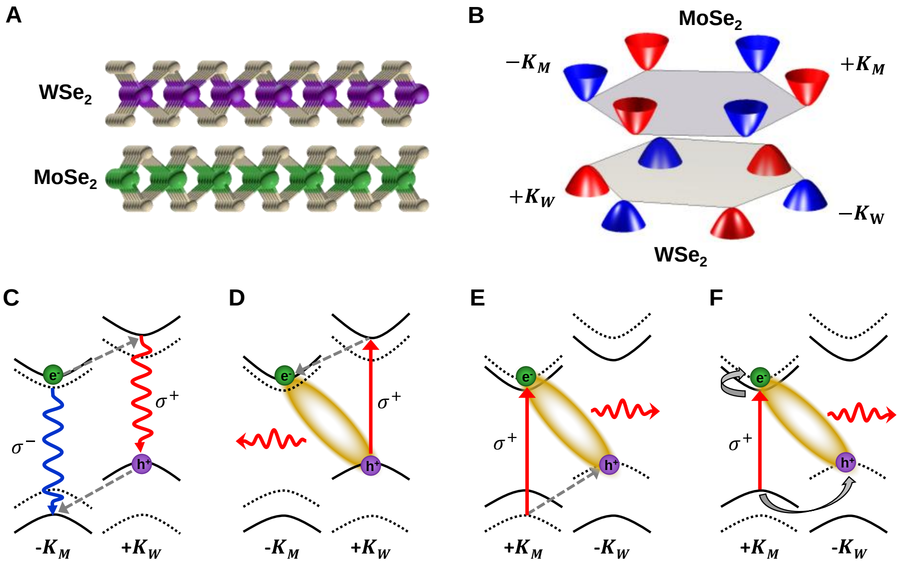

Figure B-5 | Interlayer excitons in heterostructures with AB-like stacking. **(A)** Side view of AB stacked $MoSe_2$-WSe_2 heterostructure. **(B)** Illustration of the band edges in the hexagonal Brillouin zone with twisting angle near 60°. There is 180 degree rotation of the Brillouin zones between the top and bottom layers. **(C)** Illustration of the two quantum pathways contributing to interlayer exciton recombination: the virtual interlayer hopping of an electron (hole) couples to intralayer excitons in WSe_2 ($MoSe_2$), emitting σ^+ (σ^-) polarized light. Solid (dashed) band indicate spin up (down). **(D)** Optical pumping with σ^+ polarized light excites the WSe_2 A exciton. Spin-conserving interlayer hopping of the electron (gray dashed arrow) forms the interlayer exciton with electron in $-K_M$ valley of $MoSe_2$ and hole in the $+K$ valley of WSe_2. **(E)** Optical pumping with σ^+ polarized light excites the $MoSe_2$ B exciton. Spin-conserving interlayer hopping of the hole (gray dashed arrow) forms the interlayer exciton with electron in $+K$ valley of $MoSe_2$ and hole in the $-K$ valley of WSe_2. **(F)** Optical pumping with σ^+ polarized light excites the $MoSe_2$ A exciton. Interlayer hopping requires the hole to change either its spin or valley index. The formation of interlayer exciton through this channel is expected to be inefficient.

exciton in the $-K_M$ valley of MoSe2 through the hole interlayer hopping from WSe_2 to $MoSe_2$ (Fig. B-5C), and the emitted photon is σ^- polarized. The radiative recombination can also be facilitated by the interlayer transition dipole between the electron and the hole. The interference of the three pathways leads to elliptically polarized emission of the interlayer exciton, with the helicity mainly determined by the relative strength of the electron and hole interlayer hopping rates. When the twisting angle is not exactly 60°, there are three light cones at inequivalent center-of-mass velocities, where the major axes of the elliptical polarization are 120° degree rotation of each other. When the PL is from the incoherent sum of the three light cones, the emission can be circularly polarized. Therefore, valley polarization of interlayer excitons in the AB stacking also corresponds to circularly polarized PL.

With the lack of information on the relative efficiency of the electron and hole interlayer hopping, the absolute emission helicity of a given interlayer exciton valley configuration (say, $X_{-,+}$) is undetermined. Nevertheless, a general argument leads to the expectation that the emission PL has the same helicity as the circularly polarized excitation. This is because the two recombination pathways resulting in co-polarized emission directly correspond to the two most efficient formation channels of bright interlayer excitons by optical pumping (Figs. B-5D & B-5E). Other interlayer exciton formation channels, such as that shown in Fig. B-5F, require multiple spin and valley flips of carriers, which are not favored. If the electron interlayer hopping is faster than that of the hole, the formation channel via the A exciton in WSe_2 is more efficient. In such a case, under σ^+ excitation, the interlayer exciton will be polarized in the $X_{-,+}$ valley configuration, from which the PL is expected to be σ^+ polarized. On the other hand, if the formation channels via the B exciton in $MoSe_2$ are more efficient, σ^+ excitation will generate the interlayer exciton polarized in the $X_{+,-}$ valley configuration, from which the PL is also σ^+ polarized. If there is AB-like stacking for the samples we have measured, the emitted PL is always co-polarized with the incident light, consistent with the expectations.

B.3 Exchange and dipole-dipole interactions

In this section, we discuss the exchange and dipole interactions between interlayer excitons. Following Ref 91, an interlayer exciton in its plane wave form with a center-of-mass velocity $\frac{\hbar}{M_0}\mathbf{Q}$ can be expressed in the basis of the free electron-hole Bloch states,

$$X_{\tau'\tau,\mathbf{Q}}(\mathbf{r}_\mathrm{e},\mathbf{r}_\mathrm{h}) = \sum_{\Delta\mathbf{Q}} \Phi_I(\Delta\mathbf{Q})\psi_{\tau',\frac{m_\mathrm{e}}{M_0}\mathbf{Q}+\Delta\mathbf{Q},\mathrm{c}}(\mathbf{r}_\mathrm{e})\psi^*_{\tau,-\frac{m_\mathrm{h}}{M_0}\mathbf{Q}+\Delta\mathbf{Q},\mathrm{v}}(\mathbf{r}_\mathrm{h})$$
$$\cong e^{i\mathbf{Q}\cdot\left(\frac{m_\mathrm{e}}{M_0}\mathbf{r}_\mathrm{e}+\frac{m_\mathrm{h}}{M_0}\mathbf{r}_\mathrm{h}\right)}\Phi_I(\mathbf{r}_\mathrm{e}-\mathbf{r}_\mathrm{h})u_{\tau',0,\mathrm{c}}(\mathbf{r}_\mathrm{e})u^*_{\tau,0,\mathrm{v}}(\mathbf{r}_\mathrm{h})$$

where $\mathbf{Q}$ is the kinematic momentum of the interlayer exciton and τ (τ') is the electron (hole) valley index (*27*). In this expansion, $\psi_{\tau',\Delta\mathbf{Q},\mathrm{c}}(\mathbf{r}_\mathrm{e}) = e^{i(\tau'\mathbf{K}'+\Delta\mathbf{Q})\cdot\mathbf{r}_\mathrm{e}}u_{\tau',\Delta\mathbf{Q},\mathrm{c}}(\mathbf{r}_\mathrm{e})$ $\left(\psi^*_{\tau,\Delta\mathbf{Q},\mathrm{v}}(\mathbf{r}_\mathrm{h}) = e^{-i(\tau\mathbf{K}+\Delta\mathbf{Q})\cdot\mathbf{r}_\mathrm{h}}u^*_{\tau,-\Delta\mathbf{Q},\mathrm{v}}(\mathbf{r}_\mathrm{h})\right)$ corresponds to the $\tau'\mathbf{K}'$ ($\tau\mathbf{K}$) valley electron (hole) Bloch function with *xy*-plane real space coordinate $\mathbf{r}_\mathrm{e}$ ($\mathbf{r}_\mathrm{h}$). $\Phi_I(\Delta\mathbf{Q})$ describes the electron-hole relative motion $\Delta\mathbf{Q}$ in momentum space. In the second step above we have used the envelope approximation $u_{\tau',\Delta\mathbf{Q},\mathrm{c}} \approx u_{\tau',\Delta\mathbf{Q}=0,\mathrm{c}}$ and $u_{\tau,\Delta\mathbf{Q},\mathrm{v}} \approx u_{\tau,\Delta\mathbf{Q}=0,\mathrm{v}}$, and a Fourier transform $\Phi_I(\mathbf{r}) \equiv \sum_{\Delta\mathbf{Q}}\Phi_I(\Delta\mathbf{Q})e^{i\Delta\mathbf{Q}\cdot\mathbf{r}}$. In the following discussion, we assume a twisting angle close to 0° between the two layers, so X_{++} and X_{--} are spin-allowed optical transitions, while X_{+-} and X_{-+} are spin-forbidden.

Below we consider interlayer excitons in their wave packet forms. Using the wave packet expression one can define the local density that corresponds to the exciton number in an area larger than the wave packet size. We write the real space wavefunction of such an interlayer exciton wave packet

$$X_{\tau'\tau,\mathbf{R}}(\mathbf{r}_\mathrm{e},\mathbf{r}_\mathrm{h}) \equiv \sum_{\mathbf{Q}} w_\mathbf{R}(\mathbf{Q})X_{\tau'\tau,\mathbf{Q}}(\mathbf{r}_\mathrm{e},\mathbf{r}_\mathrm{h})$$
$$\cong w\left(\frac{m_\mathrm{e}}{M_0}\mathbf{r}_\mathrm{e}+\frac{m_\mathrm{h}}{M_0}\mathbf{r}_\mathrm{h}-\mathbf{R}\right)\Phi_I(\mathbf{r}_\mathrm{e}-\mathbf{r}_\mathrm{h})u_{\tau',0,\mathrm{c}}(\mathbf{r}_\mathrm{e})u^*_{\tau,0,\mathrm{v}}(\mathbf{r}_\mathrm{h}). \qquad \text{(S1)}$$

Here $w(\mathbf{r}-\mathbf{R}) \equiv \sum_\mathbf{Q} w_\mathbf{R}(\mathbf{Q})e^{i\mathbf{Q}\cdot\mathbf{r}}$ describes a real space wave packet centered at $\mathbf{R}$ whose width W is larger than the interlayer exciton Bohr radius a_B but much smaller than the heterostructure sample size $\sqrt{A}$.

We now consider interactions between two interlayer excitons. The Coulomb interaction between two interlayer excitons is illustrated in Fig. B-6A, where the solid (dashed) double arrows denote attraction (repulsion) between an electron and a hole (two electrons or two holes). We denote the electron (hole) constituent of the n-th exciton as e_n (h_n) with real space coordinate $\mathbf{d}+\mathbf{r}_{\mathrm{e},n}$ ($\mathbf{r}_{\mathrm{h},n}$) and valley index τ_n' (τ_n), where $\mathbf{r}_{\mathrm{e},n}$ ($\mathbf{r}_{\mathrm{h},n}$) lies in the xy-plane and $\mathbf{d}\equiv d\hat{\mathbf{z}}$ corresponds to the interlayer separation (≈ 0.7 nm). The exciton-exciton interaction is

$$\hat{V}_{XX}=V(\mathbf{r}_{\mathrm{e}1}-\mathbf{r}_{\mathrm{e}2})+V(\mathbf{r}_{\mathrm{h}1}-\mathbf{r}_{\mathrm{h}2})-V(\mathbf{d}+\mathbf{r}_{\mathrm{e}1}-\mathbf{r}_{\mathrm{h}2})-V(\mathbf{d}+\mathbf{r}_{\mathrm{e}2}-\mathbf{r}_{\mathrm{h}1}),$$

with $V(\mathbf{r})$ being the real space form of the Coulomb interaction.

The matrix elements of $\hat{V}_{XX}$ in the two-exciton direct product basis $X_{\tau_1'\tau_1,\mathbf{R}_1}(\mathbf{r}_{\mathrm{e}1},\mathbf{r}_{\mathrm{h}1})\otimes X_{\tau_2'\tau_2,\mathbf{R}_2}(\mathbf{r}_{\mathrm{e}2},\mathbf{r}_{\mathrm{h}2})$ can be separated into the dipole-dipole and exchange interaction parts.

I. Dipole-dipole interaction

First, we consider the dipole-dipole (or direct Coulomb) interaction illustrated in Figure B-6B, which corresponds to an exciton-exciton scattering process $(e_1,h_1)+(e_2,h_2)\rightarrow(e_1,h_1)+(e_2,h_2)$. The direct Coulomb interaction between two interlayer excitons (in wavepacket form) located at $\mathbf{R}_1$ and $\mathbf{R}_2$ is

$$\begin{aligned}
&V_{\mathrm{dd}}(\mathbf{R}_1-\mathbf{R}_2)\\
&\equiv\left\langle X_{\tau_2'\tau_2,\mathbf{R}_2}(\mathbf{r}_{\mathrm{e}2},\mathbf{r}_{\mathrm{h}2})\middle|\left\langle X_{\tau_1'\tau_1,\mathbf{R}_1}(\mathbf{r}_{\mathrm{e}1},\mathbf{r}_{\mathrm{h}1})\middle|\hat{V}_{XX}\middle|X_{\tau_1'\tau_1,\mathbf{R}_1}(\mathbf{r}_{\mathrm{e}1},\mathbf{r}_{\mathrm{h}1})\right\rangle\middle|X_{\tau_2'\tau_2,\mathbf{R}_2}(\mathbf{r}_{\mathrm{e}2},\mathbf{r}_{\mathrm{h}2})\right\rangle\\
&=\int\left|u_{\tau_1',0,\mathrm{c}}(\mathbf{r}_{\mathrm{e}1})u^*_{\tau_1,0,\mathrm{v}}(\mathbf{r}_{\mathrm{h}1})u_{\tau_2',0,\mathrm{c}}(\mathbf{r}_{\mathrm{e}2})u^*_{\tau_2,0,\mathrm{v}}(\mathbf{r}_{\mathrm{h}2})\right|^2\\
&\times\left|w\left(\tfrac{m_\mathrm{e}}{M_0}\mathbf{r}_{\mathrm{e}1}+\tfrac{m_\mathrm{h}}{M_0}\mathbf{r}_{\mathrm{h}1}-\mathbf{R}_1\right)w\left(\tfrac{m_\mathrm{e}}{M_0}\mathbf{r}_{\mathrm{e}2}+\tfrac{m_\mathrm{h}}{M_0}\mathbf{r}_{\mathrm{h}2}-\mathbf{R}_2\right)\Phi_I(\mathbf{r}_{\mathrm{e}1}-\mathbf{r}_{\mathrm{h}1})\Phi_I(\mathbf{r}_{\mathrm{e}2}-\mathbf{r}_{\mathrm{h}2})\right|^2\\
&\times\big(V(\mathbf{r}_{\mathrm{e}1}-\mathbf{r}_{\mathrm{e}2})+V(\mathbf{r}_{\mathrm{h}1}-\mathbf{r}_{\mathrm{h}2})-V(\mathbf{d}+\mathbf{r}_{\mathrm{e}1}-\mathbf{r}_{\mathrm{h}2})-V(\mathbf{d}+\mathbf{r}_{\mathrm{e}2}-\mathbf{r}_{\mathrm{h}1})\big)\\
&\times d\mathbf{r}_{\mathrm{e}1}d\mathbf{r}_{\mathrm{e}2}d\mathbf{r}_{\mathrm{h}1}d\mathbf{r}_{\mathrm{h}2}\\
&\approx\int\left|w\left(\tfrac{m_\mathrm{e}}{M_0}\mathbf{r}_{\mathrm{e}1}+\tfrac{m_\mathrm{h}}{M_0}\mathbf{r}_{\mathrm{h}1}-\mathbf{R}_1\right)w\left(\tfrac{m_\mathrm{e}}{M_0}\mathbf{r}_{\mathrm{e}2}+\tfrac{m_\mathrm{h}}{M_0}\mathbf{r}_{\mathrm{h}2}-\mathbf{R}_2\right)\Phi_I(\mathbf{r}_{\mathrm{e}1}-\mathbf{r}_{\mathrm{h}1})\Phi_I(\mathbf{r}_{\mathrm{e}2}-\mathbf{r}_{\mathrm{h}2})\right|^2\\
&\times\big(V(\mathbf{r}_{\mathrm{e}1}-\mathbf{r}_{\mathrm{e}2})+V(\mathbf{r}_{\mathrm{h}1}-\mathbf{r}_{\mathrm{h}2})-V(\mathbf{d}+\mathbf{r}_{\mathrm{e}1}-\mathbf{r}_{\mathrm{h}2})-V(\mathbf{d}+\mathbf{r}_{\mathrm{e}2}-\mathbf{r}_{\mathrm{h}1})\big)\\
&\times d\mathbf{r}_{\mathrm{e}1}d\mathbf{r}_{\mathrm{e}2}d\mathbf{r}_{\mathrm{h}1}d\mathbf{r}_{\mathrm{h}2}. \qquad\qquad \text{(S2)}
\end{aligned}$$

Since the width of the interlayer exciton wavefunction is much larger than the interlayer exciton Bohr radius, $W>a_B\gg a$ (a is the lattice constant), $w(\mathbf{r}-\mathbf{R})$ and $\Phi_I(\mathbf{r})$ vary slowly with $\mathbf{r}$ compared to $u_{\tau,0,\mathrm{c/v}}(\mathbf{r})$. So in the third step above, we approximate $\left|u_{\tau,0,\mathrm{c/v}}(\mathbf{r})\right|^2$ by its mean value $\int\left|u_{\tau,0,\mathrm{c/v}}(\mathbf{r})\right|^2d\mathbf{r}=1$, and the periodic part of the Bloch function in the integral can be dropped.

For finite interlayer separation $\mathbf{d}$, we can expect $V(\mathbf{r}_{\mathrm{e}1}-\mathbf{r}_{\mathrm{e}2})+V(\mathbf{r}_{\mathrm{h}1}-\mathbf{r}_{\mathrm{h}2})>V(\mathbf{d}+\mathbf{r}_{\mathrm{e}1}-\mathbf{r}_{\mathrm{h}2})+V(\mathbf{d}+\mathbf{r}_{\mathrm{e}2}-\mathbf{r}_{\mathrm{h}1})$ thus $V_{\mathrm{dd}}(\mathbf{R}_1-\mathbf{R}_2)>0$ is finite, this is why we call V_{dd} the dipole-dipole interaction between two interlayer excitons. Here we emphasize that V_{dd} is independent of the valley indices of the two excitons.

II. Exchange interaction

Next, we consider the exchange interactions between two interlayer excitons with the same valley index. From the indistinguishability of Fermions, the two-exciton wavefunction should have an antisymmetrized form

$$\frac{1}{2}\Big(X_{\tau'\tau,\mathbf{R}_1}(\mathbf{r}_{\mathrm{e}1},\mathbf{r}_{\mathrm{h}1})X_{\tau'\tau,\mathbf{R}_2}(\mathbf{r}_{\mathrm{e}2},\mathbf{r}_{\mathrm{h}2})-X_{\tau'\tau,\mathbf{R}_1}(\mathbf{r}_{\mathrm{e}1},\mathbf{r}_{\mathrm{h}2})X_{\tau'\tau,\mathbf{R}_2}(\mathbf{r}_{\mathrm{e}2},\mathbf{r}_{\mathrm{h}1}) \\ -X_{\tau'\tau,\mathbf{R}_1}(\mathbf{r}_{\mathrm{e}2},\mathbf{r}_{\mathrm{h}1})X_{\tau'\tau,\mathbf{R}_2}(\mathbf{r}_{\mathrm{e}1},\mathbf{r}_{\mathrm{h}2})+X_{\tau'\tau,\mathbf{R}_1}(\mathbf{r}_{\mathrm{e}2},\mathbf{r}_{\mathrm{h}2})X_{\tau'\tau,\mathbf{R}_2}(\mathbf{r}_{\mathrm{e}1},\mathbf{r}_{\mathrm{h}1})\Big).$$

The expectation value $\hat{V}_{XX}$ under this wavefunction then contains two terms. The first term is just the dipole-dipole interaction $V_{\mathrm{dd}}(\mathbf{R}_1-\mathbf{R}_2)$ given above, while the second term is *(40-43)*:

$$\begin{aligned}
&V_{\mathrm{ex}}(\mathbf{R}_1-\mathbf{R}_2)\\
&\equiv -\big\langle X_{\tau'\tau,\mathbf{R}_2}(\mathbf{r}_{\mathrm{e}2},\mathbf{r}_{\mathrm{h}1})\big|\big\langle X_{\tau'\tau,\mathbf{R}_1}(\mathbf{r}_{\mathrm{e}1},\mathbf{r}_{\mathrm{h}2})\big|\hat{V}_{XX}\big|X_{\tau'\tau,\mathbf{R}_1}(\mathbf{r}_{\mathrm{e}1},\mathbf{r}_{\mathrm{h}1})\big\rangle\big|X_{\tau'\tau,\mathbf{R}_2}(\mathbf{r}_{\mathrm{e}2},\mathbf{r}_{\mathrm{h}2})\big\rangle\\
&\approx \int \Phi_I(\mathbf{r}_{\mathrm{e}1}-\mathbf{r}_{\mathrm{h}1})\Phi_I(\mathbf{r}_{\mathrm{e}2}-\mathbf{r}_{\mathrm{h}2})\Phi_I^*(\mathbf{r}_{\mathrm{e}1}-\mathbf{r}_{\mathrm{h}2})\Phi_I^*(\mathbf{r}_{\mathrm{e}2}-\mathbf{r}_{\mathrm{h}1})\\
&\times w^*\left(\tfrac{m_{\mathrm{e}}}{M_0}\mathbf{r}_{\mathrm{e}2}+\tfrac{m_{\mathrm{h}}}{M_0}\mathbf{r}_{\mathrm{h}1}-\mathbf{R}_2\right)w^*\left(\tfrac{m_{\mathrm{e}}}{M_0}\mathbf{r}_{\mathrm{e}1}+\tfrac{m_{\mathrm{h}}}{M_0}\mathbf{r}_{\mathrm{h}2}-\mathbf{R}_1\right)\\
&\times w\left(\tfrac{m_{\mathrm{e}}}{M_0}\mathbf{r}_{\mathrm{e}1}+\tfrac{m_{\mathrm{h}}}{M_0}\mathbf{r}_{\mathrm{h}1}-\mathbf{R}_1\right)w\left(\tfrac{m_{\mathrm{e}}}{M_0}\mathbf{r}_{\mathrm{e}2}+\tfrac{m_{\mathrm{h}}}{M_0}\mathbf{r}_{\mathrm{h}2}-\mathbf{R}_2\right)\\
&\times\big(V(\mathbf{d}+\mathbf{r}_{\mathrm{e}1}-\mathbf{r}_{\mathrm{h}2})+V(\mathbf{d}+\mathbf{r}_{\mathrm{e}2}-\mathbf{r}_{\mathrm{h}1})-V(\mathbf{r}_{\mathrm{e}1}-\mathbf{r}_{\mathrm{e}2})-V(\mathbf{r}_{\mathrm{h}1}-\mathbf{r}_{\mathrm{h}2})\big)\\
&\times d\mathbf{r}_{\mathrm{e}1}d\mathbf{r}_{\mathrm{e}2}d\mathbf{r}_{\mathrm{h}1}d\mathbf{r}_{\mathrm{h}2}. \qquad\qquad \text{(S3)}
\end{aligned}$$

This corresponds to the exciton-exciton scattering process $(e_1,h_1)+(e_2,h_2)\rightarrow(e_1,h_2)+(e_2,h_1)$, where either the electron or the hole constituent are exchanged between the two excitons. For two excitons with the same valley indices ($\tau_1'=\tau_2'=\tau'$ and $\tau_1=\tau_2=\tau$), this exchange process corresponds to a diagonal energy, i.e. an interaction energy between the excitons (Figure B-6C). Importantly, we note that V_{ex} is present only between two excitons with the same valley index. This is in contrast to the dipole-dipole interaction V_{dd}, which is valley independent.

The exchange of electrons or holes can happen only when the two interlayer excitons are in contact with each other, i.e. V_{ex} is only appreciable when the two wave packets have substantial overlap. With a large enough separation between the wave packets $(|\mathbf{R}_1 - \mathbf{R}_2| \gg W)$, the exchange interaction decays as $V_{\mathrm{ex}} \sim \left(w^* \left(\frac{m_{\mathrm{h}}}{M_0} (\mathbf{R}_1 - \mathbf{R}_2) \right) \right)^2 \left(V(\mathbf{d} + \mathbf{R}_1 - \mathbf{R}_2) - V(\mathbf{R}_1 - \mathbf{R}_2) \right)$ which is exponentially small.

We note that the Coulomb exchange interaction also results in another process, as shown in Figure B-6D: when the two bright interlayer excitons are from different valleys (X_{++} and X_{--}), they will be scattered to become a pair of dark excitons X_{+-} and X_{-+}. This can be phenomenologically described as population decay of the bright excitons and has negligible effect on the spatial pattern of polarization.

III. Density-dependent energy shift from the exciton-exciton interaction

Here we use the mean field approximation and only consider the diagonal terms for the exciton-exciton interaction. For a heterostructure sample with spatially inhomogeneous X_{++} density $N_+(\mathbf{r})$ and X_{--} density $N_-(\mathbf{r})$, an X_{++} (X_{--}) exciton wave packet at position $\mathbf{R}$ feels a mean potential from both the dipole-dipole and exchange interactions,

$$\begin{aligned} \Delta E_{\pm}(\mathbf{R}) &= \int V_{\mathrm{ex}}(\mathbf{R}-\mathbf{r}) N_{\pm}(\mathbf{r}) d\mathbf{r} + \int V_{\mathrm{dd}}(\mathbf{R}-\mathbf{r}) \left(N_+(\mathbf{r}) + N_-(\mathbf{r}) \right) d\mathbf{r} \\ &= \left(\frac{\int V_{\mathrm{ex}}(\mathbf{R}-\mathbf{r}) N_{\pm}(\mathbf{r}) d\mathbf{r}}{\int V_{\mathrm{ex}}(\mathbf{R}-\mathbf{r}) d\mathbf{r}} \right) \int V_{\mathrm{ex}}(\mathbf{R}-\mathbf{r}) d\mathbf{r} + \left(\frac{\int V_{\mathrm{dd}}(\mathbf{R}-\mathbf{r}) \left(N_+(\mathbf{r}) + N_-(\mathbf{r}) \right) d\mathbf{r}}{\int V_{\mathrm{dd}}(\mathbf{R}-\mathbf{r}) d\mathbf{r}} \right) \int V_{\mathrm{dd}}(\mathbf{R}-\mathbf{r}) d\mathbf{r} \\ &\approx N_{\pm}(\mathbf{R}) \bar{V}_{\mathrm{ex}} + \left(N_+(\mathbf{R}) + N_-(\mathbf{R}) \right) \bar{V}_{\mathrm{dd}}. \qquad \text{(S4)} \end{aligned}$$

In the last step above, we have used the fact that in the experiment $N_{\pm}(\mathbf{R})$ varies rather slowly with a typical length scale of ~μm, and V_{ex} has a contact nature, so $\frac{\int V_{\mathrm{ex}}(\mathbf{R}-\mathbf{r}) N_{\pm}(\mathbf{r}) d\mathbf{r}}{\int V_{\mathrm{ex}}(\mathbf{R}-\mathbf{r}) d\mathbf{r}} \approx \frac{\int V_{\mathrm{dd}}(\mathbf{R}-\mathbf{r}) N_{\pm}(\mathbf{r}) d\mathbf{r}}{\int V_{\mathrm{dd}}(\mathbf{R}-\mathbf{r}) d\mathbf{r}} \approx N_{\pm}(\mathbf{R})$. $\bar{V}_{\mathrm{ex/dd}} \equiv \int V_{\mathrm{ex/dd}}(\mathbf{R}-\mathbf{r}) d\mathbf{r}$ are two constants independent on $\mathbf{R}$ which will be estimated in the next subsection.

Eq. (S4) above is the central result of this section, which makes clear that for sufficiently dense populations of interlayer excitons, the potential landscape depends on both dipole-dipole and exchange interactions. Since the exchange interactions are only present between excitons in the same valley, in the presence of valley polarization ($N_+(\mathbf{r})$ differs from $N_-(\mathbf{r})$), the spatially dependent potential $\Delta E(\mathbf{R})$ due to the exciton-exciton interaction is different for X_{--} and X_{++}, which then corresponds to a valley-dependent driving force for the exciton expansion.

IV. Qualitative estimation of the dipole-dipole and exchange interaction

We note that $\bar{V}_{\mathrm{ex/dd}} \equiv \int V_{\mathrm{ex/dd}}(\mathbf{R}-\mathbf{r})d\mathbf{r}$ corresponds to the interaction between two excitons in plane wave forms. For spatially indirect exciton in coupled quantum wells with homogeneous ε, references (*40-43)* have already calculated such $\bar{V}_{\mathrm{ex/dd}}$ using the hydrogen model with 1/r Coulomb law ($V(\mathbf{r}) = e^2/\varepsilon r$). For a qualitative estimation below, we first directly quote their results, then qualitatively discuss the difference between the indirect exciton in coupled quantum wells and the interlayer exciton in transition metal dichalcogenide heterobilayers.

We note that in the hydrogen model the dipole-dipole interaction has the form $V_{\mathrm{dd}}(\mathbf{R}) \propto \frac{1}{R} - \frac{1}{\sqrt{R^2+d^2}}$, where $\frac{1}{R}$ comes from the e-e and h-h repulsion while $\frac{-1}{\sqrt{R^2+d^2}}$ is from the e-h attraction. When $R \gg d$, $V_{\mathrm{dd}}(\mathbf{R}) \propto R^{-3}$ becomes the conventional form for the dipole-dipole interaction. The integral is evaluated as $\bar{V}_{\mathrm{dd}} \equiv \int V_{\mathrm{dd}}(\mathbf{R})d\mathbf{R} = \frac{e^2}{\varepsilon}\int\left(\frac{1}{R} - \frac{1}{\sqrt{R^2+d^2}}\right)RdR = de^2/\varepsilon$, which increases linearly with d.

The exchange interaction has a more complicated form and should be evaluated numerically, so we only give an approximate result here: $\bar{V}_{\mathrm{ex}} \approx \left(1 - \frac{d}{0.66a_0}\right)6a_0e^2/\varepsilon$. It also has an approximately linear dependence on d, where a_0 is the 2D hydrogen model Bohr radius of the intralayer exciton. For small d, $\bar{V}_{\mathrm{ex}}$ is positive which means the exchange interaction is repulsive for two excitons in the same valley. $\bar{V}_{\mathrm{ex}}$ decreases about linearly with d and crosses zero at $d \approx 0.66a_0$.

In the layered structure of transition metal dichalcogenides, however, the dielectric constant ε is anisotropic (ε in the in-plane direction is much larger than that of the out-of-plane direction), so a simple hydrogen model with 1/r Coulomb law is not accurate (*44*). The exact forms of $\bar{V}_{\mathrm{ex/dd}}$ should be more complicated, but nevertheless we can still analyze how they deviate from the above hydrogen model results. Since ε in the out-of-plane direction is small, $V(\mathbf{d}+\mathbf{r}_{\mathrm{e}}-\mathbf{r}_{\mathrm{h}})$ should have a slower decay with d compared to the hydrogen model with isotropic ε. This has opposite effects on $\bar{V}_{\mathrm{dd}}$ and $\bar{V}_{\mathrm{ex}}$. As shown in the Eq. (S2), in $\bar{V}_{\mathrm{dd}}$, the electron-hole interaction $V(\mathbf{d}+\mathbf{r}_{\mathrm{e}}-\mathbf{r}_{\mathrm{h}})$ partially cancels the electron-electron and hole-hole interaction energy. On the other hand, for small d, $\bar{V}_{\text{ex}} > 0$, the repulsive exchange interaction $\bar{V}_{\text{ex}}$ mainly originates from the electron-hole interaction $V(\mathbf{d} + \mathbf{r}_{\text{e}} - \mathbf{r}_{\text{h}})$, as shown in Eq. (S3). Therefore, at given interlayer separation d, the hydrogen model overestimates $\bar{V}_{\text{dd}}$ and underestimates $\bar{V}_{\text{ex}}$.

Since the layer separation d (~0.7 nm) is small compared to the Bohr radius of the intralayer exciton, a_0 (~ $1 - 3$ nm), it only slightly reduces the direct Coulomb interaction between electron and hole that forms the interlayer exciton. For an order of magnitude estimation of V_{ex} and V_{dd}, we assume that the Bohr radius and binding energy of interlayer exciton have the same order of magnitudes as the intralayer excitons in monolayers. From this, we can do an order of magnitude estimation of $\bar{V}_{\text{ex}}$ and $\bar{V}_{\text{dd}}$, which results in $\bar{V}_{\text{ex}} \sim a_0 e^2/\varepsilon \sim a_0^2 E_b > 0$, and $0 < \bar{V}_{\text{dd}} \lesssim de^2/\varepsilon \sim d a_0 E_b$, where $E_b \sim e^2/\varepsilon a_0 \sim 0.5$ eV is the intralayer exciton binding energy. Therefore, we expect that the exchange and dipole-dipole interactions are both repulsive.

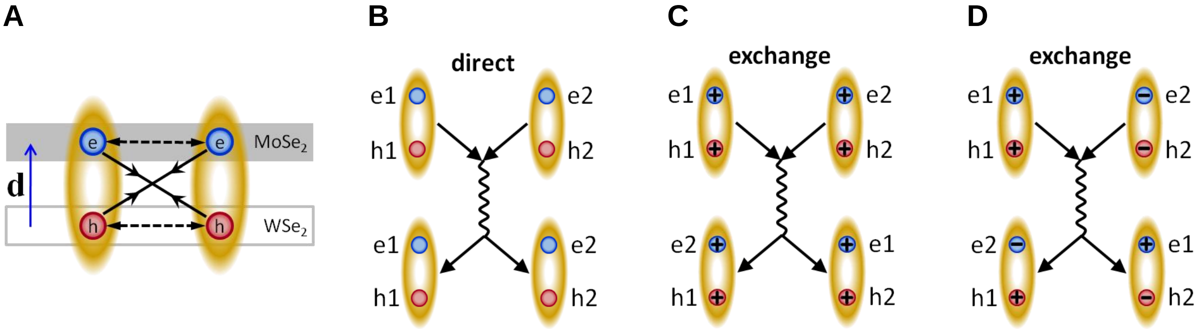

Figure B-6 | Interactions between spin-valley polarized interlayer excitons. (**A**) The interaction between two interlayer excitons. The solid (dashed) double arrows denote the Coulomb attraction (repulsion) between an electron and a hole (two electrons or two holes). (**B**) The diagram of the valley-independent direct interaction between two excitons. (**C**) The exchange interaction between two excitons with the same valley indices. (**D**) The exchange interaction between two excitons with different valley indices. Here, ± denotes $\pm K$ valleys.

B.4 Exciton density under pulsed excitation

Here we estimate an upper bound for the exciton density under pulsed excitation with photon energy of 1.72 eV at 40 μW average power. The optical absorption of the heterostructure is taken as the combined absorption of the individual layers of MoSe$_2$ and WSe$_2$, which are approximately 5% and 10%, respectively (*45*), and we adjust for the observed saturation in PL intensity (Fig. B-7). Additionally, we assume the intralayer excitons relax to form interlayer excitons (X_I) with unit efficiency. Under pulsed excitation, $\sim 10^5$ photons are absorbed per pulse, forming the same number of interlayer excitons. Due to the short duration of the pulse compared to the exciton lifetime, we normalize the exciton population over the Gaussian profile of the excitation beam (700 nm FWHM), and the peak density of interlayer excitons occurs at the center of the excitation. Immediately after a pulse the interlayer exciton density has a maximum value of $\sim 0.2\, X_I \cdot \mathrm{nm}^{-2}$. Based on the assumptions, this is the upper bound for the interlayer exciton density under our experimental condition.

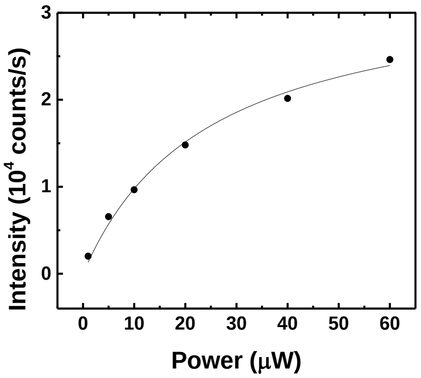

Figure B-7 | Power dependence of interlayer exciton PL. Power dependence of the co-polarized component of interlayer exciton PL intensity (under σ^+ pulsed excitation at 1.72 eV).

B.5 Interlayer exciton drift-diffusion model

Consider a heterostructure system with spatial- and time-dependent X_{++} density $N_+(\mathbf{r},t)$ and X_{--} density $N_-(\mathbf{r},t)$. As described above, the X_{++} exciton at $\mathbf{r}$ feels a mean potential from both the valley-dependent exchange and valley-independent dipole-dipole interactions, $\bar{V}_{\mathrm{ex}}N_+(\mathbf{r},t) + \bar{V}_{\mathrm{dd}}\big(N_+(\mathbf{r},t) + N_-(\mathbf{r},t)\big)$. Similarly, the X_{--} exciton at $\mathbf{r}$ feels a mean potential $\bar{V}_{\mathrm{ex}}N_-(\mathbf{r},t) + \bar{V}_{\mathrm{dd}}\big(N_+(\mathbf{r},t) + N_-(\mathbf{r},t)\big)$. The gradient in the density-dependent potential leads to a force on the interlayer excitons, imparting them with a drift velocity $V_{\pm,\mathrm{drift}} = -\alpha_0\nabla N_\pm - \beta_0\nabla N_\mp$. Here the parameters $\alpha_0 \equiv \frac{\mu}{e}(\bar{V}_{\mathrm{ex}} + \bar{V}_{\mathrm{dd}}) \sim \frac{\mu}{e}(a_0 + d)a_0E_b$ and $\beta_0 \equiv \frac{\mu}{e}\bar{V}_{\mathrm{dd}} \lesssim \frac{\mu}{e}da_0E_b$ (see supplementary discussion 2.11). A mobility value of $\mu \sim 50\ \mathrm{cm}^2\cdot\mathrm{V}^{-1}\cdot\mathrm{s}^{-1}$ corresponds to $\alpha_0 \sim 10^{-5}\ \mu\mathrm{m}^4\cdot\mathrm{ns}^{-1}$. For β_0 currently we only know $\beta_0 < \alpha_0$, but considering the ambiguity of a_0 value and the non-hydrogen model correction discussed in section 2.11, there could be $\bar{V}_{\mathrm{ex}} \gg \bar{V}_{\mathrm{dd}}$ and $\alpha_0 \gg \beta_0$. Accordingly, we choose $\alpha_0 = 5\beta_0$ for simulation purposes.

The expansion of the two-valley interlayer excitons under laser generation profile $G_\pm(\mathbf{r},t)$ is described by the drift-diffusion model:

$$\frac{\partial N_+}{\partial t} = G_+(\mathbf{r},t) + D\nabla^2 N_+ + \nabla\cdot\big((\alpha_0\nabla N_+ + \beta_0\nabla N_-)N_+\big) - \frac{N_+}{\tau} - \frac{N_+ - N_-}{\tau_v},$$

$$\frac{\partial N_-}{\partial t} = G_-(\mathbf{r},t) + D\nabla^2 N_- + \nabla\cdot\big((\alpha_0\nabla N_- + \beta_0\nabla N_+)N_-\big) - \frac{N_-}{\tau} + \frac{N_+ - N_-}{\tau_v}.$$

Here, the second term on the right hand side corresponds to the density dependent diffusion of the interlayer excitons, and $D = \mu k_B T/e \sim 0.01\ \mu\mathrm{m}^2 \cdot \mathrm{ns}^{-1} = 0.1\ \mathrm{cm}^2 \cdot \mathrm{s}^{-1}$ ($T \sim 30$ K) is the diffusion constant. The third term is of primary interest, as it captures the exchange and dipole-dipole interaction driven drift of the valley interlayer excitons $X_{\pm\pm}$, manifesting the excitonic drift current $-(\alpha_0 \nabla N_\pm + \beta_0 \nabla N_\mp) N_\pm$. The final two terms capture radiative decay and the valley relaxation, with τ the exciton life time, and τ_v the valley polarization lifetime.

We note that processes such as biexciton formation, Auger scattering, and the population relaxation between bright and dark excitons are not included in this model, which can be oversimplified for a quantitative comparison with experiment. Nevertheless, the main qualitative features observed (i.e. the ring-like polarization pattern) can be well-reproduced using reasonable parameters, where the valley-dependent exchange and the valley-independent dipole-dipole repulsive interactions are the main causes.

For the pulsed laser with a very short duration, we write the exciton density distribution just after the pulse as $N_+(\mathbf{r}, t = 0) = N_0 e^{-r^2/a^2}$and $N_-(\mathbf{r}, t = 0) = \delta \cdot N_0 e^{-r^2/a^2}$, with N_0 the peak exciton density and a the laser half-width. Let the dimensionless variable $\rho_\pm(\mathbf{r}, t) \equiv N_\pm(\mathbf{r}, t)/N_0$, then the evolution is governed by

$$\frac{\partial \rho_+}{\partial t} = D\nabla^2 \rho_+ + \nabla \cdot \big((\alpha \nabla \rho_+ + \beta \nabla \rho_-)\rho_+\big) - \frac{\rho_+}{\tau} - \frac{\rho_+ - \rho_-}{\tau_v},$$

$$\frac{\partial \rho_-}{\partial t} = D\nabla^2 \rho_- + \nabla \cdot \big((\alpha \nabla \rho_- + \beta \nabla \rho_+)\rho_-\big) - \frac{\rho_-}{\tau} + \frac{\rho_+ - \rho_-}{\tau_v}.$$

In the above we have written $\alpha \equiv N_0 \alpha_0$ and $\beta \equiv N_0 \beta_0$. Under a peak density $N_0 \sim 10^{12} - 10^{13}\ \mathrm{cm}^{-2}$, $\alpha \sim 0.1 - 1\ \mu\mathrm{m}^2 \cdot \mathrm{ns}^{-1}$. Simulation results are presented in the following, section.

B.6 Drift-diffusion model simulation results

Here we present simulation results obtained from the drift-diffusion model. Figure B-8 shows the results using the model parameters listed in Table B-1 and exciton densities N_0 =[0.0012, 0.005, 0.009, 0.014, 0.020, 0.023] nm^{-2}. These values are the estimated exciton densities corresponding to excitation powers of 1-60μW. The simple model captures the qualitative features from the experiment, namely the evolution of an expanding ring pattern under increasing excitation powers.

$\boldsymbol{a}$ (nm)	$\boldsymbol{\tau}$ (ns)	$\boldsymbol{\tau_v}$ (ns)	$\boldsymbol{\alpha_0}$ ($10^{-6}\mu\mathrm{m}^4 \cdot \mathrm{ns}^{-1}$)	$\boldsymbol{\beta_0}$ ($10^{-6}\ \mu\mathrm{m}^4 \cdot \mathrm{ns}^{-1}$)	$\boldsymbol{D}$ ($\mu\mathrm{m}^2 \cdot \mathrm{ns}^{-1}$)	$\boldsymbol{\delta}$
420	10	40	10	2	0.005	0.2

Table B-1: Drift-diffusion model parameters for pulsed excitation.

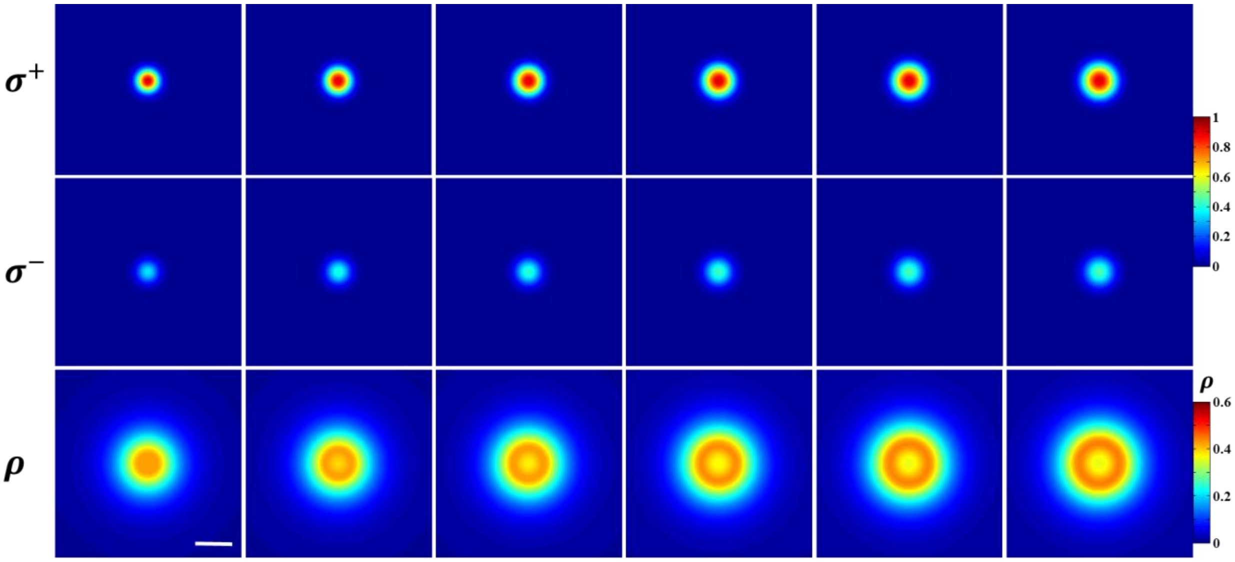

Figure B-8 | Simulated interlayer exciton valley drift-diffusion. Simulated spatial maps of valley polarization under σ^+ pulsed laser excitation for exciton densities corresponding to excitation powers of 1-60 μW. At each power, the spatial profile of co- and cross-polarized interlayer exciton density is shown in the top and middle panels (normalized to the peak co-polarized density), respectively, and the degree of valley polarization is shown in the bottom. The spatial pattern of valley polarization displays the evolution of a ring with increasing diameter under higher excitation power. $P_0 = 1\ \mu W$ and the scale bar is 2 μm.

Appendix C: Supporting Materials for Chapter 8

C.1 Supplementary figures

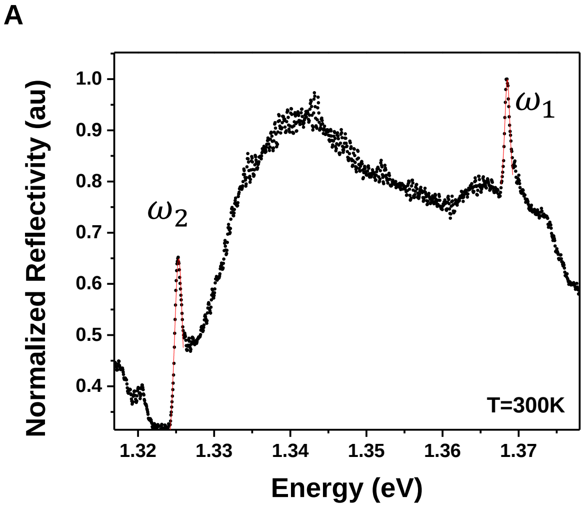

Figure C-1 | Characterization of the photonic crystal cavity modes. A The cross-linearly polarized broad band reflectivity from the linear 3 hole defect cavity in the GaP photonic crystal, at room temperature. The incident light was linearly polarized at $\pi/4$ rotation to the axes of the photonic crystal, i.e along the V+H direction. The two cavity modes (ω_1 and ω_2) are well fit by single Lorentzian functions (red solid lines). The extracted quality factors are $Q_1 = 1370 \pm 140$ and $Q_2 = 780 \pm 50$.

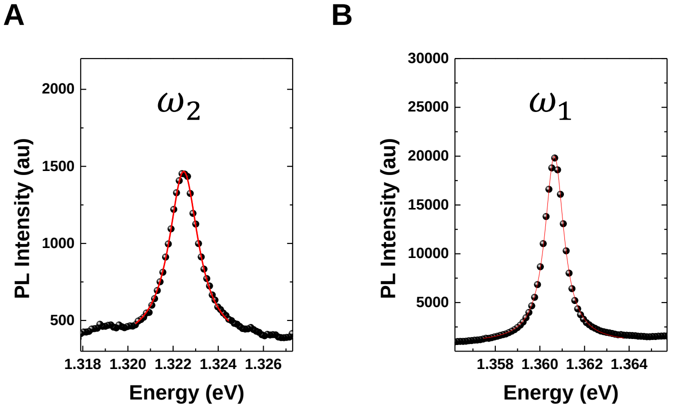

Figure C-2 | Characterization of the PL peaks ON the photonic crystal cavity. A The low energy (ω_2) and **B** high energy (ω_1) resonances appearing in the interlayer exciton photoluminescence (PL) ON the photonic crystal cavity at low temperature (T=5K) are well fit by single Lorentzian functions (red solid lines). The extracted quality factors are $Q_1 = 1320 \pm 13$ and $Q_2 = 830 \pm 10$, which correspond well with the quality factors of the photonic crystal cavity modes identified by optical reflectivity at room temperature.

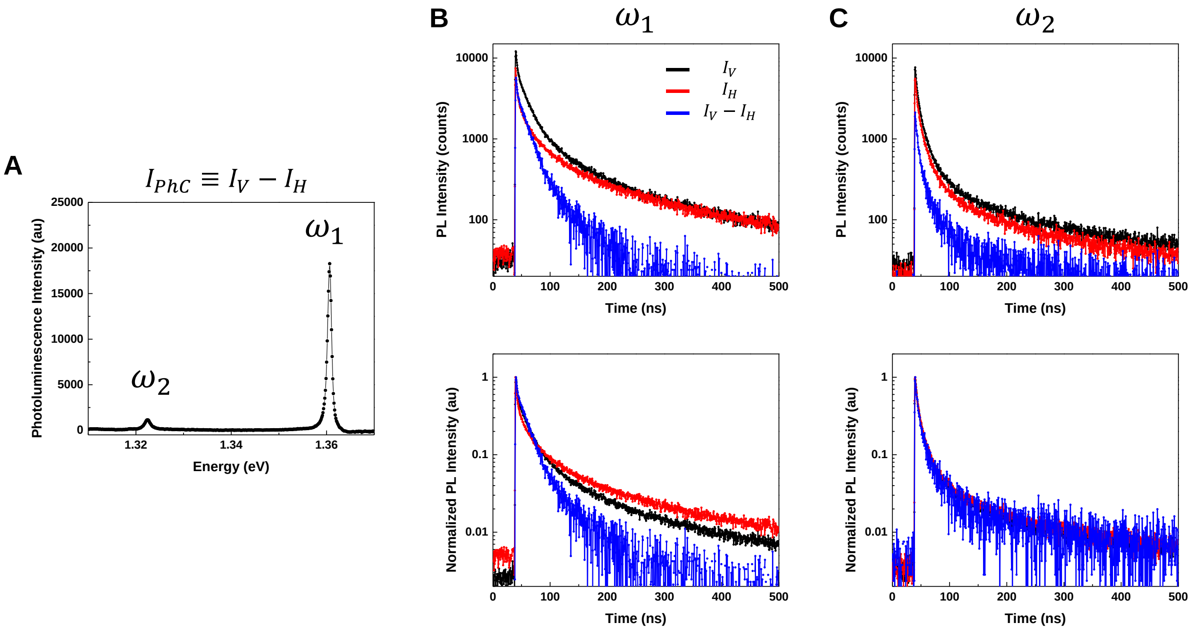

Figure C-3 | Dynamics of the cavity-enhanced PL. A Time-integrated spectrum of the cavity-enhanced ($I_{PhC} \equiv I_V - I_H$) photoluminescence (PL) from interlayer excitons (IXs) coupled to the photonic crystal (PhC) cavity modes ω_1 and ω_2. **B** Time resolved PL from IXs coupled to the ω_1 PhC cavity mode with V polarization (black), H polarization (red), and the cavity-enhanced PL (blue). **C** Time resolved PL from IXs coupled to the ω_2 PhC cavity mode with V polarization (black), H polarization (red), and the cavity-enhanced PL (blue). Top row is the measured histogram of PL intensity, while the bottom row is the normalized PL intensity.

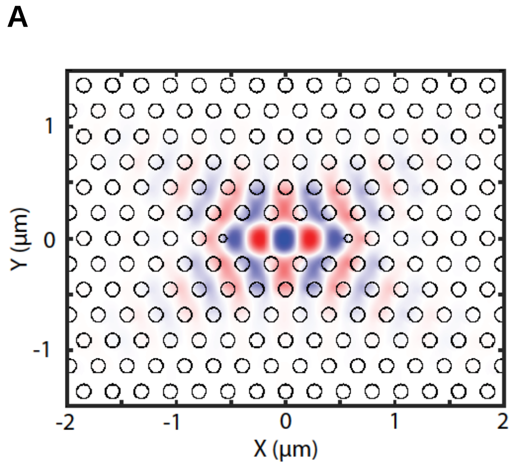

Figure C-4 | Photonic crystal cavity field profile. A Simulation of the cavity field profile. The red and blue are the magnitude of the Electric field along the x direction. The electric field component in the out-of-plane direction is negligible.

C.2 Discussion of cavity-enhanced PL dynamics

The population lifetime of the interlayer exciton PL was probed using time-correlated single photon counting (TCSPC) techniques. The time resolved decay of I_{H} and I_{V} were recorded in separate measurements, allowing for the extraction of the dynamic response of $I_{PhC} \equiv I_V - I_H$. The time-integrated spectra of I_{H} and I_{V} under the pulsed excitation are shown in Figure C-3A. We note that the cavity resonances have shifted slightly, likely due to thermal cycling between these and previous measurements. The dynamics of I_{V} and I_{H} in resonance with ω_1 are presented in Figure C-3B, which displays a clear difference between I_{V} (black) and I_{H} (red) over the first 200ns, after which, the cavity-enhanced PL (I_{PhC}, shown in blue) vanishes. Figure C-3C shows the results of these measurements for the PL in resonance with ω_2.

A typical method for determining the Purcell enhancement in exciton-cavity coupled systems is through direct comparison of the PL decay rates for samples with and without the cavity. Sample inhomogeneity precludes such measurements in the present case. Furthermore, the observed population decay of the interlayer exciton PL is not indicative of the underlying spontaneous emission rate. The measured population decay dynamics includes the effects of non-radiative relaxation to long-lived and dark exciton states, which obfuscates the contribution from relatively short timescale effects, such as the spontaneous emission rate. A separate factor that prevents Purcell effect quantification is the anomalous dispersion of the interlayer exciton. The finite lattice mismatch and relative rotation of the $MoSe_2$ and WSe_2 crystals causes the bright interlayer excitons to reside at finite momentum, so cold interlayer excitons may only couple to light through higher order processes that satisfy the momentum conservation requirements (e.g. scattering by phonon or impurity). Quantitatively, these processes are not yet understood and presently lack sufficient investigations.

Considering the complicated radiative decay pathways of the interlayer exciton, it is not surprising that the measured PL decays are generally not well fit by simple exponentials. However, the decay of I_{PhC}, shown in Figure C-3B, is well fit by a triple exponential fit, with decay constants of approximately 1.8, 20, and 93 ns. The requirements for the I_{PhC} emission are that the interlayer exciton has energy degeneracy with the cavity mode, in-plane optical dipole moment with projection along the V axis, and must conserve momentum. On short timescales, the interlayer excitons formed following interlayer charge transfer have excess energy (due to the significant band offsets) which allows them to sample a large region of momentum space. The fast decay time therefore may correspond to the decay of the interlayer exciton already within the light cone. The second decay time may correspond to the scattering of dark interlayer exciton into the finite momentum light cone. This leaves the long component of the decay, which may be attributed to cold excitons outside of the cavity, which have long lifetime due to their weak light coupling through higher order processes. This is a consequence of the beamspot size being larger than the cavity and the relatively fast depletion of IXs within spatial proximity of the cavity.

Appendix D: Supporting Materials for Chapter 9

D.1 Interlayer exciton g-factors

As discussed in the main text (Figs. D-4a, b), the Zeeman shift of the conduction or valence band edges has three contributions: spin ($\Delta_s = 2s_z\mu_B B$), atomic orbital ($\Delta_a = l_i\mu_B B$), and a valley contribution ($\Delta_v = \tau\alpha_i\mu_B B$) from the Berry phase effect. Here, $\tau = \pm 1$ is valley index, $s_z = \pm 1/2$ is electron spin index, μ_B is Bohr magneton. $\alpha_c = m_0/m_e^*$ and $\alpha_v = m_0/m_h^*$ are the valley g-factors for the conduction and valence bands, respectively, according to a simplified 2-band **k**.**p** description of the band edges[1] with m_e^* (m_h^*) the electron (hole) effective mass and m_0 the free electron mass. The two spin-split conduction bands have close effective masses, so we expect their α_c values to be about the same. $l_c = 0$ and $l_v = 2\tau$ are the magnetic quantum number for the atomic orbitals at the conduction and valence band edges.

For spin-conserved optical transitions, the electron and hole spin contributions to the interlayer exciton Zeeman shift cancel with each other, and only Δ_a and Δ_v are important. For near 0° stacking, the bright interlayer exciton has two configurations with valley pairing $(\tau_c, \tau_v) = (+,+)$ and $(-,-)$, whose Zeeman shifts are $-(2+\alpha_v-\alpha_c)\mu_B B$ and $(2+\alpha_v-\alpha_c)\mu_B B$, respectively. For near 60° or 21.8° stacking, the bright interlayer exciton has two configurations with the valley pairing $(\tau_c, \tau_v) = (-,+)$ and $(+,-)$, whose Zeeman shifts are $-(2+\alpha_v+\alpha_c)\mu_B B$ and $(2+\alpha_v+\alpha_c)\mu_B B$, respectively. From the measured exciton g-factors, we have

$$2|2+\alpha_v-\alpha_c| \approx 6.7,$$
$$2|2+\alpha_v+\alpha_c| \approx 15.9,$$

which lead to $\alpha_v \approx 3.65$ in WSe_2 and $\alpha_c \approx 2.3$ in $MoSe_2$.

The sign of the g-factor depends on how the Zeeman splitting is defined. If the Zeeman splitting is defined as the energy of the $(\tau_c,+)$ interlayer exciton minus that of $(-\tau_c,-)$, i.e. according to the hole valley index, then the obtained g-factors should always be negative, i.e., given by $-2(2+\alpha_v-\alpha_c)$ or $-2(2+\alpha_v+\alpha_c)$. However, in the experiments, our observable to distinguish the time-reversal pair of valley configurations is the PL polarization only, so the Zeeman splitting is defined here as the σ^+ PL peak energy minus σ^- PL peak energy. The valley optical selection rule, namely whether $(\tau_c, +)$ emits σ^- or σ^+ photon, then determines the sign of the g-factor.

As pointed out in earlier works[2–5], the circularly polarized valley optical selection rules for interlayer excitons depend on the interlayer registry and hence the location in a moiré supercell. Taking the $(+,+)$ interlayer exciton in a near 0° moiré pattern as an example, it emits a σ^+ (σ^-) photon at the $\boldsymbol{A}$ ($\boldsymbol{B}$) trapping sites of the moiré potential which has the interlayer registry R_h^h (R_h^X). Here, R_h^μ denotes a 0° lattice-matched stacking, with the μ site of the electron layer vertically aligned with the hexagon center (h) of the hole layer. Interlayer excitons trapped at $\boldsymbol{A}$ and $\boldsymbol{B}$ sites then have g-factors with minus and plus signs, respectively.

For the sample with 57° (2°) twist angle, our measured g-factor of -15.9 (+6.7) implies that the PL emission is from interlayer excitons localized at $\boldsymbol{A}$ ($\boldsymbol{B}$) trapping site of the moiré supercell. The different signs of the g-factors are also consistent with the co-circular PL polarization for 57° and 20° samples and cross-circular polarization for the 2° sample. For example, when exciting at the monolayer exciton resonance in WSe_2 with a σ^+ laser, most of the excited holes will reside in the K valley. The majority interlayer exciton species is then the $(+,+)$ valley pairing in the 2° sample and $(-,+)$ valley pairing in 57° and 20° samples. At low temperature, the valley-polarized interlayer excitons will relax to the local energy minima, that is, $\boldsymbol{A}$ trapping sites in 57° and 20° samples ($\boldsymbol{B}$ sites in 2° sample), which emit σ^+ (σ^-) circularly polarized PL, i.e. co-polarized (cross-polarized) with the excitation laser, consistent with the experiment.

In the above analysis, we considered only the excitons of the spin-conserved optical transitions, also known as the spin-singlet excitons. In samples with near 0° twist angle, we expect the PL emission is always from the spin-singlet interlayer exciton that is bright and has the lowest energy. However, in samples with near 60° or 21.8° twist angles, the lowest energy interlayer excitons have the spin-triplet configuration due to the $MoSe_2$ conduction band spin alignment. In heterobilayers, despite its spin-flip nature, the optical dipole of the spin-triplet exciton can be comparable to that of the spin-singlet one[5]. It is therefore possible that the PL emission from these samples arise from the spin-flip optical transitions of the spin-triplet exciton. In such case, the spin contribution to the exciton Zeeman shift are finite, and the total shifts become $-(4 + \alpha_v + \alpha_c)\mu_B B$ and $(4 + \alpha_v + \alpha_c)\mu_B B$ respectively for $(\tau_c, \tau_v) = (-,+)$ and $(+,-)$. The measured g-factor then gives us the equation: $2|4+\alpha_v+\alpha_c| \approx 15.9$. Combined with $2|2+\alpha_v-\alpha_c| \approx 6.7$ from the 0° samples, these yield $\alpha_v \approx 2.65$ in WSe_2 and $\alpha_c \approx 1.3$ in $MoSe_2$. The spin-triplet interlayer excitons also have circularly polarized valley optical selection rules at the moiré trapping sites as dictated by the rotational symmetry[5], and our previous discussion about g-factor signs still applies.

D.2 Heterobilayer moiré pattern for a twist angle close to 21.8°

For two transition metal dichalcogenide layers with the same lattice constant a, a twist angle of 21.8° corresponds to a commensurate pattern with the smallest supercell size $(\sqrt{7}a \times \sqrt{7}a)$. Like the 0° or 60° lattice-matched case, here the commensurate 21.8° bilayer also has an interlayer translation degree of freedom, which defines the different stacking configurations. In Figs. D-8a-c, we show three C_3-symmetric stacking at 21.8°. In (a), the stacking corresponds to a metal site (M) in the electron layer overlapped with a metal site in the hole layer. In (b), a hexagon center (h) in the electron layer overlaps with a hexagon center in the hole layer. In (c), a chalcogen site (X) in the electron layer overlaps with a chalcogen site in the hole layer. In the 21.8° heterobilayer of the stacking in (a), (b) and (c), a spin-singlet interlayer exciton with the valley pairing $(\tau_c, \tau_v) = (-,+)$ then has the C_3 quantum numbers +1, -1, and 0 respectively[3,5]. This implies that for the stacking in (a), the $(-,+)$ interlayer exciton can emit a σ^+ circularly polarized photon, whereas for the stacking in (b), it can emit a σ^- circularly polarized photon.

The slight deviation $\delta\theta$ of the twist angle from the commensurate 21.8° will give rise to a concatenated moiré pattern. Different local regions correspond to 21.8° commensurate stacking of different interlayer translation, as shown in Fig. D-8d, where the $\boldsymbol{A}$, $\boldsymbol{B}$ and $\boldsymbol{C}$ locales correspond to the stacking pattern in (a), (b) and (c), respectively. The moiré periodicity is given by $\frac{a}{\sqrt{7}\delta\theta}$. Meanwhile the stacking-dependent interlayer hopping can lead to the periodic change of electronic band gaps[6], which gives rise to a spatially modulated excitonic potential $E(\mathbf{R})$, where $\mathbf{R}$ is the center position of the localized interlayer exciton. At locations $\boldsymbol{A}$, $\boldsymbol{B}$ or $\boldsymbol{C}$, the C_3 symmetry requires $\nabla_{\mathbf{R}} E(\mathbf{R}) = 0$, which means they correspond to energy extrema. Thus, an interlayer exciton will be localized at $\boldsymbol{A}$, $\boldsymbol{B}$ or $\boldsymbol{C}$ trapping sites in near 21.8° moiré pattern.

D.3 Supplementary figures

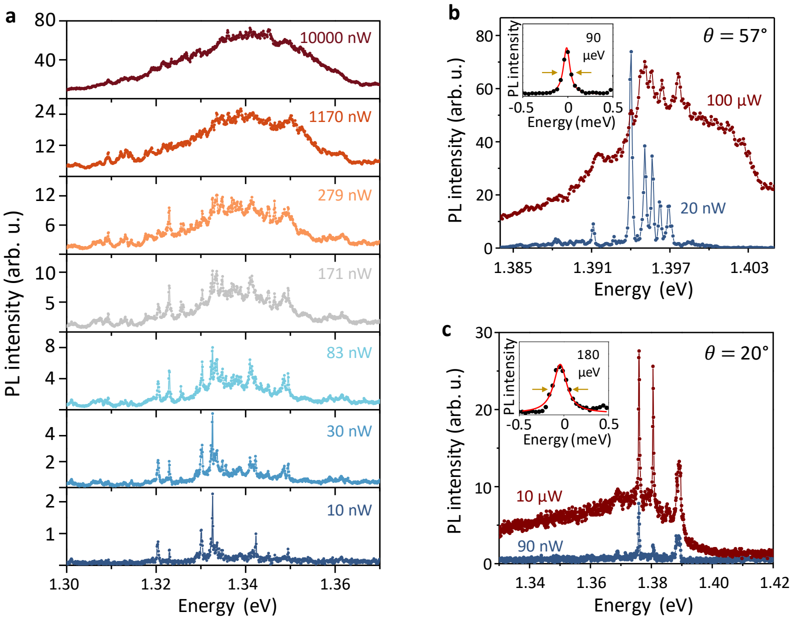

Fig. D-1 | Supplementary power dependence data. a, Interlayer exciton PL spectra at selected excitation powers for θ = 2° sample of device 1. **b**, **c**, PL spectra at low versus high power (indicated on the figure) for θ = 57° of device 2 (**b**) and θ = 20° of device 1 (**c**). Insets: Lorentzian fit to representative PL peaks with the indicated linewidths.

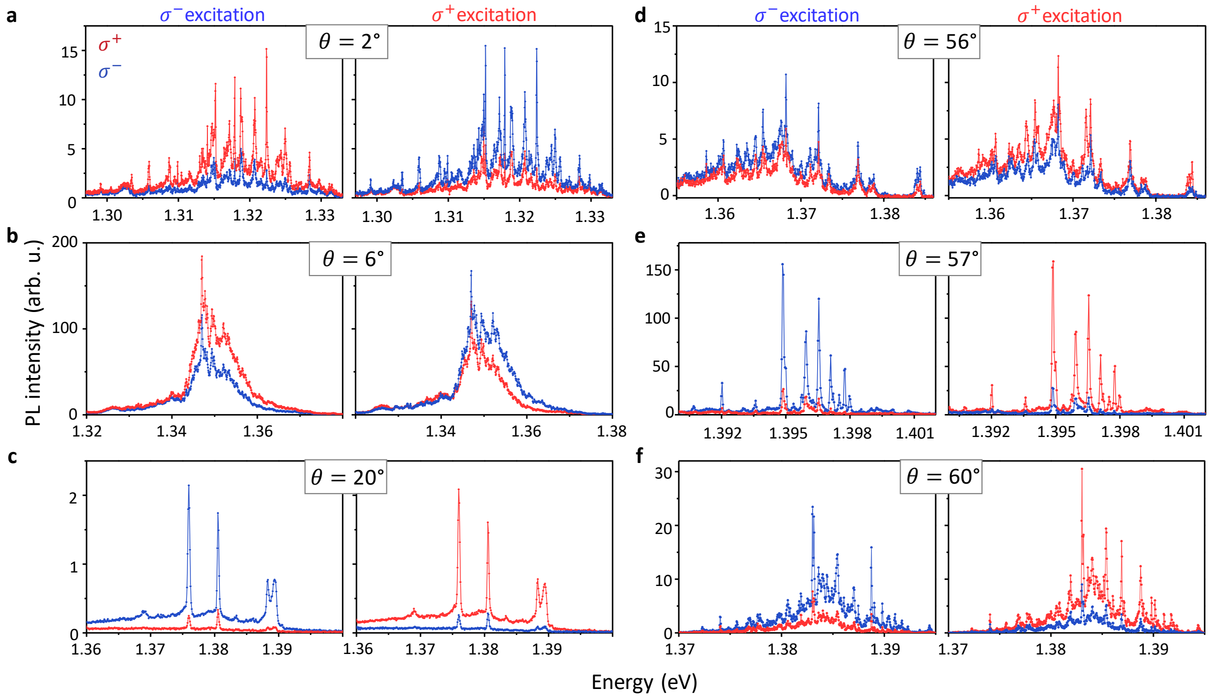

Figure D-3 | Supplementary circular-polarization-resolved PL spectra. Each subfigure represents data from a different sample with the indicated twist angle. The left and right columns of each subfigure correspond to σ^- and σ^+ polarized excitation. The red and blue curves indicate σ^+ and σ^- polarized PL components. Spectra from the θ = 2° and θ = 20° region of device 1 in the main text are shown in (**a**) and (**c**), while θ = 6° and θ = 57° from device 2 are shown in (**b**) and (**e**). The θ = 2° spectra in (**a**) were acquired on a different sample region from that of the spectra in main text, which shows similarly strong polarization reversal. The spectra in (**d**) and (**f**) are from

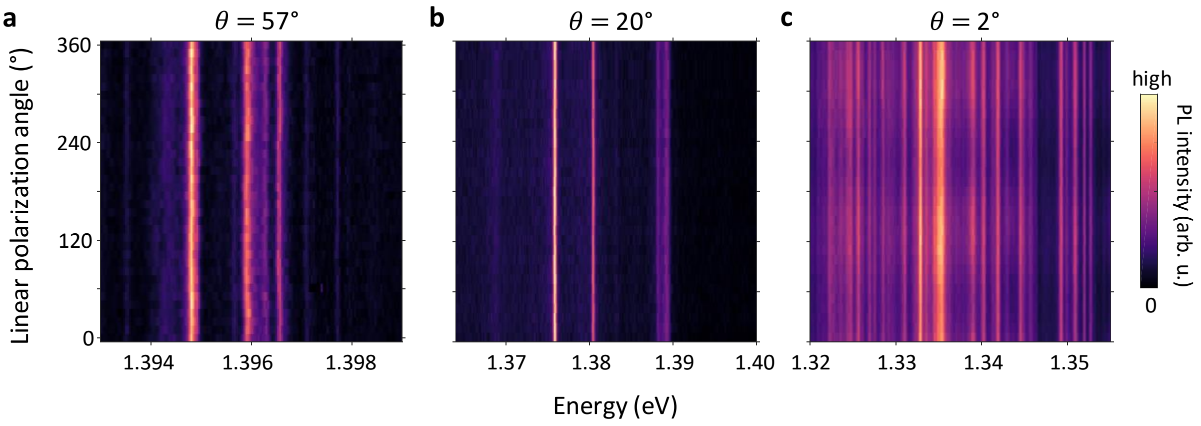

Figure D-4 | Linear-polarization-resolved PL. a-c, PL intensity plots as a function of the linear polarization detection angle and photon energy under linearly polarized excitation for θ = 57° (**a**), 20° (**b**), and 2° (**c**). No linear PL polarization is observed.

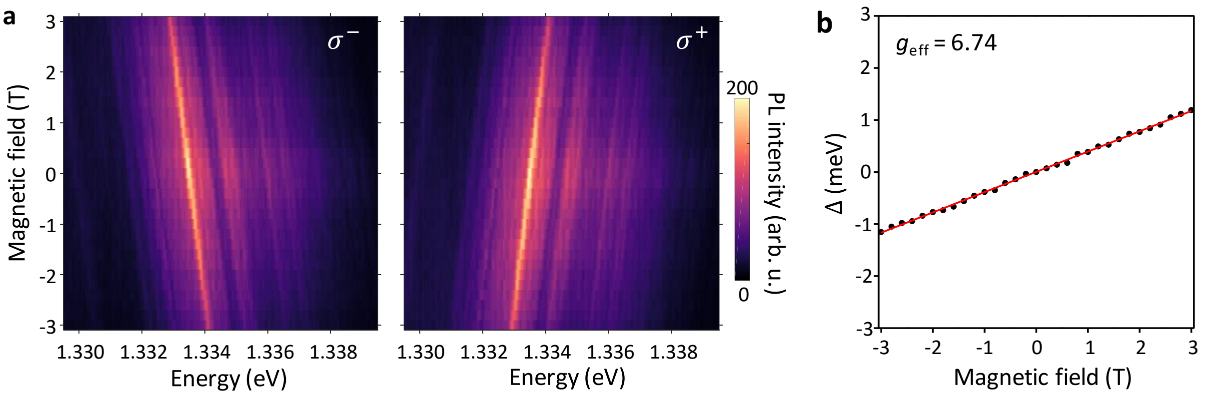

Figure D-5 | Free and trapped interlayer exciton *g*-factor for *θ* ~ 0°. The data is acquired on the θ = 6° region of device 2. **a**, PL intensity plot of σ^+ (right) and σ^- (left) components as a function of applied magnetic field and photon energy. The broad background (free exciton) clearly shifts with same slope as the sharp trapped interlayer exciton on top. **b**, Valley splitting versus applied magnetic field, from which a g-factor of 6.74 ± 0.05 is extracted from a linear fit to Δ versus B (red solid line).

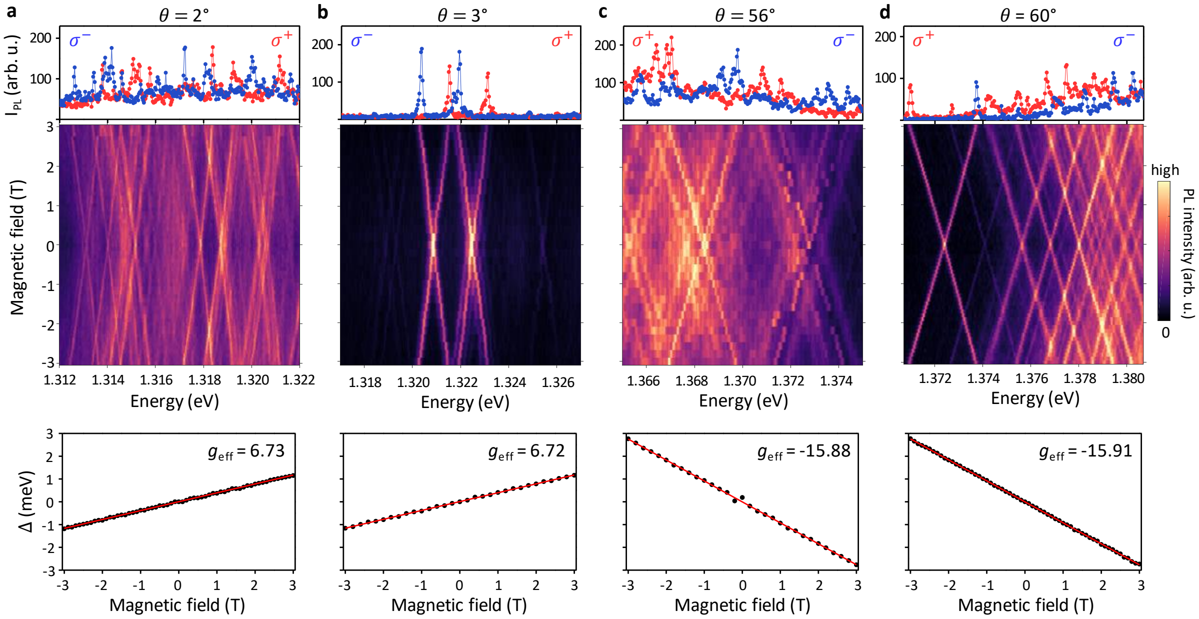

Figure D-6 | Uniformity of *g*-factors. a-d, Magneto-PL of 2° (**a**), 3° (**b**), 56° (**c**), and 60° (**d**) heterobilayers. The data in the 2° heterobilayer (**a**) was taken at a different spot from the one in the main text. The excitation is linearly polarized. Top row: Circularly polarized PL spectra at 3 T. Middle row: PL intensity as a function of applied magnetic field, which display a clear linear Zeeman shift of the σ^+ and σ^- components. Bottom row: Valley Zeeman splitting versus applied magnetic field. Linear fits (red solid lines) yield effective g-factors of heterobilayers at different twist angle, which are 6.73 ± 0.02, 6.72 ± 0.03, -15.88 ± 0.09, and -15.91± 0.02 for (**a**)-(**d**). The data confirm the g-factor uniformity across the same sample as well as different samples with similar twist angle.

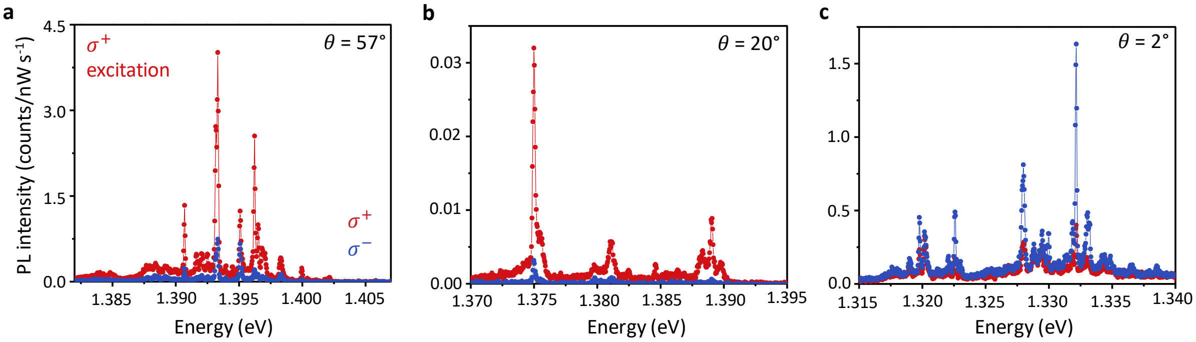

Figure D-7 | PL intensity from heterobilayers with different twist angles. The measurement reveals the PL intensity of $\theta = 2°$ and 57° is about 100 times stronger than that of $\theta = 20°$. Excitation powers were 10 nW for (**a**) and (**c**) and 100 nW for (**b**). The PL intensity for $\theta = 20°$ heterobilayer is still in the linear regime for powers less than 100 nW. Aside from the excitation power, the data from all three twist angles were acquired in identical experimental conditions to facilitate their comparison.

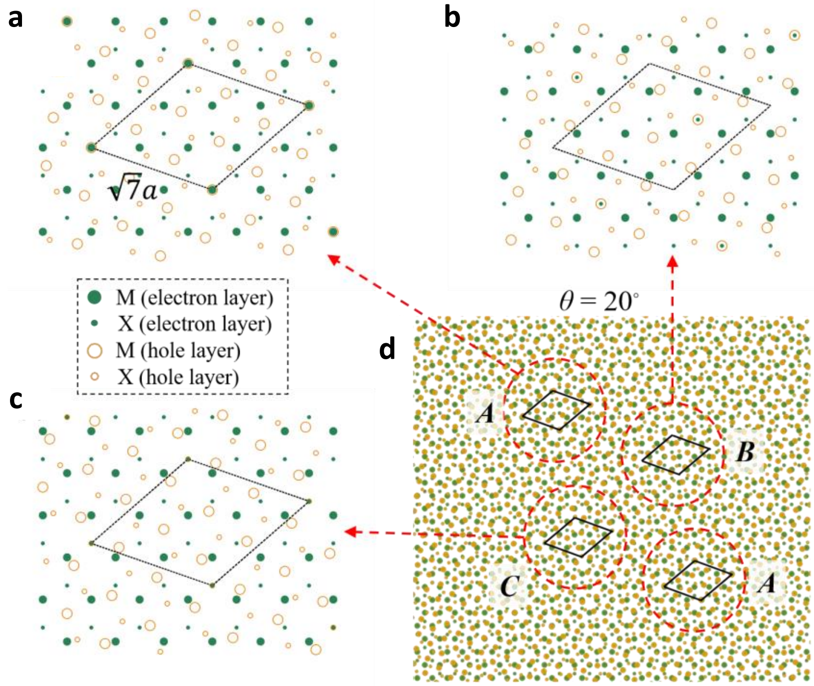

Figure D-8 | Heterobilayer moiré pattern for twist angle close to 21.8°. a-c, Three high-symmetry stacking patterns under the commensurate 21.8° twist angles for two layers with the same lattice constant a. The dashed diamonds give the smallest supercells, whose periodicity is $\sqrt{7}a$. The large (small) solid green dots denote the metal or M (chalcogen or X) sites in the electron layer, while the large (small) empty orange dots denote the metal or M (chalcogen or X) sites in the hole layer. (a) is the stacking where two M sites in different layers horizontally overlap. (b) is the stacking where two hexagon centers (h sites) in different layers horizontally overlap. (c) is the stacking where two X sites in different layers horizontally overlap. Because M, X and h are the C_3 rotation centers of the monolayers, the stacking in (a), (b) and (c) are all C_3 symmetric. **d**, Illustration of the moiré pattern when the twist angle slightly deviates from 21.8° (θ = 20° here). Red circles marked by ***A***, ***B*** and ***C*** are the local regions nearly indistinguishable from the 21.8° commensurate pattern in (a), (b) and (c), respectively. The black diamonds are the $\sqrt{7}a \times \sqrt{7}a$ supercells of the local regions.

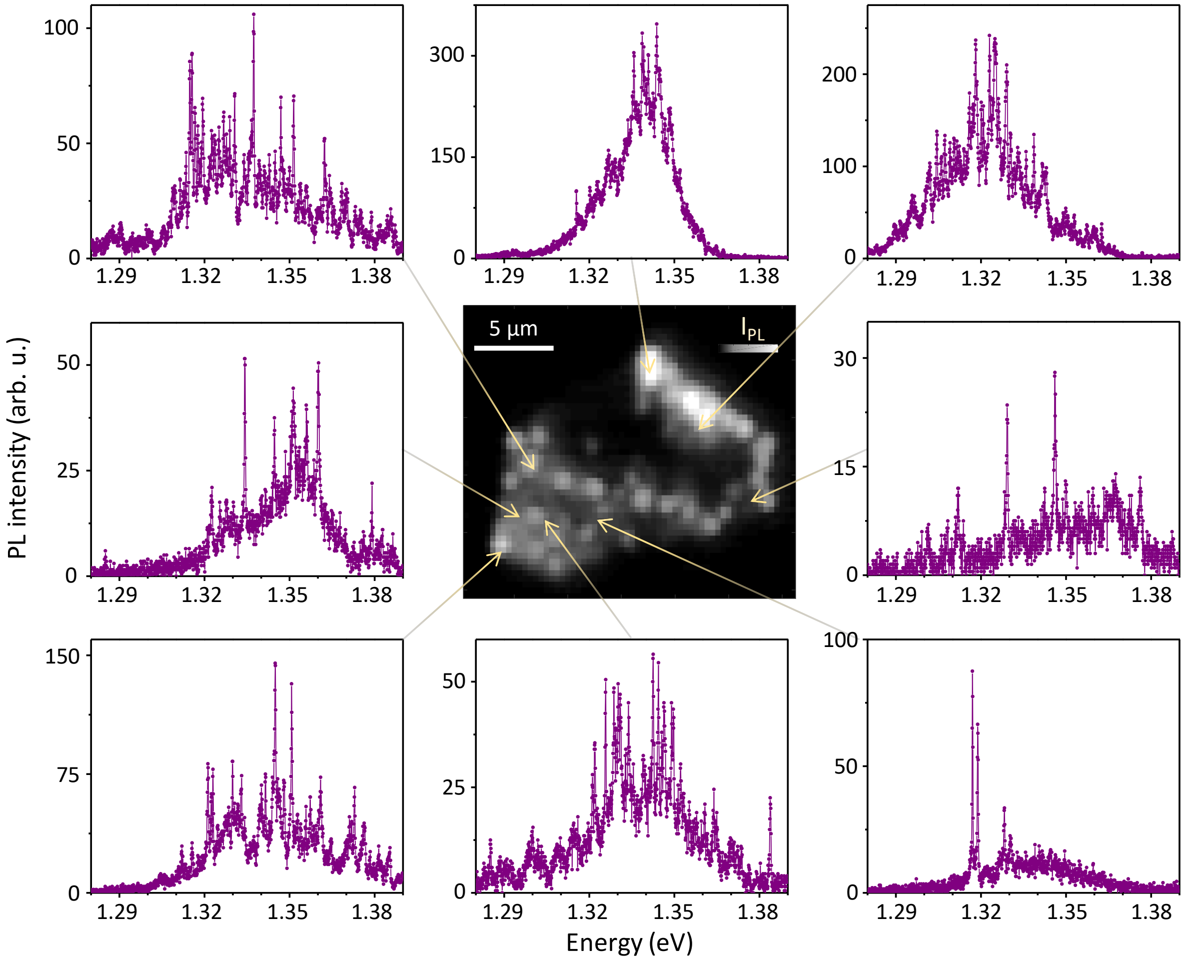

Extended Data Fig. 9 | Spatial homogeneity of interlayer exciton PL. The center image displays a spatial map of the integrated PL for the $\theta = 2°$ heterobilayer and the plots along the outside show selected interlayer exciton PL spectra at different sample locations. The PL is bright across a wide region of the sample, except along one edge of a crack that runs through the sample (note correspondence to sample height map in Fig. 1c of main text). Narrow-line PL emission is a general feature of the PL spectra across the sample, as seen in the selected spectra from spatially distinct regions of the sample. The number of narrow-line peaks, their intensities, and their energy distribution is inhomogeneous across the sample. The origin of this inhomogeneity is an important topic for further study.

Appendix E: Curriculum Vitae

E.1 CV at graduation

Pasqual Rivera

pasqual@uw.edu · 360.632.6168 · Seattle, WA

EDUCATION

- **Ph.D. in Physics** – University of Washington, Seattle, WA Sept. 2018
- B.S. in Physics – University of Washington, Seattle, WA 2013
- B.S. in Economics – Harvey Mudd College, Claremont, CA 2008

RESEARCH EXPERIENCE

Ph.D. Researcher | Xu Laboratory, UW Physics | 2013 – Present Advisor: Prof. Xiaodong Xu

- Spearheaded pioneering work discovering spatially-indirect excitons in two-dimensional semiconductor heterostructures and characterized their electronic and optical spin and valley properties. Currently a leading expert in this area.
- Innovated laboratory apparatus by implementing digital control and instrument integration. Deployed automated data acquisition systems, custom analysis programs, and programmatic controls via graphic user interfaces.
- Mentored many undergraduate research students and provided active leadership and guidance for new graduate students.
- Collaborated internationally to author a dozen research articles in top peer-reviewed journals, with 4 first author publications, including an invited review article in *Nature Nanotechnology* and a chapter in the textbook *2D Materials*.
- Instrument manager for TESCAN Vega SEM/EBL system – performed system maintenance and trained new users.
- Managed laboratory purchasing, and chemical and laser safety compliance and training.

Research Assistant | Optical Spintronics and Sensing Lab, UW Physics | 2012-2013 Advisor: Prof. Kai-Mei Fu

- Constructed an off-axis excitation microscope for low temperature optical spectroscopy measurements.
- Assisted in preliminary measurements towards determining the T_1 time of donor-bound electron spin states in bulk InP and GaAs.

PRIMARY SKILLS

- Proficient in polarization-sensitive and time-resolved optical spectroscopy, including the following important techniques:
    - Microscope design and construction – visible and mid-IR – free-space and fiber optics based systems.
    - Photoluminescence, photoluminescence excitation, transient absorption, and time-correlated single photon counting.
    - Ultrafast (femtosecond) and CW pump-probe, both degenerate and non-degenerate non-linear optical spectroscopy.
- Broad experience with laser systems, narrow band CW and mode-locked femtosecond Ti:Sapphire, regenerative and optical parametric amplifiers, supercontinuum generation, LEDs, wavemeters, and power stabilization systems.

- Experience with streak cameras, lock-in detection, AOM and EOM, SLM, and HBT photon correlation detection.
- Broad experience with cryogenic systems for low-temperature optical spectroscopy and electronic transport measurements.
- Strong programming skills for computerized instrument control, timing, and systems integration, DAQ automation, GUI design and deployment, and machine learning for data analysis. Primarily used Matlab and LabVIEW, but extensive coursework in Java and experience with Python and C++. Enthusiastic to become fluent in new programming languages.
- Familiar with FDTD for computational modeling of electrodynamic response and system design. Experience with Lumerical.
- UW Machine Shop certification; frequent use of precision high-speed milling machine, lathe, drill press, band saw, etc.
- Clean room certification from UW Washington Nanofabrication Facility; nanoscale optoelectronic device fabrication.
- Proficient use of AFM, SEM, EBL, ICP/RIE, sputtering and e-beam evaporation. Familiar with optical lithography techniques.
- Experience with various EBL systems fabricating >100 custom optoelectronic devices. JEOL, Tescan, FEI Sirion with Nabity.
- Superb written and oral communication skills in a multi-lingual environment. Extensive experience in public speaking, the writing of white papers, technical reports, SOPs, research and grant proposals, and academic articles and reviews for top journals.

EXTRACURRICULAR & OUTREACH ACTIVITIES

- Graduate Student Mentor · UW Physics Department · 2015-2017
- Clean Energy Institute Associated Outreach Activities · Across Puget Sound · 2015-2016
- Discovery Days · UW College of Engineering · 2014-2015
- Science Café · UW Society of Physics Students · 2014
- Paws-on Science · Pacific Science Center, Seattle, WA · 2014

ACADEMIC AWARDS

- **Hans G. Dehmelt Prize in Experimental Physics** · UW Department of Physics · 2016
- Clean Energy Institute Fellowship · Clean Energy Institute · 2016
- Graduate Opportunity Minority Achievement Program Research Award · UW GO-MAP · 2013-2014
- Undergraduate Research Scholarship · Washington NASA Space Grant Consortium · Summer 2012

CONFERENCE PRESENTATIONS

- Interlayer Exciton Optoelectronics in a 2D Heterostructure P-N Junction · APS March Meeting 2017
- Valley-Polarized Interlayer Excitons in 2D Semiconductor Heterostructures · APS March Meeting 2016
- Interlayer Physics in $MoSe_2$-WSe_2 Heterostructures · APS March Meeting 2015
- Bright Interlayer Exciton Dynamics in $MoSe_2$-WSe_2 Heterostructures · APS March Meeting 2014
- Measuring the spin relaxation time of donor-bound electrons in InP · APS NW Section Meeting 2012

PUBLICATIONS LIST

1. **P. Rivera**, H. Yu, K.L. Seyler, N.P. Wilson, W. Yao, X. Xu. “Interlayer valley excitons in heterobilayers of transition metal dichalcogenides.” Accepted for publication by *Nature Nanotechnology*. Aug 13 (2018).
2. K.L. Seyler*****, **P. Rivera***, H. Yu, N.P. Wilson, E. Ray, D.G. Mandrus, J. Yan, W. Yao, X. Xu. “Signatures of Moire-trapped Valley Excitons in $MoSe_2\backslash WSe_2$ Heterobilayers.” Currently under review at Nature. *****Author’s contributed equally to this work.
3. **P. Rivera**, K.L. Seyler, H. Yu, J.R. Schaibley, J. Yan, D.G. Mandrus, W. Yao, X. Xu. “Valley polarized exciton dynamics in a 2D semiconductor heterostructure.” *Science* 351, 688-691 (2016).

4. **P. Rivera**, J.R. Schaibley, A.M. Jones, J.S. Ross, S. Wu, G. Aivazian, P. Klement, K.L. Seyler, G. Clark, N.J. Ghimire, J. Yan, D.G. Mandrus, W. Yao, X. Xu. “Observation of long-lived interlayer excitons in monolayer MoSe2-WSe2 heterostructures.” *Nature Communications*. **6**, 6242 (2014).
5. **P. Rivera**, W. Yao, X. Xu. “Optical Properties of TMD Heterostructures.” *2D Materials: Properties and Devices*. Chapter 17, Cambridge University Press (2017). DOI:10.1017/9781316681619.
6. J.R. Schaibley, H. Yu, G. Clark, **P. Rivera**, J.S. Ross, K.L. Seyler, W. Yao, X. Xu, “Valleytronics in 2D materials.” ***Nature Reviews Materials*** 1, 16055 (2016).
7. J.R. Schaibley, **P. Rivera**, H. Yu, K.L. Seyler, J. Yan, D. G. Mandrus, T. Taniguchi, K. Watanabe, W. Yao, X. Xu. “Directional Interlayer Spin-Valley Transfer in 2D Heterostructures.” *Nature Communications* **7**, 13747, (2016).
8. J.S. Ross, **P. Rivera**, J.R. Schaibley, E. Lee-Wong, H. Yu, T. Taniguchi, K. Watanabe, J. Yan, D. Mandrus, D.H. Cobden, W. Yao, X. Xu. “Interlayer exciton optoelectronics in a 2D heterostructure p-n Junction”. *Nano Letters*. DOI: 10.1021/acs.nanolett.6b03398 (2017).
9. N.R. Wilson, P.V. Nguyen, K.L. Seyler, **P. Rivera**, A.J. Marsden, Z.P.L. Laker, G.C. Constantinescu, V. Kandyba, A. Barinov, N.D.M. Hine, X. Xu, D.H. Cobden. “Determination of band offsets, hybridization, and exciton binding in 2D semiconductor heterostructures”. ***Science Advances*** 3.2 (2017): e1601832.
10. C. Huang, S. Wu, A.M. Sanchez, J.JP. Peters, R. Beanland, J.S. Ross, **P. Rivera**, W. Yao, D.H. Cobden, and X. Xu. "Lateral heterojunctions within monolayer MoSe2–WSe2 semiconductors." *Nature Materials* 13, no. 12 (2014): 1096-1101.
11. G. Clark, S. Wu, **P. Rivera**, J. Finney, P. Nguyen, D.H. Cobden, X. Xu. "Vapor-transport growth of high optical quality WSe2 monolayers a." *APL Materials* 2, no. 10 (2014).
12. K.L. Seyler, J.R. Schaibley, P. Gong, **P. Rivera**, A.M. Jones, S. Wu, J. Yan, D.G. Mandrus, W. Yao, X. Xu. "Electrical control of second-harmonic generation in a WSe2 monolayer transistor." *Nature Nanotechnology* (2015).
13. J.R. Schaibley, T. Karin, H. Yu, J.S. Ross, **P. Rivera**, A.M. Jones, M.E. Scott, J. Yan, D.G. Mandrus, W. Yao, K.M. Fu, X. Xu. "Population Pulsation Resonances of Excitons in Monolayer MoSe 2 with Sub-1 μeV Linewidths." *Physical Review Letters* 114, no. 13 (2015).

REFERENCES

1. **Professor Xiaodong Xu | Ph.D. Advisor**
   Boeing Distinguished Associate Professor | University of Washington – Departments of Physics and MSE
   206.543.8444 | xuxd@uw.edu

2. **Professor John Schaibley | Former Post-Doctoral Mentor**
   Assistant Professor | University of Arizona – Department of Physics
   520.626.5112 | johnschaibley@email.arizona.edu

3. **Professor Arka Majumdar | Collaborator and Instructor**
   Assistant Professor | University of Washington – Departments of Physics and Electrical Engineering
   206.616.5558 | arka@uw.edu

4. **Catherine Provost | Character Reference**
   Graduate Students Advisor | University of Washington – Department of Physics
   206.543.2488 | cuala@uw.edu

List of References

1 Novoselov, K. S. *et al.* Electric field effect in atomically thin carbon films. *Science* **306**, 666-669, doi:10.1126/science.1102896 (2004).

2 Geim, A. K. & Novoselov, K. S. The rise of graphene. *Nature materials* **6**, 183-191, doi:10.1038/nmat1849 (2007).

3 Novoselov, K. S. *et al.* Two-dimensional gas of massless Dirac fermions in graphene. *Nature* **438**, 197-200, doi:10.1038/nature04233 (2005).

4 Das, S., Robinson, J. A., Dubey, M., Terrones, H. & Terrones, M. Beyond Graphene: Progress in Novel Two-Dimensional Materials and van der Waals Solids. *Annual Review of Materials Research* **45**, 1-27, doi:10.1146/annurev-matsci-070214-021034 (2015).

5 Novoselov, K. S. *et al.* Two-dimensional atomic crystals. *Proceedings of the National Academy of Sciences of the United States of America* **102**, 10451-10453, doi:10.1073/pnas.0502848102 (2005).

6 Butler, S. Z. *et al.* Progress, challenges, and opportunities in two-dimensional materials beyond graphene. *ACS Nano* **7**, 2898-2926, doi:10.1021/nn400280c (2013).

7 Xu, M., Liang, T., Shi, M. & Chen, H. Graphene-like two-dimensional materials. *Chemical reviews* **113**, 3766-3798, doi:10.1021/cr300263a (2013).

8 Miro, P., Audiffred, M. & Heine, T. An atlas of two-dimensional materials. *Chemical Society reviews* **43**, 6537-6554, doi:10.1039/c4cs00102h (2014).

9 Bhimanapati, G. R. *et al.* Recent Advances in Two-Dimensional Materials beyond Graphene. *ACS Nano* **9**, 11509-11539, doi:10.1021/acsnano.5b05556 (2015).

10 Mas-Balleste, R., Gomez-Navarro, C., Gomez-Herrero, J. & Zamora, F. 2D materials: to graphene and beyond. *Nanoscale* **3**, 20-30, doi:10.1039/c0nr00323a (2011).

11 Neto, A. H. C. & Novoselov, K. Two-Dimensional Crystals: Beyond Graphene. *Materials Express* **1**, 10-17, doi:10.1166/mex.2011.1002 (2011).

12 Lieth, R. & Terhell, J. in *Preparation and crystal growth of materials with layered structures* 141-223 (Springer, 1977).

13 Wilson, J. A. & Yoffe, A. The transition metal dichalcogenides discussion and interpretation of the observed optical, electrical and structural properties. *Advances in Physics* **18**, 193-335 (1969).

14 Mak, K. F., Lee, C., Hone, J., Shan, J. & Heinz, T. F. Atomically thin MoS(2): a new direct-gap semiconductor. *Physical review letters* **105**, 136805, doi:10.1103/PhysRevLett.105.136805 (2010).

15 Splendiani, A. *et al.* Emerging photoluminescence in monolayer MoS2. *Nano letters* **10**, 1271-1275, doi:10.1021/nl903868w (2010).

16 Li, Y. *et al.* Measurement of the optical dielectric function of monolayer transition-metal dichalcogenides:MoS2,MoSe2,WS2, andWSe2. *Physical Review B* **90**, doi:10.1103/PhysRevB.90.205422 (2014).

17 Ugeda, M. M. *et al.* Giant bandgap renormalization and excitonic effects in a monolayer transition metal dichalcogenide semiconductor. *Nature materials* **13**, 1091-1095, doi:10.1038/nmat4061 (2014).

18 Wang, Q. H., Kalantar-Zadeh, K., Kis, A., Coleman, J. N. & Strano, M. S. Electronics and optoelectronics of two-dimensional transition metal dichalcogenides. *Nature nanotechnology* **7**, 699-712, doi:10.1038/nnano.2012.193 (2012).

19 Jariwala, D., Sangwan, V. K., Lauhon, L. J., Marks, T. J. & Hersam, M. C. Emerging device applications for semiconducting two-dimensional transition metal dichalcogenides. *ACS Nano* **8**, 1102-1120, doi:10.1021/nn500064s (2014).

20 Lv, R. *et al.* Transition metal dichalcogenides and beyond: synthesis, properties, and applications of single- and few-layer nanosheets. *Accounts of chemical research* **48**, 56-64, doi:10.1021/ar5002846 (2015).

21 Wang, H., Feng, H. & Li, J. Graphene and graphene-like layered transition metal dichalcogenides in energy conversion and storage. *Small* **10**, 2165-2181, doi:10.1002/smll.201303711 (2014).

22 Bernardi, M., Palummo, M. & Grossman, J. C. Extraordinary sunlight absorption and one nanometer thick photovoltaics using two-dimensional monolayer materials. *Nano letters* **13**, 3664-3670, doi:10.1021/nl401544y (2013).

23 Xiao, D., Liu, G. B., Feng, W., Xu, X. & Yao, W. Coupled spin and valley physics in monolayers of MoS2 and other group-VI dichalcogenides. *Physical review letters* **108**, 196802, doi:10.1103/PhysRevLett.108.196802 (2012).

24 Yao, W., Xiao, D. & Niu, Q. Valley-dependent optoelectronics from inversion symmetry breaking. *Physical Review B* **77**, doi:10.1103/PhysRevB.77.235406 (2008).

25 Zeng, H., Dai, J., Yao, W., Xiao, D. & Cui, X. Valley polarization in MoS2 monolayers by optical pumping. *Nature nanotechnology* **7**, 490-493, doi:10.1038/nnano.2012.95 (2012).

26 Dean, C. R. *et al.* Boron nitride substrates for high-quality graphene electronics. *Nature nanotechnology* **5**, 722-726, doi:10.1038/nnano.2010.172 (2010).

27 Wang, L. *et al.* One-dimensional electrical contact to a two-dimensional material. *Science* **342**, 614-617, doi:10.1126/science.1244358 (2013).

28 Ponomarenko, L. A. *et al.* Cloning of Dirac fermions in graphene superlattices. *Nature* **497**, 594-597, doi:10.1038/nature12187 (2013).

29 Dean, C. R. *et al.* Hofstadter's butterfly and the fractal quantum Hall effect in moire superlattices. *Nature* **497**, 598-602, doi:10.1038/nature12186 (2013).

30 Hunt, B. *et al.* Massive Dirac fermions and Hofstadter butterfly in a van der Waals heterostructure. *Science* **340**, 1427-1430, doi:10.1126/science.1237240 (2013).

31 Geim, A. K. & Grigorieva, I. V. Van der Waals heterostructures. *Nature* **499**, 419-425, doi:10.1038/nature12385 (2013).

32 Novoselov, K. S., Mishchenko, A., Carvalho, A. & Castro Neto, A. H. 2D materials and van der Waals heterostructures. *Science* **353**, aac9439, doi:10.1126/science.aac9439 (2016).

33 Mak, K. F. & Shan, J. Photonics and optoelectronics of 2D semiconductor transition metal dichalcogenides. *Nature Photonics* **10**, 216-226, doi:10.1038/nphoton.2015.282 (2016).

34 Radisavljevic, B., Radenovic, A., Brivio, J., Giacometti, V. & Kis, A. Single-layer MoS2 transistors. *Nature nanotechnology* **6**, 147-150, doi:10.1038/nnano.2010.279 (2011).

35 Tsai, M. L. *et al.* Monolayer MoS2 heterojunction solar cells. *ACS Nano* **8**, 8317-8322, doi:10.1021/nn502776h (2014).

36 Furchi, M. M., Pospischil, A., Libisch, F., Burgdorfer, J. & Mueller, T. Photovoltaic effect in an electrically tunable van der Waals heterojunction. *Nano letters* **14**, 4785-4791, doi:10.1021/nl501962c (2014).

37 Baugher, B. W., Churchill, H. O., Yang, Y. & Jarillo-Herrero, P. Optoelectronic devices based on electrically tunable p-n diodes in a monolayer dichalcogenide. *Nature nanotechnology* **9**, 262-267, doi:10.1038/nnano.2014.25 (2014).

38 Ross, J. S. *et al.* Electrically tunable excitonic light-emitting diodes based on monolayer WSe2 p-n junctions. *Nature nanotechnology* **9**, 268-272, doi:10.1038/nnano.2014.26 (2014).

39 Cheng, R. *et al.* Electroluminescence and photocurrent generation from atomically sharp WSe2/MoS2 heterojunction p-n diodes. *Nano letters* **14**, 5590-5597, doi:10.1021/nl502075n (2014).

40 Chhowalla, M. *et al.* The chemistry of two-dimensional layered transition metal dichalcogenide nanosheets. *Nature chemistry* **5**, 263-275, doi:10.1038/nchem.1589 (2013).

41 Mattheiss, L. F. Band Structures of Transition-Metal-Dichalcogenide Layer Compounds. *Physical Review B* **8**, 3719-3740, doi:10.1103/PhysRevB.8.3719 (1973).

42 Eda, G. *et al.* Photoluminescence from chemically exfoliated MoS2. *Nano letters* **11**, 5111-5116, doi:10.1021/nl201874w (2011).

43 Ashcroft, N. W., Mermin, N. D. & Rodriguez, S. (AAPT, 1978).

44 Castro Neto, A. H., Guinea, F., Peres, N. M. R., Novoselov, K. S. & Geim, A. K. The electronic properties of graphene. *Reviews of Modern Physics* **81**, 109-162, doi:10.1103/RevModPhys.81.109 (2009).

45 Xu, X., Yao, W., Xiao, D. & Heinz, T. F. Spin and pseudospins in layered transition metal dichalcogenides. *Nature Physics* **10**, 343-350, doi:10.1038/nphys2942 (2014).

46 Liu, G.-B., Shan, W.-Y., Yao, Y., Yao, W. & Xiao, D. Three-band tight-binding model for monolayers of group-VIB transition metal dichalcogenides. *Physical Review B* **88**, doi:10.1103/PhysRevB.88.085433 (2013).

47 Schaibley, J. R. *et al.* Valleytronics in 2D materials. *Nature Reviews Materials* **1**, 16055, doi:10.1038/Natrevmats.2016.55 (2016).

48 Mak, K. F., He, K., Shan, J. & Heinz, T. F. Control of valley polarization in monolayer MoS2 by optical helicity. *Nature nanotechnology* **7**, 494-498, doi:10.1038/nnano.2012.96 (2012).

49 Jones, A. M. *et al.* Optical generation of excitonic valley coherence in monolayer WSe2. *Nature nanotechnology* **8**, 634-638, doi:10.1038/nnano.2013.151 (2013).

50 Yu, H., Liu, G. B., Gong, P., Xu, X. & Yao, W. Dirac cones and Dirac saddle points of bright excitons in monolayer transition metal dichalcogenides. *Nature communications* **5**, 3876, doi:10.1038/ncomms4876 (2014).

51 Mak, K. F. *et al.* Tightly bound trions in monolayer MoS2. *Nature materials* **12**, 207-211, doi:10.1038/nmat3505 (2013).

52 Ross, J. S. *et al.* Electrical control of neutral and charged excitons in a monolayer semiconductor. *Nat Commun* **4**, 1474, doi:10.1038/ncomms2498 (2013).

53 Berkelbach, T. C., Hybertsen, M. S. & Reichman, D. R. Theory of neutral and charged excitons in monolayer transition metal dichalcogenides. *Physical Review B* **88**, doi:10.1103/PhysRevB.88.045318 (2013).

54 Kylänpää, I. & Komsa, H.-P. Binding energies of exciton complexes in transition metal dichalcogenide monolayers and effect of dielectric environment. *Physical Review B* **92**, doi:10.1103/PhysRevB.92.205418 (2015).

55 Zhang, X. X., You, Y., Zhao, S. Y. & Heinz, T. F. Experimental Evidence for Dark Excitons in Monolayer WSe_{2}. *Physical review letters* **115**, 257403, doi:10.1103/PhysRevLett.115.257403 (2015).

56 Echeverry, J. P., Urbaszek, B., Amand, T., Marie, X. & Gerber, I. C. Splitting between bright and dark excitons in transition metal dichalcogenide monolayers. *Physical Review B* **93**, doi:10.1103/PhysRevB.93.121107 (2016).

57 Wang, G. *et al.* In-Plane Propagation of Light in Transition Metal Dichalcogenide Monolayers: Optical Selection Rules. *Physical review letters* **119**, 047401, doi:10.1103/PhysRevLett.119.047401 (2017).

58 Zhang, X. X. *et al.* Magnetic brightening and control of dark excitons in monolayer WSe2. *Nature nanotechnology* **12**, 883-888, doi:10.1038/nnano.2017.105 (2017).

59 Molas, M. R. *et al.* Brightening of dark excitons in monolayers of semiconducting transition metal dichalcogenides. *2D Materials* **4**, 021003, doi:10.1088/2053-1583/aa5521 (2017).

60 Zhou, Y. *et al.* Probing dark excitons in atomically thin semiconductors via near-field coupling to surface plasmon polaritons. *Nature nanotechnology* **12**, 856-860, doi:10.1038/nnano.2017.106 (2017).

61 Robert, C. *et al.* Fine structure and lifetime of dark excitons in transition metal dichalcogenide monolayers. *Physical Review B* **96**, doi:10.1103/PhysRevB.96.155423 (2017).

62 Aharonovich, I., Englund, D. & Toth, M. Solid-state single-photon emitters. *Nature Photonics* **10**, 631-641, doi:10.1038/nphoton.2016.186 (2016).

63 He, Y. M. *et al.* Single quantum emitters in monolayer semiconductors. *Nat Nanotechnol* **10**, 497-502, doi:10.1038/nnano.2015.75 (2015).

64 Tonndorf, P. *et al.* Single-photon emission from localized excitons in an atomically thin semiconductor. *Optica* **2**, 347, doi:10.1364/optica.2.000347 (2015).

65 Srivastava, A. *et al.* Optically active quantum dots in monolayer WSe2. *Nat Nanotechnol* **10**, 491-496, doi:10.1038/nnano.2015.60 (2015).

66 Koperski, M. *et al.* Single photon emitters in exfoliated WSe2 structures. *Nat Nanotechnol* **10**, 503-506, doi:10.1038/nnano.2015.67 (2015).

67 Kumar, S., Kaczmarczyk, A. & Gerardot, B. D. Strain-Induced Spatial and Spectral Isolation of Quantum Emitters in Mono- and Bilayer WSe2. *Nano letters* **15**, 7567-7573, doi:10.1021/acs.nanolett.5b03312 (2015).

68 Kern, J. *et al.* Nanoscale Positioning of Single-Photon Emitters in Atomically Thin WSe2. *Advanced materials* **28**, 7101-7105, doi:10.1002/adma.201600560 (2016).

69 Branny, A., Kumar, S., Proux, R. & Gerardot, B. D. Deterministic strain-induced arrays of quantum emitters in a two-dimensional semiconductor. *Nat Commun* **8**, 15053, doi:10.1038/ncomms15053 (2017).

70 Palacios-Berraquero, C. *et al.* Large-scale quantum-emitter arrays in atomically thin semiconductors. *Nat Commun* **8**, 15093, doi:10.1038/ncomms15093 (2017).

71 Schwarz, S. *et al.* Electrically pumped single-defect light emitters in WSe2. *2D Materials* **3**, 025038, doi:10.1088/2053-1583/3/2/025038 (2016).

72 Clark, G. *et al.* Single Defect Light-Emitting Diode in a van der Waals Heterostructure. *Nano letters* **16**, 3944-3948, doi:10.1021/acs.nanolett.6b01580 (2016).

73 Palacios-Berraquero, C. *et al.* Atomically thin quantum light-emitting diodes. *Nature communications* **7**, 12978, doi:10.1038/ncomms12978 (2016).

74 Maialle, M. Z., de Andrada e Silva, E. A. & Sham, L. J. Exciton spin dynamics in quantum wells. *Physical review. B, Condensed matter* **47**, 15776-15788, doi:10.1103/PhysRevB.47.15776 (1993).

75 Late, D. J., Liu, B., Matte, H. S. S. R., Rao, C. N. R. & Dravid, V. P. Rapid Characterization of Ultrathin Layers of Chalcogenides on SiO2/Si Substrates. *Advanced Functional Materials* **22**, 1894-1905, doi:10.1002/adfm.201102913 (2012).

76 Roddaro, S., Pingue, P., Piazza, V., Pellegrini, V. & Beltram, F. The optical visibility of graphene: interference colors of ultrathin graphite on SiO(2). *Nano letters* **7**, 2707-2710, doi:10.1021/nl071158l (2007).

77 Huang, Y. *et al.* Reliable Exfoliation of Large-Area High-Quality Flakes of Graphene and Other Two-Dimensional Materials. *ACS Nano* **9**, 10612-10620, doi:10.1021/acsnano.5b04258 (2015).

78 Zomer, P. J., Guimarães, M. H. D., Brant, J. C., Tombros, N. & van Wees, B. J. Fast pick up technique for high quality heterostructures of bilayer graphene and hexagonal boron nitride. *Applied Physics Letters* **105**, 013101, doi:10.1063/1.4886096 (2014).

79 Purdie, D. G. *et al.* Cleaning interfaces in layered materials heterostructures. *arXiv:1803.00912* (2018).

80 Gong, C. *et al.* Band alignment of two-dimensional transition metal dichalcogenides: Application in tunnel field effect transistors. *Applied Physics Letters* **103**, 053513, doi:10.1063/1.4817409 (2013).

81 Kang, J., Tongay, S., Zhou, J., Li, J. B. & Wu, J. Q. Band offsets and heterostructures of two-dimensional semiconductors. *Applied Physics Letters* **102**, 012111, doi:10.1063/1.4774090 (2013).

82 Wang, Y., Wang, Z., Yao, W., Liu, G. B. & Yu, H. Y. Interlayer coupling in commensurate and incommensurate bilayer structures of transition-metal dichalcogenides. *Physical Review B* **95**, 115429, doi:10.1103/Physrevb.95.115429 (2017).

83 Komsa, H. P. & Krasheninnikov, A. V. Electronic structures and optical properties of realistic transition metal dichalcogenide heterostructures from first principles. *Physical Review B* **88**, 085318, doi:10.1103/Physrevb.88.085318 (2013).

84 Heo, H. *et al.* Interlayer orientation-dependent light absorption and emission in monolayer semiconductor stacks. *Nature communications* **6**, 7372, doi:10.1038/ncomms8372 (2015).

85 Kośmider, K. & Fernández-Rossier, J. Electronic properties of the MoS2-WS2heterojunction. *Physical Review B* **87**, doi:10.1103/PhysRevB.87.075451 (2013).

86 Terrones, H., Lopez-Urias, F. & Terrones, M. Novel hetero-layered materials with tunable direct band gaps by sandwiching different metal disulfides and diselenides. *Scientific reports* **3**, 1549, doi:10.1038/srep01549 (2013).

87 Amin, B., Singh, N. & Schwingenschlogl, U. Heterostructures of transition metal dichalcogenides. *Physical Review B* **92**, 075439, doi:10.1103/Physrevb.92.075439 (2015).

88 Tongay, S. *et al.* Tuning interlayer coupling in large-area heterostructures with CVD-grown MoS2 and WS2 monolayers. *Nano letters* **14**, 3185-3190, doi:10.1021/nl500515q (2014).

89 Liu, K. *et al.* Evolution of interlayer coupling in twisted molybdenum disulfide bilayers. *Nature communications* **5**, 4966, doi:10.1038/ncomms5966 (2014).

90 van der Zande, A. M. *et al.* Tailoring the electronic structure in bilayer molybdenum disulfide via interlayer twist. *Nano letters* **14**, 3869-3875, doi:10.1021/nl501077m (2014).

91 Yu, H., Wang, Y., Tong, Q., Xu, X. & Yao, W. Anomalous Light Cones and Valley Optical Selection Rules of Interlayer Excitons in Twisted Heterobilayers. *Physical review letters* **115**, 187002, doi:10.1103/PhysRevLett.115.187002 (2015).

92 Liu, C. S., Xu, T. F., Liu, Y. H. & Jing, X. L. Theory of indirect exciton photoluminescence in elevated quantum trap. *Physica E: Low-dimensional Systems and Nanostructures* **63**, 193-198, doi:10.1016/j.physe.2014.05.028 (2014).

93 Ceballos, F., Bellus, M. Z., Chiu, H. Y. & Zhao, H. Ultrafast charge separation and indirect exciton formation in a MoS2-MoSe2 van der Waals heterostructure. *ACS Nano* **8**, 12717-12724, doi:10.1021/nn505736z (2014).

94 Hong, X. *et al.* Ultrafast charge transfer in atomically thin MoS(2)/WS(2) heterostructures. *Nature nanotechnology* **9**, 682-686, doi:10.1038/nnano.2014.167 (2014).

95 Zhu, H. *et al.* Interfacial Charge Transfer Circumventing Momentum Mismatch at Two-Dimensional van der Waals Heterojunctions. *Nano letters* **17**, 3591-3598, doi:10.1021/acs.nanolett.7b00748 (2017).

96 Peng, B. *et al.* Ultrafast charge transfer in MoS2/WSe2p–n Heterojunction. *2D Materials* **3**, 025020, doi:10.1088/2053-1583/3/2/025020 (2016).

97 Hsu, W. T. *et al.* Negative circular polarization emissions from WSe2/MoSe2 commensurate heterobilayers. *Nature communications* **9**, 1356, doi:10.1038/s41467-018-03869-7 (2018).

98 Chiu, M. H. *et al.* Determination of band alignment in the single-layer MoS2/WSe2 heterojunction. *Nature communications* **6**, 7666, doi:10.1038/ncomms8666 (2015).

99 Zhang, C. *et al.* Interlayer couplings, Moire patterns, and 2D electronic superlattices in MoS2/WSe2 hetero-bilayers. *Science advances* **3**, e1601459, doi:10.1126/sciadv.1601459 (2017).

100 Hill, H. M., Rigosi, A. F., Rim, K. T., Flynn, G. W. & Heinz, T. F. Band Alignment in MoS2/WS2 Transition Metal Dichalcogenide Heterostructures Probed by Scanning Tunneling Microscopy and Spectroscopy. *Nano letters* **16**, 4831-4837, doi:10.1021/acs.nanolett.6b01007 (2016).

101 Wilson, N. R. *et al.* Determination of band offsets, hybridization, and exciton binding in 2D semiconductor heterostructures. *Science advances* **3**, e1601832, doi:10.1126/sciadv.1601832 (2017).

102 Bistritzer, R. & MacDonald, A. H. Transport between twisted graphene layers. *Physical Review B* **81**, doi:10.1103/PhysRevB.81.245412 (2010).

103 Mishchenko, A. *et al.* Twist-controlled resonant tunnelling in graphene/boron nitride/graphene heterostructures. *Nature nanotechnology* **9**, 808-813, doi:10.1038/nnano.2014.187 (2014).

104 Schuller, J. A. *et al.* Orientation of luminescent excitons in layered nanomaterials. *Nature nanotechnology* **8**, 271-276, doi:10.1038/nnano.2013.20 (2013).

105 Cao, T. *et al.* Valley-selective circular dichroism of monolayer molybdenum disulphide. *Nature communications* **3**, 887, doi:10.1038/ncomms1882 (2012).

106 Gong, Z. *et al.* Magnetoelectric effects and valley-controlled spin quantum gates in transition metal dichalcogenide bilayers. *Nature communications* **4**, 2053, doi:10.1038/ncomms3053 (2013).

107 Jones, A. M. *et al.* Spin-layer locking effects in optical orientation of exciton spin in bilayer WSe2. *Nature Physics* **10**, 130-134, doi:10.1038/Nphys2848 (2014).

108 Su, J.-J. & MacDonald, A. H. How to make a bilayer exciton condensate flow. *Nature Physics* **4**, 799-802, doi:10.1038/nphys1055 (2008).

109 Kumar, N. *et al.* Second harmonic microscopy of monolayer MoS2. *Physical Review B* **87**, doi:10.1103/Physrevb.87.161403 (2013).

110 Hsu, W. T. *et al.* Second harmonic generation from artificially stacked transition metal dichalcogenide twisted bilayers. *ACS Nano* **8**, 2951-2958, doi:10.1021/nn500228r (2014).

111 Malard, L. M., Alencar, T. V., Barboza, A. P. M., Mak, K. F. & de Paula, A. M. Observation of intense second harmonic generation from MoS2atomic crystals. *Physical Review B* **87**, doi:10.1103/PhysRevB.87.201401 (2013).

112 Li, Y. *et al.* Probing symmetry properties of few-layer MoS2 and h-BN by optical second-harmonic generation. *Nano letters* **13**, 3329-3333, doi:10.1021/nl401561r (2013).

113 Shi, H. *et al.* Exciton dynamics in suspended monolayer and few-layer MoS(2) 2D crystals. *ACS Nano* **7**, 1072-1080, doi:10.1021/nn303973r (2013).

114 Lagarde, D. *et al.* Carrier and polarization dynamics in monolayer MoS2. *Physical review letters* **112**, 047401, doi:10.1103/PhysRevLett.112.047401 (2014).

115 Wang, G. *et al.* Valley dynamics probed through charged and neutral exciton emission in monolayerWSe2. *Physical Review B* **90**, doi:10.1103/PhysRevB.90.075413 (2014).

116 Mai, C. *et al.* Many-body effects in valleytronics: direct measurement of valley lifetimes in single-layer MoS2. *Nano letters* **14**, 202-206, doi:10.1021/nl403742j (2014).

117 Kormányos, A., Zólyomi, V., Drummond, N. D. & Burkard, G. Spin-Orbit Coupling, Quantum Dots, and Qubits in Monolayer Transition Metal Dichalcogenides. *Physical Review X* **4**, doi:10.1103/PhysRevX.4.011034 (2014).

118 Butov, L. V., Lai, C. W., Ivanov, A. L., Gossard, A. C. & Chemla, D. S. Towards Bose-Einstein condensation of excitons in potential traps. *Nature* **417**, 47-52, doi:10.1038/417047a (2002).

119 Fang, H. *et al.* Strong interlayer coupling in van der Waals heterostructures built from single-layer chalcogenides. *Proceedings of the National Academy of Sciences of the United States of America* **111**, 6198-6202, doi:10.1073/pnas.1405435111 (2014).

120 Lee, C. H. *et al.* Atomically thin p-n junctions with van der Waals heterointerfaces. *Nature nanotechnology* **9**, 676-681, doi:10.1038/nnano.2014.150 (2014).

121 Lin, Y. C. *et al.* Atomically thin resonant tunnel diodes built from synthetic van der Waals heterostructures. *Nature communications* **6**, 7311, doi:10.1038/ncomms8311 (2015).

122 Gong, Y. *et al.* Vertical and in-plane heterostructures from WS2/MoS2 monolayers. *Nature materials* **13**, 1135-1142, doi:10.1038/nmat4091 (2014).

123 Rivera, P. *et al.* Observation of long-lived interlayer excitons in monolayer MoSe2-WSe2 heterostructures. *Nature communications* **6**, 6242, doi:10.1038/ncomms7242 (2015).

124 Butov, L. V., Gossard, A. C. & Chemla, D. S. Macroscopically ordered state in an exciton system. *Nature* **418**, 751-754, doi:10.1038/nature00943 (2002).

125 Snoke, D., Denev, S., Liu, Y., Pfeiffer, L. & West, K. Long-range transport in excitonic dark states in coupled quantum wells. *Nature* **418**, 754-757, doi:10.1038/nature00940 (2002).

126 Leonard, J. R. *et al.* Spin transport of excitons. *Nano letters* **9**, 4204-4208, doi:10.1021/nl9024227 (2009).

127 Finkman, E., Sturge, M. D. & Tamargo, M. C. X-point excitons in AlAs/GaAs superlattices. *Applied Physics Letters* **49**, 1299-1301, doi:10.1063/1.97392 (1986).

128 Gilliland, G. D. *et al.* Direct measurement of heavy-hole exciton transport in type-II GaAs/AlAs superlattices. *Physical review letters* **71**, 3717-3720, doi:10.1103/PhysRevLett.71.3717 (1993).

129 Fogler, M. M., Butov, L. V. & Novoselov, K. S. High-temperature superfluidity with indirect excitons in van der Waals heterostructures. *Nature communications* **5**, 4555, doi:10.1038/ncomms5555 (2014).

130 Appendix B.

131 Wang, Q. *et al.* Valley carrier dynamics in monolayer molybdenum disulfide from helicity-resolved ultrafast pump-probe spectroscopy. *ACS Nano* **7**, 11087-11093, doi:10.1021/nn405419h (2013).

132 Zhu, C. R. *et al.* Exciton valley dynamics probed by Kerr rotation inWSe2monolayers. *Physical Review B* **90**, doi:10.1103/PhysRevB.90.161302 (2014).

133 Wu, S. *et al.* Monolayer semiconductor nanocavity lasers with ultralow thresholds. *Nature* **520**, 69-72, doi:10.1038/nature14290 (2015).

134 Wu, S. *et al.* Control of two-dimensional excitonic light emission via photonic crystal. *2D Materials* **1**, 011001, doi:10.1088/2053-1583/1/1/011001 (2014).

135 Yu, H., Liu, G.-B. & Yao, W. Brightened spin-triplet interlayer excitons and optical selection rules in van der Waals heterobilayers. *2D Materials* **5**, 035021, doi:10.1088/2053-1583/aac065 (2018).

136 García de Abajo, F. J. Special Issue "2D Materials for Nanophotonics". *ACS Photonics* **4**, 2959-2961, doi:10.1021/acsphotonics.7b01399 (2017).

137 Xia, F., Wang, H., Xiao, D., Dubey, M. & Ramasubramaniam, A. Two-dimensional material nanophotonics. *Nature Photonics* **8**, 899-907, doi:10.1038/nphoton.2014.271 (2014).

138 Nagler, P. *et al.* Interlayer exciton dynamics in a dichalcogenide monolayer heterostructure. *2d Materials* **4**, 025112, doi:10.1088/2053-1583/Aa7352 (2017).

139 Rivera, P. *et al.* Valley-polarized exciton dynamics in a 2D semiconductor heterostructure. *Science* **351**, 688-691, doi:10.1126/science.aac7820 (2016).

140 Jiang, C. *et al.* Microsecond dark-exciton valley polarization memory in two-dimensional heterostructures. *Nature communications* **9**, 753, doi:10.1038/s41467-018-03174-3 (2018).

141 Miller, B. *et al.* Long-Lived Direct and Indirect Interlayer Excitons in van der Waals Heterostructures. *Nano letters* **17**, 5229-5237, doi:10.1021/acs.nanolett.7b01304 (2017).

142 Ross, J. S. *et al.* Interlayer Exciton Optoelectronics in a 2D Heterostructure p-n Junction. *Nano letters* **17**, 638-643, doi:10.1021/acs.nanolett.6b03398 (2017).

143 Dufferwiel, S. *et al.* Valley-addressable polaritons in atomically thin semiconductors. *Nature Photonics* **11**, 497-501, doi:10.1038/nphoton.2017.125 (2017).

144 Sun, Z. *et al.* Optical control of room-temperature valley polaritons. *Nature Photonics* **11**, 491-496, doi:10.1038/nphoton.2017.121 (2017).

145 Liu, C. H. *et al.* Nanocavity Integrated van der Waals Heterostructure Light-Emitting Tunneling Diode. *Nano letters* **17**, 200-205, doi:10.1021/acs.nanolett.6b03801 (2017).

146 Fryett, T. K. *et al.* Silicon photonic crystal cavity enhanced second-harmonic generation from monolayer WSe2. *2D Materials* **4**, 015031, doi:10.1088/2053-1583/4/1/015031 (2016).

147 Yu, H., Liu, G. B., Tang, J., Xu, X. & Yao, W. Moire excitons: From programmable quantum emitter arrays to spin-orbit-coupled artificial lattices. *Science advances* **3**, e1701696, doi:10.1126/sciadv.1701696 (2017).

148 FengCheng Wu, T. L., A.H. MacDonald. Theory of Optical Absorption by Interlayer Excitons in Transition Metal Dichalcogenide Heterobilayers. *arXiv:1710.10278* (2017).

149 Cao, Y. *et al.* Correlated insulator behaviour at half-filling in magic-angle graphene superlattices. *Nature* **556**, 80-84, doi:10.1038/nature26154 (2018).

150 Chen, G. *et al.* Gate-Tunable Mott Insulator in Trilayer Graphene-Boron Nitride Moiré Superlattice. *arXiv:1803.01985* (2018).

151 Cao, Y. *et al.* Unconventional superconductivity in magic-angle graphene superlattices. *Nature* **556**, 43-50, doi:10.1038/nature26160 (2018).

152 Jin, C. *et al.* Imaging of pure spin-valley diffusion current in WS2-WSe2 heterostructures. *Science* **360**, 893-896, doi:10.1126/science.aao3503 (2018).

153 Rivera, P. *et al.* Interlayer valley excitons in heterobilayers of transition metal dichalcogenides. *Nature nanotechnology*, doi:10.1038/s41565-018-0193-0 (2018).

154 Nagler, P. *et al.* Giant magnetic splitting inducing near-unity valley polarization in van der Waals heterostructures. *Nature communications* **8**, 1551, doi:10.1038/s41467-017-01748-1 (2017).

155 Bloch, I. Ultracold quantum gases in optical lattices. *Nature Physics* **1**, 23-30, doi:10.1038/nphys138 (2005).

156 Chakraborty, C., Kinnischtzke, L., Goodfellow, K. M., Beams, R. & Vamivakas, A. N. Voltage-controlled quantum light from an atomically thin semiconductor. *Nature nanotechnology* **10**, 507-511, doi:10.1038/nnano.2015.79 (2015).

157 Tran, T. T., Bray, K., Ford, M. J., Toth, M. & Aharonovich, I. Quantum emission from hexagonal boron nitride monolayers. *Nature nanotechnology* **11**, 37-41, doi:10.1038/nnano.2015.242 (2016).

158 Hanbicki, A. T. *et al.* Double Indirect Interlayer Exciton in a MoSe2/WSe2 van der Waals Heterostructure. *ACS Nano* **12**, 4719-4726, doi:10.1021/acsnano.8b01369 (2018).

159 Zhang, S. *et al.* Defect Structure of Localized Excitons in a WSe_{2} Monolayer. *Physical review letters* **119**, 046101, doi:10.1103/PhysRevLett.119.046101 (2017).

160 Wu, F., Lovorn, T. & MacDonald, A. H. Topological Exciton Bands in Moire Heterojunctions. *Physical review letters* **118**, 147401, doi:10.1103/PhysRevLett.118.147401 (2017).

161 Aivazian, G. *et al.* Many-body effects in nonlinear optical responses of 2D layered semiconductors. *2d Materials* **4**, 025024, doi:10.1088/2053-1583/Aa56f1 (2017).

162 Srivastava, A. *et al.* Valley Zeeman effect in elementary optical excitations of monolayer WSe2. *Nature Physics* **11**, 141-147, doi:10.1038/nphys3203 (2015).

163 MacNeill, D. *et al.* Breaking of valley degeneracy by magnetic field in monolayer MoSe2. *Physical review letters* **114**, 037401, doi:10.1103/PhysRevLett.114.037401 (2015).

164 Li, Y. *et al.* Valley splitting and polarization by the Zeeman effect in monolayer MoSe2. *Physical review letters* **113**, 266804, doi:10.1103/PhysRevLett.113.266804 (2014).

165 Aivazian, G. *et al.* Magnetic control of valley pseudospin in monolayer WSe 2. *Nature Physics* **11**, 148-152, doi:10.1038/nphys3201 (2015).

166 Schaibley, J. R. *et al.* Directional interlayer spin-valley transfer in two-dimensional heterostructures. *Nature communications* **7**, 13747, doi:10.1038/ncomms13747 (2016).

167 Li, Y. M. *et al.* Light-Induced Exciton Spin Hall Effect in van der Waals Heterostructures. *Physical review letters* **115**, 166804, doi:10.1103/PhysRevLett.115.166804 (2015).

168 High, A. A., Novitskaya, E. E., Butov, L. V., Hanson, M. & Gossard, A. C. Control of exciton fluxes in an excitonic integrated circuit. *Science* **321**, 229-231, doi:10.1126/science.1157845 (2008).

169 Wu, M., Qian, X. & Li, J. Tunable exciton funnel using Moire superlattice in twisted van der Waals bilayer. *Nano letters* **14**, 5350-5357, doi:10.1021/nl502414t (2014).

170 Seamons, J. A., Morath, C. P., Reno, J. L. & Lilly, M. P. Coulomb drag in the exciton regime in electron-hole bilayers. *Physical review letters* **102**, 026804, doi:10.1103/PhysRevLett.102.026804 (2009).

171 Lamas-Linares, A., Howell, J. C. & Bouwmeester, D. Stimulated emission of polarization-entangled photons. *Nature* **412**, 887-890, doi:10.1038/35091014 (2001).

172 Perczel, J. *et al.* Topological Quantum Optics in Two-Dimensional Atomic Arrays. *Physical review letters* **119**, 023603, doi:10.1103/PhysRevLett.119.023603 (2017).